Journal of the Electrochemical Society of India

Indian Institute of Science Campus,
Bengaluru - 560 012, India

Guest Editor

Dr. Rajalakshmi N

Dr. S.T. Aruna

Vol. No. 73 (5&6), July-Sept 2024

CODEN - JESIA 73 [5&6] 2024 ISSN:0013-466X

INSTRUCTIONS TO AUTHORS

GENERAL

Address all manuscripts to the Managing Editor, Electrochemical Society of India,(JECSI) Bengaluru-560012 and send it by email to arunaecsi@gmail.com / ecsiiisc@gmail.com. Submission of an article will be taken to imply that it has not been previously published and is not under consideration for publication elsewhere. And further that if accepted, it will not be published elsewhere. Submit an electronic version of the paper in WORD format along with a pdf version in order not to miss any portion due to transmission faults. Identify the address, affiliation, email address of the author (corresponding author in case of multiple authors). Also, identify the category in which the paper qualifies for publication.

Journal of the Electrochemical Society of India (JECSI) is a multidisciplinary journal in the general area of Electrochemical Science and Technology. Research and review papers of general significance that are written clearly and well organized will be given preference. All submitted papers will be reviewed by three experts to determine suitability. Paper found unsuitable in terms of the overall requirements of the Journal and those not accepted by the reviewers will be returned to the authors. Both solicited and unsolicited papers will be reviewed. Authors will be notified of acceptance, rejection or any need for revision before acceptance for publication. Any illustrations or other material reproduced from other publications must be properly credited. It is the author's responsibility to obtain the necessary permission in such cases.

CATEGORIES OF MANUSCRIPTS

GeneralArticles, not exceeding 5000 words in length, should discuss current trends in research in a field that will be of interest to readers outside the field; interdisciplinary topics; Science policy and administration; Impact of Science and Technology on Society, etc. The paper should include a summary not exceeding 200 words, introductory paragraph(s), brief subheads at appropriate places to point to what follows, Illustrations that will help a general reader and references.

Review Articles, not exceeding 5000 words, are expected to survey and discuss recent developments in a relevant field. They should be well focused and organized. General text book style is not acceptable. Research Articles should report and discuss results of work of a fairly major significance. They should include an Abstract, introductory paragraph(s) and brief subheads indicating materials and methods used, major results and discussion of results, relevant illustrations and references.

Research Communications, not exceeding 2000 words, should contain important findings that are novel and are of fairly broad interest. They should not be broken up under subheads. Correspondences include letters, not exceeding 500 words that are of general interest to Scientist, Engineers and Technologists. Only selected letters will be published. Scientific Correspondence contains technical comments, including those on articles or communications published in JECSI. Appropriate letters will be published.

Book Reviews are reviews of books published in the major areas of Electrochemical Science, Technology and Engineering. Unsolicited reviews will also be considered. Reviews that simply 'list' the contents will not be acceptable for publication. Reviews should have 'context' and convey information about the subject of the book. Historical Comments and Notes inform readers about interesting aspects of personalities or institutions of Science or about watershed events in the history/ development of science. Most are expected to relate to India. Illustrations are welcome with due credit if already published elsewhere.

MANUSCRIPT PREPARATION

The manuscript should be in double line spacing in an area corresponding to A-4 size paper with 25 mm margin all around. Page numbers, including that for the first page should be given at the bottom centre of the page. The title should be brief, specific and amenable to indexing. Give a maximum of 5 keywords which are carefully chosen and not phrases of several words. Summary and abstract should not have more than 200 words and should convey the main point of the paper, outline the results and conclusions and explain the significance of the work and results.

Text

Papers should begin with an introduction. The text should be intelligible to readers in different disciplines and technical terms should be defined. Tables and figures should be arranged in numerical order and referred to in that order. All symbols and abbreviations must be defined and used only when absolutely necessary. Superscripts and subscripts and ambiguous characters should be clearly indicated. Units of measure should be metric and preferably SI. Methods should, as far as possible, be described briefly in appropriate table and figure legends.

Figures are to be drawn in sizes that are clearly intelligible. Location and orientation of figures is the entire responsibility of the author(s). The actual location of figures and tables may be clearly indicated in the pdf format that accompanies the main word format submission. The same data should not be given in both tables and figures. Photomicrographs and other photographs that require a scale bar or a micron marker should be defined clearly in the caption. Magnifications are not acceptable in place of micron markers. Primary data should be submitted as far as possible as for example actual photograph of an electrophoretic gel rather than an idealized diagram.

References should be numbered in the order in which they appear first through the text and then through table and figure legends. Following examples indicate the different ways of writing the references:

Reference to a journal publication:

[1] J. Name, J.A.J. Name, R.A. Name, Title of article, J. Sci. Commun. Vol.no (year) page number xx–xy. https://doi.org/10.1016/ j.Sc.2010.00372.

Reference to a book:

[3] W. Name, E.B. Name, Title of the book, Edition, Publisher, Place name, year.

Reference to a chapter in an edited book:

[4] G.R. Name, L.B. Name, Chapter title, in: B.S. Name, R.Z. Name
(Eds.), Title of book, Publisher, Place name, Year, pp. xxx–yyy.

Acknowledgments should be brief and clear.

Funding: This work was supported by Granting Agency Name [grant numbers xxxx, yyyy];

Cover Photographs. Good photographs (colour or black and white) that pertain to a submitted paper will be considered for use on the cover of an issue.

Proofs and Publication: A final pdf version of the paper may be sent to the author before publication if there are any inaccuracies or doubts of any nature. Such a procedure is redundant in case no major editorial changes are made in the paper.

About Guest Editors

Dr.N.Rajalakshmi

Former Senior Scientist and Head,
Centre for Fuel Cell Technology, ARCI, HT Madras Research Park, Chennai 600 113

After obtaining Ph.D in Physics from IIT, Madras, she worked as post doctoral fellow in TH Darmstadt Germany and University of Geneva, Switzerland for about 8 years. She has worked on various aspects of Hydrogen economy like production, storage and utilization.

She has gained vast experience in Fuel cell technology both in Material aspects and Engineering challenges from SPIC Science foundation and Center for Fuel Cell Technology, ARCI for the past 20 years. She has received the Technology award from Spic Science Foundation, Bharat Vikas Award from Institute of Self-Reliance for clean energy generation, Nature publi shing award etc.

She has chaired many sessions and given invited talks in various International conferences on Fuel cell science, Engineering technology, Gordon Research Conference on Fuel cell s, Society of Automobile Engineers etc., in India and Abroad . She is a reviewer for many journals related to Hydrogen and Fuel cells.

She has about 200 publications in various International Journals, 10 book chapters and 25 patents to her credit.

She is a Top2% of the world Scientists from India by Stanford University ranking during 2020 & 2021.

She is a DST nominated representative in the Hydrogen energy projects at National and International level and also a member of National Hydrogen Mission, Professor of practice at IITDh, Advisor for Deakin University, Australia , CSTEP, Bangalore, a few startups in H_2 technology.

Dr. S.T. Aruna

Chief Scientist
CSIR-National Aerospace Laboratories
Bangalore-560017

Dr. S.T. Aruna is currently working as a Chief Scientist at Council of Scientific and Industrial Research - National Aerospace Laboratories (CSIR-NAL), Bangalore, India. She has a Master's Degree in Chemistry from Mysore University (1994) and she secured the first rank and won 4 gold medals. She obtained her Ph.D. from the Indian Institute of Science (IISc), Bangalore in the year 1998.

She worked as a postdoctoral fellow at Bar-Ilan University, Israel in the area of dye-sensitized solar cells from 1998-1999. She has authored ~ 140 research papers in international peer reviewed journals, 11 patents, co-authored a book and coedited a book, written 14 book chapters and 4 encyclopedia chapters. Her research papers have been well cited and her publications have an h-index of 45. Her name features in the list of top 2 per cent of the world scientists released by Stanford University. Her current research interests include development of tapecast ceramic substrates for electronics application, nanomaterials, plasma sprayed thermal and environmental barrier coatings, oxygen sensor and solid oxide fuel cells (SOFCs). She has guided 5 Ph.D students. One of her review papers has received the best cited paper award twice which was published in Current Opinion in Solid State and Materials science. She is on the editorial board of Surface Engineering Journal. She has won Sathish Dhawan Young Engineer Karnataka State Award-2021, Thermal spray excellence award-2025, Sasadhar Ray Memorial award-2023, MRSI Medal-2022, NM Sampat award -2016 and Pavan Nagpal Memorial award-2019.

Publication Ethics and Publication Malpractice Statement

The Journal of Electrochemical Society of India (JECSI) follows the Committee on Publication Ethics (COPE) *Code of Conduct and Best Practice Guidelines for Journal Editors* and the *Code of Conduct for Journal Publishers*. It is expected that authors, reviewers and editors follow the best-practice guidelines on ethical behaviour.

Responsibilities of Editorial Board

Editors evaluate submitted manuscripts only on the basis of their merit such as novelty, originality, importance, and its relevance to the journal's scope. The information or ideas imparted to the editors due to handling the manuscript will be kept confidential and will not be used for their own benefit. The editors will refrain from reviewing a manuscript in which they have conflict of interest and will be handled by other editorial board members. Editors and editorial staff will maintain confidentiality about the submitted manuscripts.

All the manuscripts submitted to the journal will undergo peer-review by at least two reviewers who are experts in that area. Based on the evaluation reports received from the reviewers, copyright permissions and plagiarism will be checked and then the Chief Editor decides on the publication of the manuscript.

The Chief Editor will take actions when ethical concerns are raised with regard to a submitted manuscript or published paper followed by a correction, retraction, expression of concern or relevant other notes will be published in JECSI.

Responsibilities of Authors

The Authors should present detailed and correct account of the work to enable others to reproduce the work. Fraudulent or inaccurate statements are not accepted. If required the authors will be asked to provide the raw data of their study if some suspicious figures are provided in the manuscript. Authors should check their manuscript for originality check using the standard software. Only manuscripts with similarity report <20% will be considered for peer review.

The authors should not simultaneously submit the same manuscript to multiple journals and is treated as unethical and such papers will be sent back to the authors and authors will be black listed.

Authors who have made significant contributions to the paper should only be included as authors in the manuscript and the role of each author has to be listed. The other peoples' name should be included in the acknowledgement section.

The authors should disclose the conflict of interest that would have influenced the results or their interpretation. Authors should also properly acknowledge the work of others and ensure proper citation of such works in the manuscript. The authors should clearly state in the manuscript if the work involved the use of hazardous chemicals, procedures or equipment. The authors should co- operate in submitting the revised manuscripts before the deadline and providing befitting replies to the reviewer comments.

The authors should inform the Chief Editor when they discover significant errors or inaccuracies in their own published work and publish a corrigendum or retract the paper.

Journal of The Electrochemical Society of India

CODEN JESIA 73 (5 & 6) July-Sept 2024. ISSN 0013-466X

Donor Members

M/s. Mascot Chemical Works, Bengaluru
M/s. Indian Telephone Industries Ltd., Bengaluru
M/s. Kangovi Electronics (P) Ltd., Bengaluru
M/s. Aquair Control Systems, Bengaluru
M/s. Stiver Equipment Pvt. Ltd., Bengaluru
M/s. Hindustan Aeronautics Ltd., Bengaluru
M/s. High Energy Batteries, Madurai
M/s. Electroplating Equipment Co., Bengaluru
M/s. Galvanosols Pvt. Ltd., Bengaluru
M/s. Pyro Technologies, Bengaluru
M/s. Shruthi Enterprises, Bengaluru
M/s. Grauer Weil (India) Ltd., Mumbai
M/s. Zaveri Brothers (P) Ltd., Mumbai
M/s. Standard Batteries, Mumbai
M/s. Geep Industries Syndicate Ltd.
M/s. Larsen and Toubro Ltd., Mysore
M/s. IR Technology Services Pvt. Ltd.
M/s. Brite Platers and Electrical Engineers,Bengaluru
M/s. Vijaya Metal Finishers, Bengaluru
M/s. Vinpla Plating Pvt. Ltd., Bengaluru
M/s. Surface Chem Finishers, Bengaluru

Permanent Sustaining Members

M/s. Tata Chemical
M/s Ashok Charitable Trust, Karaikudi
M/s. Mysore Paper Mills, Bhadravathi
M/s. Tata Iron and Steel Company Ltd., Jamshedpur
M/s. DCM Chemical Works
M/s. Indian Aluminum Company Ltd., Alwaye
M/s. Visveswaraya Iron and Steel Ltd., Bhadravathi

Journal of The Electrochemical Society of India

CODEN JESIA 73 (5 & 6) July-Sept 2024. ISSN 0013-466X

Email : ecsiiisc@gmail.com

Address all communications to :
THE ELECTROCHEMICAL SOCIETY OF INDIA
Indian Institute of Science Campus
Bengaluru - 560 012
Email : ecsiiise@gmail.com

Exploring Corrosion Resistance of Self-Assembled Monolayer Thin Films on Mild Steel Substrates

V.Sribharathy[1]*, S. John Mary.[2] Susai Rajendran[3]

[1.] *Department of chemistry, Anna Adarsh college for women,Chennai,-600040*

[2.] *Department of Chemistry, Loyola College, Chennai 600 034, India.*

[3.]*St Antony's College of Arts and Sciences for Women, Tha-maraipadi , Dindigul – 624 005, Tamilnadu, India*

**Corresponding author: bharathyvijayagopal1985@mail.com*

Abstract

Well-ordered Self Assembled Monolayers (SAMS) using adipic acid (AA) were formed on the oxide of iron carbon steel surface by immersion method. This leads to ordered, robust monolayer bound to the surface in a tetradentate manner. Monolayer formation takes place when carbon steel is immersed in an aqueous solution containing 60 ppm of Cl^- and 150 ppm of adipic acid for 5 minutes, and rinsing the physisorbed molecules in distilled water and heating in a hot air oven. The adipic acid monolayer on iron oxide steel carbon can withstand rinsing with water, concentrated acid and base exposure. Additionally, these monolayers are stable over the course of at least one week. The formations of monolayer were confirmed by AFM study and FTIR spectra. The SAMs were tested by polarization and EIS electrochemical analysis. The results of this study show that adipic acid monolayer adsorbed on metal surfaces can reduce electrochemical activity on the surface, often the first step in corrosion.

Keywords: *Self-assembled films; iron oxide surface; polarization study; electrochemical impedance spectroscopy; AFM; FTIR; corrosion.*

1. Introduction

Nanometer-sized particles are attracting considerable attention because of their unique properties,including optical, electrical, electrochemical, photo electrochemical and magnetic properties [1-3]. SAMs are ordered molecular assemblies formed by the adsorption of an active surfactant on a solid surface. The most elegant method for SAM formation consists of dissolving molecules in a solution and exposing an appropriate metal or substrate to this solution. Noble metals, such as gold and silver are hot spots of the research because they can be easily prepared and exist steadily.

Moreover, these nano-particles can be manipulated as desired. Much research efforts have been focused on transforming self-assembled (SA) nanoparticles into ordered structures [4]. Specific structures can provide controlled fabrication of nanometer-sized building blocks with distinctive and useful properties [5]. Polymer-stabilized nanoparticles are usually self-assembled into two-dimensional arrays on the substrate [6]. Yiwei Tan et al. [7] had reported the self-organization of wire-pattern arrays of Ag nanoparticles. Byeong-Hyeok Sohn et al. [5] had demonstrated a directed self-assembly of two different kinds of nanoparticles on a block copolymer micellar template using gold and iron oxide. The self-assembling process has been investigated to improve the corrosion inhibition of metals because self-assembled substances are able to react spontaneously on the metal surface and form compact and stable films [8]. These films can protect metal from corrosion successfully. Iron is a widely used metal with extensive industrial applications and the study of its corrosion inhibition has attracted much attention [9, 10]. The first work to use self-assembled films on iron for corrosion protection was self-assembled alkane thiols [11]. But the application of thiol-compounds is limited due to their toxicity. The SAMs are excellent systems for a more fundamental understanding of phenomena affected by competing intermolecular, molecular-substrates and molecule-solvent interactions like ordering and growth, wetting, adhesion, lubrication, and corrosion [12-31].

In the present work, SAMs of oxide / carbon steel surface using adipic acid (AA) were formed on carbon steel surface by immersion coating (immersing metal surface in an aqueous solution containing 60 ppm of Cl^-,

in the absence and presence of 150 ppm of adipic acid). The modified samples were characterized by Fourier Transorm Infrared (FTIR) spectroscopy and Atomic force Microscopy (AFM). The formation, uniformity, ordering and bonding of the monolayer accomplished by immersion method have been evaluated. Furthermore, the electrochemical properties of the unmodified and modified carbon steel surfaces were characterized by polarization study and electrochemical impedance spectroscopy (EIS) analysis to test the ability of the monolayer to reduce the corrosion of the surface.

2. Experimental Section

2.1. Development of Self Assembled Monolayer

Very pure adipic acid of analytical reagent grade was used in the present study. Carbon steel substrates (Composition : wt % : 0.026% S, 0.06% P, 0.4% Mn, 0.1% C and the rest Fe) of dimensions 1 x 1 x 0.2 cm^3 were polished to a mirror finish and degreased with trichloroethylene and stored in on oven at 100°C for more than 1 h.

The cleaned substrates were placed in the oven for 24 h. They were then immersed in an aqueous solution containing 60 ppm Cl^- in the absence and presence of 150 ppm of adipic acid for 5 min and placed in an oven at 100°C for at least 1 h.

2.2. Characterization of the Monolayer

The substrates were studied using a Perkin Elmer 1600 FTIR spectrophotometer. FTIR spectrophotometer was used to analyze the nature of interaction between the molecules of adipic acid (AA) and the substrate and the alkyl chain ordering the νCH_2 peaks as the reference. The film was removed carefully, mixed with KBr and made into pellets and FTIR spectra were recorded.

The carbon steel specimen immersed in blank and in the inhibitor solution for a period of 5 mins was removed, rinsed with double distilled water, dried and subjected to the surface examination. Atomic force microscopy (Veecoinnova model) was used to observe the samples' surface in tapping mode, using cantilever with linear tips. The scanning area in the images was 5 μm x 5 μm and the scan rate was 0.6 mm.

Polarization studies were carried out in a CH–Electrochemical workstation with impedance, model 660 A. It was provided with an IR compensation facility. A three electrode cell assembly was used. The working electrode used was carbon steel. A saturated calomel electrode (SCE) was used as the reference electrode and platinum was used as the counter electrode. From polarization study, corrosion parameters such as corrosion potential (E_{corr}), corrosion current (I_{corr}), Tafel slopes (b_c and b_a) and linear polarization resistance (LPR) were calculated. During the polarization study, the scan rate (v/s) was 0.01; hold time at E_f (s) was zero and quiet time (s) was 2.

The instrument used for polarization study was used to record electrochemical impedance spectra (EIS) also. The cell setup was also the same. The real part (Z') and imaginary part (Z") of the cell impedance were measured in ohms at various frequencies. Value of charge transfer resistance (Rt), double layer capacitance (Cdl) and impedance, log (Z/ohm) were derived from Nyquist and Bode plots. Electrochemical impedance spectra were recorded with initial E (v) = 0; High frequency (Hz = 1 x 105); Low frequency (Hz = 1); Amplitude (v) = 0.005 and Quiet Time (s) = 2.

3.Results

3.1. FTIR Spectra

A simple procedure of immersing mild steel into an aqueous solution containing 60 ppm of Cl^- and 100 ppm of adipic acid for 5 minutes led to spontaneous film formation on the iron oxide surface, produced by the interaction of chloride ion present in the medium with iron. There is also the possibility of formation of iron-adipic acid film, in the absence of iron oxide, if there is less corrosion or no corrosion of carbon steel. The samples were characterized by FTIR spectra to determine alkyl chain conformation and head group-substrate bonding. Position of the CH_2 stretching in the infrared spectrum can be used to determine the ordering of the alkyl chain within a film [32].

For disordered chains, the frequency of the CH_2 stretching is close to that of a liquid alkane (νCH_2asym ~ 2924 cm^{-1}) due to the presence of a gauche conformation in the alkyl chains [33]. For well-ordered alkyl chains, the frequency is shifted to lower wavenumbers and is close to that of a crystalline alkyl (νCH_2asym ~ 2914 – 2918 cm^{-1}) which is considered to have a high degree of order, with all-trans conformation throughout the alkyl chain. The FTIR spectrum of pure adipic acid (AA) is shown in Fig 1a. The peaks due to CH_2asym and CH_2sym appear at 2810 and 2724 cm^{-1}. The FTIR spectrum of iron oxide

film formed on a metal surface after immersion in 60 ppm Cl^- is shown in Fig 1c. The peaks due to iron oxide appear at γFeOOH = 1045, 1632 cm^{-1}; αFeOOH = 602 cm^{-1}. The peaks due to Fe_3O_4 are absent.

The position of the peaks corresponding to ν_{CH2}asym and ν_{CH2}sym after immersion in an aqueous solution containing 60 ppm of Cl^- and 150 ppm of adipic acid for 5 minutes and after rinsing in distilled water to remove any physisorbed material or multilayers were 2811cm^{-1} and 2808 cm^{-1}, respectively (Fig 1b). This indicates that the film is stable, well ordered and strongly bound to the surface. The IR spectra further indicate that the organic molecules are bound to the surface in a tetradentate manner as determined from the shifting of ν_C=O and νOH stretching of the two carboxyl groups of adipic acid specifically the ν C = O has shifted from 1725 to 1595 cm^{-1} and ν_{OH} has shifted from 3412 to 3423 cm^{-1}. Similar bidentate interaction has been reported for alkyl phosphonic acid on nickel oxide surface and other organic molecules on other oxides.

While FTIR spectroscopy can be used to characterize alkyl chain ordering and binding of the molecules to the surface, it cannot determine film thickness and integrity. Therefore, AFM imaging was used to examine the monolayer at nanometer resolution and to verify that the deposition method produces a uniform monolayer [33].

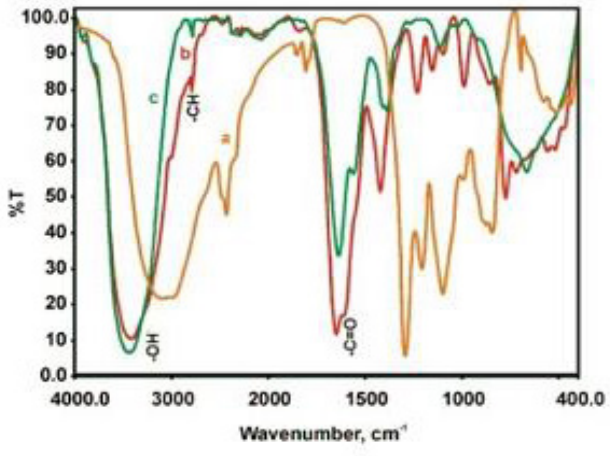

Fig. 1. FTIR spectra (KBr) of films formed on carbon steel surface after immersion in various test solutions (a) pure adipic acid (AA), (b) Adipic acid 150 ppm + Cl^- 60 ppm, (c) iron oxides formed on metal surface after immersion in solution containing 60 ppm of Cl^-.

3.2. AFM Imaging

The comparison of the root mean square (rms) roughness of the unmodified substrate to the modified samples is an indicator of the film uniformity. The rms roughness parameter is a measure of the deviations in the surface from the mean plane within the sampling area [34-36]. Modified surfaces with an rms roughness similar to the control surface are considered to be films of monolayer thickness that follow the contour of the surface, while modified surfaces that have much larger rms roughness than the control are multilayer or non-uniform films.

The iron oxide control samples had an average rms roughness of 12.06 nm (Fig 2a). The control sample of iron oxide is rough in comparison to model surfaces such as gold and silicon. Modified samples formed by the immersion method (immersed in 60 ppm of Cl had an rms roughness of 10.59 nm (Fig 2b).

The rms roughness of the substrate did not change very much after the adsorption of adipic acid molecules suggesting uniform deposition of the organic molecules on the surface without aggregate or micelle formation. Therefore, it is concluded that within the scope of the analysis, the film formed is a single layer of molecules that follows the contour of the underlying substrate. The rms roughness values of the films (SAMs) formed on iron oxide / metal surface after immersion in various test solutions are given in Table 1. The rms roughness 12.0558 nm is due to oxides of iron, confirmed by FTIR spectrum (Fig 1b) which are formed when carbon steel is immersed in 60 ppm Cl^- environment. When 100 ppm of adipic acid (AA) is added the rms value decreases to 10.5912 nm. This indicates that the protective film (SAMs) is formed on the metal surface itself, and not on the iron oxide surface. Had it formed on the iron oxide surface the rms value would have been greater than 12.0558 nm. So it is concluded that SAMs are formed not on the iron oxide surface but on the metal itself, even before the corrosion process starts, leading to the formation of iron oxide.

Table 1. The rms roughness values of the films (SAMs) formed on iron oxide / metal surface immersed in various test solutions.

Test solution	rms roughness of the films (SAMs), nm
Cl^- 60 ppm	12.0558
Cl^- 60 ppm + AA 150 ppm	10.5912

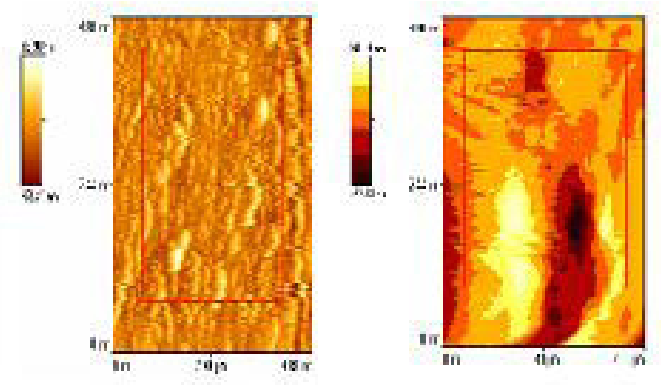

Fig. 2. AFM topography images of films formed on carbon steel surface after immerse on in various test solution (a) Cl^- 60 ppm (b): Cl^- 60 ppm + Adipic acid 150 ppm

3.3. Stability of Monolayer Films

The monolayers formed by the deposition method were analyzed for stability. After rinsing in water, the samples were left under atmospheric conditions for one day and analyzed. The monolayer remained ordered and bound to the surface as indicated by the unaltered FTIR spectra over one day. Stability to acid and base exposure was tested by rinsing modified substrates in 1 M HCl. IR spectra taken after these treatments remained unchanged.

Film stability and chain ordering can be dependent on alkyl chain length. In general, stability and order increase as the chain length increases. Therefore, a long chain length (> 11 carbons) is commonly used in the formation of SAMs. Substantial disorder is generally found in films formed by short chain molecules, although ordered monolayers of short chain phosphonic acids have been formed on nitinol, titanium and stainless steel oxide [37]. In the present study there are only 6 carbons in the chain. However, the monolayer is found to be stable. Since adipic acid is a dicarboxylic acid, tetradentate bonding is expected and this leads to the stability of the monolayer. It is obvious from the proposed structure of the monolayers, there is some strain in the CH_2 chain, as per Baeyer's strain theory. There are even numbers of (four) CH_2 groups in adipic acid. Therefore there is strain in the CH_2 chain. Interestingly, if the number of CH_2 groups is odd number (1, 3, 5) as in the case of malonic acid, glutaric acid and pimelic acid, more stability is expected, in the SAMs after coordination to the metal surface in a tetradentate fashion. Further, research in this line will confirm the proposed concepts [38]. This will also be reflected in the more corrosion resistance offered by these SAMs, during electrochemical studies such as polarization study and AC impedance spectra. These conclusions are confirmed by visual observations also. In the blank experiment (60 ppm Cl^-only) brown film was observed on the metal. In the presence of 150 ppm of AA brown film was absent and thin interference films (VIBGYOR color) were noticed.

3.4. Potentiodynamic Polarization Study

The potentiodynamic polarization curves of carbon steel immersed in an aqueous solution containing 60 ppm of Cl^- in the absence and presence of adipic acid (AA) are shown in Fig 3. The corrosion parameters such as corrosion potential (E_{corr}), Tafel slopes (b_c, b_a), linear polarization resistance (LPR) and corrosion current (I_{corr}) are given in Table 2.

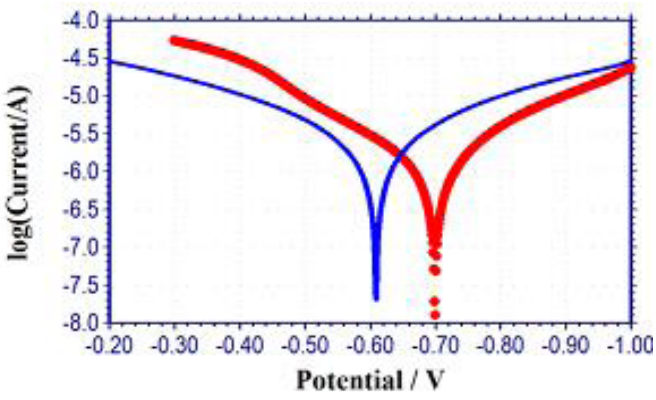

Fig. 3. Polarization curves of carbon steel immersed in various test solutions (a) Cl^- 60 ppm (b) Cl^-60 ppm + Adipic acid 150 ppm

Table 2. : Corrosion parameters of carbon steel immersed in aqueous solution containing 60 ppm of Cl^-

AA ppm	E_{corr} mV vs SCE	b_c mV/ decade	b_a mv/ decade	LPR ohm Cm^2	I_{corr} A / cm^2
0	-609	183	189	23319.1	1.7×10^{-6}
150	-700	163	186	30352	1.205×10^{-6}

Carbon steel electrodes were immersed in various test solutions for 5 minutes to attain the steady state potential. Then polarization curves were recorded. When carbon steel is immersed in an aqueous solution containing 60 ppm of Cl^-, oxides of iron are formed on the metal surface (FTIR spectra, Fig 1b). The corrosion potential is -609 mV vs SCE. The LPR is 23319.1 ohm cm^2 and the corrosion current is 1.735×10^{-6} A/cm^2 (Fig 3a). When 150 ppm of AA is added to the above environment, and allowed to stand for 5 minutes, self-assembled monolayers (SAMs) of AA are formed on the metal surface. Now the LPR value increases from 23319.1 ohm cm^2 to 30352 ohm cm^2 (Fig 3b). The corrosion current decreases from 1.735×10^{-6} A/cm^2 to 1.205×10^{-6}A/cm^2. This reveals that the SAMs formed on the metal surface have corrosion resistant property. The attack of Cl^- ions present in the bulk of the solution, on the metal surface, is prevented by the SAMs of adipic acid.

3.5. *Electrochemical Impedance Spectra*

The electrochemical impedance spectra of carbon steel immersed in various test solutions are shown in Fig 4. The impedance parameters such as charge transfer resistance (R_t), double layer capacitance (C_{dl}) and impedance value, long (Z/ohm), are given in Table 3.

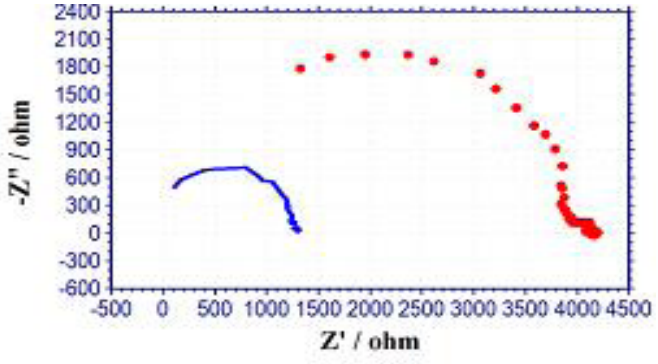

Fig. 4. Electrochemical impedance spectra of carbon steel immersed in various test solution (Nyquist Plots) (a) Cl^- 60 ppm (b) Cl^- 60 ppm + Adipic acid 150 ppm

(When carbon steel is immersed in an aqueous solution containing 60 ppm of Cl^-, and left for 5 minutes, oxides of iron are formed on the metal surface. The R_t value is 1225 ohm cm^2. The C_{dl} value is 4.3162×10^{-9} F /cm^2. The impedance, log (Z/ohm) is 3.60 (Fig 5).)

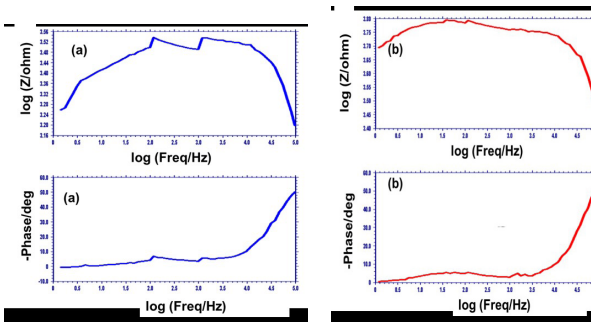

Fig. 5. AC impedance spectra (Bode Plots) of carbon steel immersed in solutions containing (a) Cl^- 60 ppm (b) Cl^- 60 ppm + Adipic acid 150 ppm

When carbon steel is immersed in an aqueous solution containing 60 ppm of Cl^- and 150 ppm of AA, the R_t value increases from 1225 ohm cm^2 to 2968 ohm cm^2; the C_{dl} value decreases from 4.3162×10^{-9} F/ cm^2 to 1.703×10^{-9} F/cm^2; the impedance value increases from 3.109 to 3.60 (Fig 4d). These results suggest that SAMs formed on the metal surface have corrosion resistanct properties. This results in an increase in R_t value and decrease in C_{dl} value.

Table 3. Impedance parameters of carbon steel immersed in an aqueous solution containing 60 ppm of Cl^-

AA ppm	R_t ohm cm^2	C_{dl} F/cm^2	Impedance log (Z/ohm)
0	1225	4.3161×10^{-9}	3.11
150	2968	1.703×10^{-9}	3.60

4. Discussion

Ordered, complete monolayers of adipic acid were formed on the iron oxide / iron surface. These monolayers were formed using an immersion deposition process. To accomplish monolayer by immersion, a counter action of 150 ppm of adipic acid, solution exposure time of 5 minutes and setting temperature of keeping the metal specimens in the oven at 100°C for 1 hr.

The process of monolayer formation using immersion coating has been described as a sequential process of nucleation, growth and coalescence of densely packed two-dimensional islands, finally covering the entire substrate surface or a large fraction of it [41-42]. The average surface coverage for adipic acid films on iron surface is found to increase monotonically with solution concentration, surface density of adipic acid molecules. It is proposed that the initial islands are nucleated through the adsorption of individual adipic acid mole from solution . Therefore a higher concentration of the monomer (150 ppm) in solution leads to more collisions between monomers and subsequent island nucleation becomes more probable leading to a large number of islands on the surface. For the immersed substrates, increasing the solution concentration leads to the formation of a complete monolayer. When the substrates were heated, the molecules become thermally mobile and therefore more available for nucleation and / or growth [41].

The molecules in the monolayers formed by immersion method were bound to the iron oxide / iron surface in a tetradentate manner. This bonding motif was persistent from deposition through solvent, acid and base rinsing and exposure to atmosphere for one day. A bidentate or monodentate bonding motif is seen between phosphonic acids and various metal oxides such as stainless steel 316L and Zirconium. In the present case, adipic acid is bonded to iron oxide/ iron surface in tetradentate manner, since adipic acid is a dicarboxylic acid and coordination can take place through oxygen atoms of carboxyl groups. The cause of the differences in bonding motifs has not been determined but it may be a function of several factors including oxygen-metal-oxygen distance on the surface, hydroxyl content of the native oxide surface and the coordination sites available on the adsorbate molecules.

5. Conclusions

Well-ordered SAMs using adipic acid were formed on the oxide of iron carbon steel surface by immersion method. This leads to ordered, robust monolayers bound to the surface in a tetra dentate manner. Monolayer formation takes place when carbon steel is immersed in an aqueous solution containing 60 ppm of Cl^- and 150 ppm of adipic acid for 5 minutes, and rinsing the physisorbed molecules in distilled water and heating in a hot air oven. The adipic acid monolayers on iron oxide steel carbon can withstand rinsing with water, concentrated acid and base exposure. Additionally, these monolayers are stable over the course of at least one week.

The formations of monolayers were confirmed by AFM study and FTIR spectra. The SAMs were tested by polarization and EIS electrochemical analysis. The results of this study show that adipic acid monolayer adsorbed on metal surfaces can reduce electrochemical activity on the surface, often the first step in corrosion. Monolayer formation on the iron oxide carbon steel surface is a significant advance in surface modification of iron oxide and can be used as a building block for future applications in corrosion barriers and electronics.

Acknowledgement

The authors are thankful to their management, St. Joseph's Educational and Research Trust, Dindigul and UGC, India for their help and encouragement.

References

[1] Liu, Z. Lin, W. Lin, K.S. Moon, C.P. Wong, Reversible superhydrophobic-superhydrophilic transition of ZnO nanorod/epoxy composite films. ACS Appl. Mater. Interfaces, 4(8) (2012) 3959-64. https://doi.org/10.1021/am300778d.

[2] L. Xiaoling, Z. Junhu, X. Weiqing, J. Huiying, W. Xu, Y. Bai, Z. Bing, L. Bofu, O. Yukihiro, Mercaptoacetic acid-capped silver nanoparticles colloid: formation, morphology, and SERS activity. Langmuir, 19(10) (2003) 4285–4290. https://doi.org/10.1021/la0341815.

[3] N. R. Jana, L. Gearheart, C.J. Murphy, Wet chemical synthesis of high aspect ratio cylindrical gold nanorods. J.Phys. Chem B, 105 (19) (2001) 4065-4067. https://doi.org/10.1021/jp0107964.

[4] H. Zeng, R. Skomski, L. Menon, Y. Liu, S. Bandyopadhyay, D. J. Sellmyer, Structure and magnetic properties of ferromagnetic nanowires in self-assembled arrays, Phys. Rev B, 65(13) (2002), 134426. https://doi.org/10.1103/PhysRevB.65.134426.

[5] B.H. Sohn, J.M. Choi, S.I. Yoo, S.H. Yun, W.C. Zin, J.C. Jung, T. Teranishi, Directed self-assembly of two kinds of nanoparticles utilizing monolayer films of diblock copolymer micelles, J. Am. Chem.Soc, 125(21) (2003)

6368–6369. https://doi.org/10.1021/ja035069w.

[6] T. Teranishi, M. Haga, Y. Shiozawa, M. Miyake, Self-Organization of Au Nanoparticles Protected by 2, 6-Bis (1 '-(8-thiooctyl) benzimidazol-2-yl) pyridine, J. Am. Chem. Soc, 122 (17) (2000) 4237-4238. https://doi.org/10.1021/ja000031u.

[7] L. Feng, S. Li, H. Li, J. Zhai, Y. Song, L. Jiang, D. Zhu, Super-hydrophobic surface of aligned polyacrylonitrile nanofibers, Angew. Chem. Int. Ed, 41(7) (2002) 1221-1223. https://doi org/10.1002/1521-3773(20020402)41:7<1221::AID-ANIE1221>3.0.CO;2-G.

[8] C.T. Wang, S.H. Chen, H.Y. Ma, C.S. Qi, Protection of copper corrosion by carbazole and N-vinylcarbazole self-assembled films in NaCl solution, J. Appl. Electrochem, 33 (2003) 179–186. https://doi.org/10.1023/A:1024097208128.

[9] G.L. Győrik, L. Mészáros, G. Mészáros, B. Lengyel, Some interesting peculiarities in the high frequency part of the impedance diagram obtained in the case of iron dissolution in dilute H_2SO_4 solution, Corros. Sci, 42 (2000) 79-90. https://doi.org/10.1016/S0010-938X(99)00042-6.

[10] K.F. Khaled, N. Hackerman, Investigation of the inhibitive effect of ortho-substituted anilines on corrosion of iron in 1 M HCl solutions, Electrochim. Acta 48 (19) (2003) 2715-2723. https://doi.org/10.1016/S0013-4686(03)00318-9.

[11] N. Katsuhisa , A. Kunitsugu, One- and two-dimensional polymer films ofmodified alkane thiol monolayers for preventing iron from corrosion, Corros. Sci, 41(1) (1999) 57-73. https://doi.org/10.1016/S0010-938X(98)00048-1.

[12] R. Lundy, P. Yadav, N. Prochukhan, E.C. Giraud, T.F. O'Mahony, A. Selkirk, E. Mullen, J. Conway, M. Turner, S. Daniels, P.G. Mani-González, Precise definition of a "monolayer point" in polymer brush films for fabricating highly coherent TiO_2 thin films by vapor-phase infiltration, Langmuir, 36 (41) (2020) 12394-12402. https://doi.org/10.1021/acs.langmuir.0c02512.

[13] D.P. Goronzy, J. Staněk, E. Avery, H. Guo, Z. Bastl, M. Dusek, N.M. Gallup, S. Gun, M. Kucerakova, B.J. Levandowski, J. Machacek, Influence of terminal carboxyl groups on the structure and reactivity of functionalized m-carboranethiolate self-assembled monolayers. Chem. Mater, 32(15) (2020) 6800-6809. https://doi.org/10.1021/acs.chemmater.0c02722.

[14] D.R. James, K.S. Melissa, J.E. Daniel, P. Jean, C.H. Luke, Expanding the scope of surface grafted polymers using electroinitiated polymerization. Langmuir, 36 (26) (2020) 7217-7226. https://doi.org/10.1021/acs langmuir.0c00444.

[15] L. Ross, Y. Pravind, S. Andrew, M. Eleanor, G. Tandra, C. Cian, A.M. Michael, Optimizing polymer brush coverage to develop highly coherent sub-5 nm oxide films by ion inclusion, Chem. Mater, 31(22) (2019), 9338-9345. https://doi.org/10.1021/acs.chemmater.9b02856.

[16]D.L.Elisa,P.Deborah,M.Mauro,P.Daniele,P.Andrea, F.R. Saverio, P.P. Pier, Multifunctional platinum@BSA–rapamycin nanocarriers for the combinatorial therapy of cerebral cavernous malformation, ACS Omega, 3 (11) (2018) 15389-15398. https://doi.org/10.1021/acsomega.8b01653.

[17] H. Yuanyuan, M. Jiani, H. Yu, J. Jing, J. Wei, Effect of end-grafted polymer conformation on protein resistance. Langmuir, 34 (5) (2018), 2073-2080. https://doi.org/10.1021/acs.langmuir.7b03930.

[18] A. Shaheen, J.M. Sturm, R. Ricciardi, J. Huskens, C.J. Lee, F. Bijkerk, Characterization of self-assembled monolayers on a ruthenium surface. Langmuir, 33 (25) (2017) 6419-6426. https://doi.org/10.1021/acs.langmuir.7b01068.

[19] L. Ross, B. Conor, B. Justin, N. Kevin, N.C. Maurice, D. Eric, E. Ryan, Exploring the role of adsorption and surface state on the hydrophobicity of rare earth oxides. ACS. Appl. Mater. Interf, 9 (15) (2017) 13751-13760. https://doi.org/10.1021/acsami.7b01515.

[20] S. Leila, E.F.Z. Victor, P.P. Samuel, J.T. Hastings, J.B. Brad, Relative Contribution of lateral packing density to albumin adsorption on monolayers. Langmuir 32 (32) (2016) 8034-8041. https://doi.org/10.1021/acs.langmuir.6b01885. https://doi.org/10.1021/acs.langmuir.6b01885

[21] A.P. Sergio, J.G. Anthony, L.S. O'Neil, B. Stephen, L. Hong, R.A. Neal, E.P. Jeanne, L.B.

Jean, G. David, R.M. Seth, Phosphonic acids for interfacial engineering of transparent conductive oxides, Chem. Rev, 116 (12) (2016) 7117-7158. https://doi.org/10.1021/acs.chemrev.6b00061.

[22] F. Abraham, E.F. William, S. Frank, N. Gabriele, S. Graham, V.W. Florian, Surface energy and work function control of alox/al surfaces by fluorinated benzylphosphonic acids, ACS Appl. Mater. Interf 8 (18) (2016) 11857-11867. https://doi.org/10.1021/acsami.6b02012.

[23] B. Asif, I. Danish, M.J. Sagar, B. Kathrin, A.H. Tarek, R. Michael, T. Andreas, Z. Michael, Promoting effect of protecting group on the structure and morphology of self-assembled monolayers: terphenylylethanethioactate on Au(111), J. Phys. Chem C, 119(45) (2015) 25352-25363. https://doi.org/10.1021/acs.jpcc.5b06813.

[24] S. Leila, J.B. Brad, Photopatterning of stable, low-density, self-assembled monolayers on gold, Langmuir, 31(9) (2015) 2689-2696. https://doi.org/10.1021/acs.langmuir.5b00001.

[25] K. Youngmin, L. Seungjae, L. Kyungjun, S. Sangdeok, Y.K. Jin, W.L. Hyung, C. Dukhyun, Self-assembled plasmonic nanoparticles on vertically aligned carbon nanotube electrodes via thermal evaporation, ACS. Appl. Mater. Interf, 6 (22) (2014) 20423-20429. https://doi.org/10.1021/am505999e.

[26] T. Melanie, V.N. Marco, K. Stefan, L. Giovanni, C. Christos, P. Luca, G. Angelo, F. Johannes, W. Berthold, M. Paolo, K. Norbert, Surface Modification of ZnO(0001)–Zn with phosphonate-based self-assembled monolayers: binding modes, orientation, and work function, Chem. Mater, 26 (17) (2014) 5042-5050. https://doi.org/10.1021/cm502171m.

[27] K. Volodymyr, P. Georg, Ion adsorption on modified electrodes as determined by direct force measurements under potentiostatic control, J. Phys. Chem C, 118(5) (2014) 2673-2685. https://doi.org/10.1021/jp500425g.

[28] K. M. Nuruzzaman, Z. Michael, Irradiation promoted exchange reaction with disulfide substituents. J. Phys. Chem C, 117 (28) (2013) 14534-14543. https://doi.org/10.1021/jp4006026.

[29] S.C. Alexander, L.F. Colin, D. Robert, M.D. Dorothy, Structure and orientation of MDBA self-assembled monolayers and their interaction with calcite: a molecular dynamics study, J. Phys. Chem C, 117 (14) (2013) 7148-7153. https://doi.org/10.1021/jp4006235.

[30] W. Hairong, S. Kai, K.G. Avijit, V. Julius, M.S. Peter, J.W.Z. Harold, Dynamics of decanethiol self-assembled monolayers on Au(111) studied by time-resolved scanning tunneling microscopy, Langmuir 29 (7) (2013) 2250-2257. https://doi.org/10.1021/la304902y.

[31] R. Bart, P.P. Sidharam, S. Luc, C.J.M. Van Rijn, J.E. Baio, T. Weidner, Z. Han, Hexadecadienyl monolayers on hydrogen-terminated Si(111): faster monolayer formation and improved surface coverage using the enyne moiety, Langmuir, 28 (16) (2012) 6577-6588. https://doi.org/10.1021/la204770r

[32] A. Raman, M. Dubey, I. Gouzman, E.S. Gawalt, Formation ES of self-assembled monolayers of alkylphosphonic acid on the native oxide surface of SS316L, Langmuir, 22(15) (2006) 6469-6472. https://doi.org/10.1021/la060636p.

[33] E.B. Troughton, C.D. Bain, G.M. Whitesides, R.G. Nuzzo, D.L. Allara, M.D. Porter, Monolayer films prepared by the spontaneous self-assembly of symmetrical and unsymmetrical dialkyl sulfides from solution onto gold substrates: Structure, Langmuir, 4 (1993) 365-385. https://doi.org/10.1021/la00080a021

[34] M.F. Panel, D. Landolt, The influence of gallic acid on the reduction of rust on painted steel surfaces, Corros. Sci, 34 (1993) 1481-1494. https://doi.org/10.1016/0010-938X(93)90243-A.

[35] A.J. Workman, The handbook of organic compounds, three-volume set: NIR, IR, R and uv-vis spectra featuring polymers and surfactants, Academic Press, Elsevier, 2000 34:1481- 1494. 2001.

[36] R. Quinones, E.S. Gawalt, Study of the formation of self-assembled monolayers on nitinol, Langmuir, 23(20) (2007) 10123-10130. https://doi.org/10.1021/la701110p.

[37] A. Faucheux, A.C. Gouget-Laemmel, C. Henry de Villeneuve, R. Boukherroub, F. Ozanam, P. Allongue, J.N. Chazalviel, Well-defined carboxyl-terminated alkyl monolayers grafted onto H− Si (111): packing density from a combined AFM and quantitative IR

study, Langmuir, 22 (2007)153-162. https://doi.org/10.1021/la052145v.

[38] I. Doudevski, W.A. Hayes, D.K. Schwartz, Submonolayer island nucleation and growth kinetics during self-assembled monolayer formation, Phys. Rev. Lett, 81 (1998) 4927. https://doi.org/10.1103/PhysRevLett.81.4927.

[39] D.K. Schwartz, Mechanisms and kinetics of self-assembled monolayer formation, Ann. Rev. Phys. Chem, 52 (1997) 107-137. https://doi.org/10.1146/annurev.physchem.52.1.107.

[40] J.T. Woodward, A. Ulman, D.K. Schwartz, Self-assembled monolayer growth of octadecylphosphonic acid on mica, Langmuir, 12(15) (1996) 3626-3629. https://doi.org/10.1021/la9510689.

[41] J.T. Woodward, I. Doudevski, H.D. Sikes, D.K. Schwartz, J. Phys. chem B, 101(38) (1997), 7535-7541. https://doi.org/10.1021/jp971338r.

Sulfur-Incorporated ZIF67 as Efficient and Chloride-Resistant Bifunctional Catalysts for Alkaline Seawater Splitting

Sana Fathima T. K.[a], Sundara Ramaprabhu[a],*

[a]*Alternative Energy and Nanotechnology Laboratory,*

Department of Physics, Indian Institute of Technology

Madras, Chennai-36, Tamil Nadu, India

**Corresponding author: ramp@iitm.ac.in*

Abstract

In this work, we report sulfur-incorporated cobalt-based zeolitic imidazolate framework (ZIF67) composites as highly selective, chloride-resistant, efficient, and durable bifunctional catalysts for splitting alkaline seawater. The sulfur-incorporation has been carried out using two simple and scalable techniques: (a) melt-diffusion (ZIF67-S) and (b) in-situ addition (S@ZIF67), for comparison. The OER and HER activities of these catalysts are meticulously studied in 1 M KOH, simulated and alkaline seawater. The ZIF67-S sample exhibits the lowest OER overpotential (360 mV vs RHE at 10 mA cm^{-2}), HER overpotential (282 mV vs RHE at 50 mA cm^{-2}) and overall splitting voltage (1.86 V at 20 mA cm^{-2}) in alkaline seawater, owing to the synergistic effects of the metal active sites and the sulfur content. Post-electrolysis study is also carried out to probe the underlying mechanism involved in the catalysis.

Keywords: *Catalyst; ZIF67; OER; Electrolysis*

1. Introduction

Water electrolysis has recently gained attention for its ability to generate hydrogen, the most desirable clean energy carrier, without emitting CO_2 [1]. However, its development is limited by its high energy and water requirement. Splitting of natural water sources, such as ground water, seawater etc. has been recently explored as sustainable alternatives to curb the consumption of freshwater. Such natural water electrolysis is highly challenging due to the presence of impurities, which may lead to competing reactions and reduced efficiencies [1–3]. Among these sources, seawater is the most desirable due to its abundancy, yet is the most difficult to split due to its peculiar composition. The ions in it, specifically chloride ions, lead to sluggish and competitive reactions, and pose a threat of corrosion to the catalysts and catalyst supports [4]. Recent studies have focused on rationally designing catalysts that can tackle these challenges.

Since the major complexities associated with seawater electrolysis arise at the anode side, where the chlorine evolution reaction (ClER) competes with the sluggish oxygen evolution reaction (OER) [2,5], most of the reports focus on developing OER-selective, chlorine-resistant OER catalysts [2,4,6,7]. This typically requires OER catalysts with an overpotential value below 490 mV and an alkaline electrolyte, so as to avoid the influence of the chloride ions [8]. This is evident from the Pourbaix diagram for simulated seawater model reported by Dionigi et al. [9], which indicates that OER is thermodynamically favored over ClER at pH>7.5. Hence, an alkaline pH is chosen in this work. We had previously reported a cobalt-based zeolitic-imidazolate framework (ZIF67) derived Co-CoO@C nanocomposite as an effective OER catalyst in alkaline seawater with an overpotential (OER) of 374 mV at 10 mA cm^{-2} [5]. Its superior OER activities (low overpotentials, excellent selectivity, high stability, etc.) were attributed to the inherent characteristics imparted by the ZIF (a class of metal-organic framework) such as hierarchical porosity, abundant surface active sites, etc. and its optimal composition. In particular, its chloride corrosion resistance was due to its unique morphology which comprised of a protective nitrogen-rich amorphous carbon layer surrounding the catalytic nanoparticles. Although effective, this catalyst did not exhibit any activity towards the hydrogen evolution reaction (HER). HER also suffers from sluggishness in seawater due to the adsorption of multiple ions on the cathode [10]. Hence, it is necessary to rationally design suitable OER and HER, preferably bifunctional, catalysts to realize practical seawater electrolysis. Several catalysts such as transition metal based oxides, hydroxides, sulfides, etc. have been widely reported for overall seawater splitting [2,10–12].

A notable strategy to boost the efficiency and prevent corrosion is the doping of sulfur or sulfidation of transition metal-based nanocatalysts, wherein the presence of the electronegative S atoms or negatively charged sulfide anions (S^{2-}) can effectively repel the chloride ions (Cl^-) in seawater [13–15]. Such heterocatalytic structures comprise of multiple phase interfaces which can act as active sites and promote the catalysis [16]. The charge rearrangement at these interfaces also renders the adsorption strengths of the reaction intermediates on the active sites more favorable. The performance of the catalyst would depend on the sulfur incorporation process and parameters used, as a uniform, atomistic distribution of sulfur atoms or sulfide ions are desired on the electrode. For instance, Haq et al. [13] developed S doped Cu_2O-CuO nanoneedles as corrosion-resistant and efficient OER catalysts for seawater splitting. They reported a low overpotential of 420 mV at 500 mA cm^{-2} and excellent stability (~100 h) in alkaline seawater. The remarkable performance was attributed to the presence of S which boosted the kinetics, corrosion-resistance, and turnover frequency (TOF). Zhang et al. [17] reported nickel coated Cu_2S nanoarrays (on copper foam) for highly efficient HER in alkaline simulated seawater, with an overpotential of 200 mV at 500 mA cm^{-2} and stability of ~150 h. Here, the adsorption of the H intermediates on Ni was boosted by the strong Ni-S interactions. In another work [16], N and S co-doped carbon-coated Ni_3S_2/MoO_2 nanowires supported on nickel foam were reported as bifunctional catalysts for alkaline seawater splitting. They observed low overpotentials for OER (191 mV at 10 mA cm^{-2}) and HER (52 mV at 10 mA cm^{-2}), and overall splitting voltage (1.71 V at 100 mA cm^{-2}) in alkaline seawater. They noted that the heteroatom doping significantly enhanced the conductivity of the catalyst.

In this work, we report the development of novel sulfur incorporated ZIF67 composites as efficient bifunctional catalysts for alkaline seawater splitting. The incorporation of sulfur is carried out by two simple and scalable methods: (a) melt-diffusion method, and (b) in-situ addition. These techniques are much simpler, cost-effective, and utilize lower temperatures compared to the reported multi-step sulfidation or sulfur-doping methods. To the best of our knowledge, such scalable bifunctional catalysts based on sulfur-incorporated ZIF67 have not been reported yet for water or seawater splitting. The catalysts have been coated on cost-effective graphite felt substrates instead of metallic foam to avoid corrosion. The developed catalysts exhibit remarkable resistance to hypochlorite formation, high OER selectivity, good HER activity, and excellent stability in alkaline seawater.

2. Materials and Methods

The materials used for the synthesis and electrochemical studies are given in the Supplementary section S1.1.

2.1. Preparation of ZIF67

ZIF67 was prepared as reported previously [5]. Briefly, an 80 mL solution of 2-methylimidazole (in methanol, 45 mmol) was added to an 80 mL solution of cobalt nitrate hexahydrate (in methanol, 5.74 mmol). The resultant solution was stirred continuously at room temperature for 12 h. It was then filtered, subjected to methanol-washed twice, and dried at 60 °C to obtain a violet powder, termedas ZIF67.

2.2. Preparation of ZIF67-S

The sulfur incorporated ZIF67 (ZIF67-S) was prepared by a previously reported melt-diffusion technique with slight modifications [18]. Initially, ZIF67 and sulfur were taken in the ratio 2:1 and ground well for 1 h using an agate mortar and pestle. Further, the mixture was transferred to a quartz ampule and sealed. This was then loaded in a horizontal tubular furnace and heated to 155 °C at a rate of 5 °C/min. The sample was maintained at that temperature for 15 h, followed by natural cooling. The entire process was carried out under argon atmosphere. The resultant sample was labelled as ZIF67-S.

2.3. Preparation of S@ZIF67

In order to validate the efficiency of the melt-diffusion technique, sulfur incorporation was also carried out using a simple, in-situ modification of the ZIF67 preparation procedure. Briefly, 300 mg of sulfur was dissolved in 20 mL methanol and stirred well. This mixture was added to the cobalt nitrate solution before the addition of 2-methylimidazole solution. The rest of the procedure is similar to that of ZIF67. The resultant powder was labelled as S@ZIF67.

3. Characterization

3.1. Physical Characterization

The X-Ray Diffraction (XRD) pattern (Figure 1) of ZIF67-S indicates that it crystallizes in the characteristic cubic structure of ZIF67 (CCDC: 1429244), without any

impurities or additional peaks. From literature, it can be seen that such similar XRD patterns after modifications confirm the successful incorporation of the targeted moiety (such as dye, nanoparticles etc.) in the parent ZIF structure (here, S in ZIF67) [19,20]. On the other hand, the XRD pattern of S@ZIF67 (Figure 1) exhibits peaks corresponding to sulfur (AMCSD: 0010058) in addition to that of the ZIF structure. This indicates that the solution mixing method may not have been effective in incorporating the sulfur within the structure, and led to the formation of a sulfur-ZIF67 composite, with the sulfur molecules loosely attached to the structure.

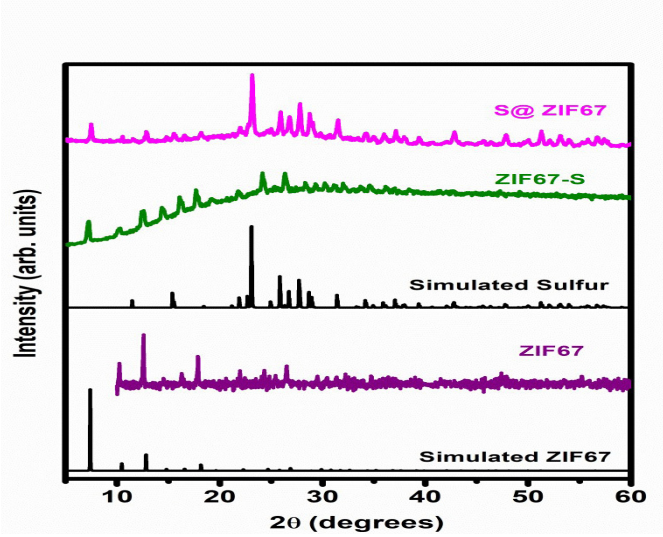

Fig. 1. XRD patterns of the synthesized catalysts

The sulfur incorporation was further validated from the thermogravimetric (TG) decomposition curves obtained in nitrogen atmosphere (Figure 2). The ZIF67 exhibits a two-step weight loss curve: first (~100 °C) corresponding to the loss of adsorbed moieties and a second (~450 °C) corresponding to the decomposition of the ligands in ZIF67 [5]. On the other hand, the ZIF67-S exhibits a weight loss region at ~155 °C corresponding to the sublimation of sulfur [18]. Based on this region, the sulfur loading content is estimated to be 40%. The S@ZIF67 exhibits additional weight loss regions, all of them corresponding to the loss of sulfur, but dependent on the strength of interaction between the sulfur and ZIF67.

The scanning electron microscopy (SEM) images of the samples are depicted in Figure 3. It can be observed that the ZIF67 exhibit micrometer-sized rhombic dodecahedrons, whereas the ZIF67-S has a heavily distorted yet smooth structure. The S@ZIF67 depicts structures similar to the parent ZIF67, with slight deformations and irregularities. The presence of sulfur in the prepared samples is also validated from their EDS spectra (Figure S1).

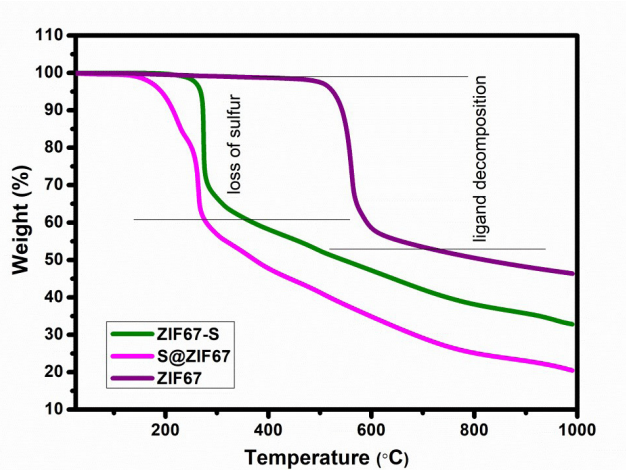

Fig. 2. TGA patterns of ZIF67, ZIF67-S, and S@ ZIF67

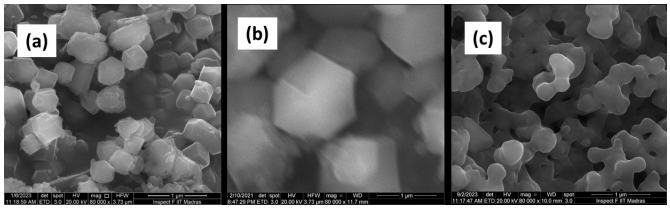

Fig. 3. SEM images of (a) ZIF67, (b) S@ZIF67, and (c) ZIF67-S

3.2. Electrochemical characterization

The OER activities of the prepared catalysts were initially assessed using the three-electrode mode. Before the measurement, the cyclic voltammograms (CV) of each catalyst/GF electrode was stabilized by running multiple cycles. The stabilized CV curves for ZIF67-S/GF are depicted in Figure S2a, and exhibit a pair of reversible redox peaks. This correspond to the M/M^{2+} and M^{2+}/M^{3+} redox couple, as discussed earlier [5]. This region is followed by a sharp increase in current density and simultaneous bubble formation, corresponding to oxygen evolution. Further, the iR-corrected linear sweep voltammograms (LSV) of all three catalyst/GFs obtained in 1 M KOH at a scan rate of 5 mV s^{-1} are depicted in Figure 4a. It is observed that the ZIF67-S/GF sample exhibited better OER activity compared to bare ZIF67 and S@ZIF67, with a remarkably low

overpotential (η) of 310 mV vs RHE at the benchmark current density of 10 mA cm^{-2}. This value is much lower than the cut-off of 490 mV to overcome the influence of chlorine in seawater, and hence is suitable for seawater electrolysis. Hence, the ZIF67-S/GF was further analyzed in simulated seawater (1 M KOH + 0.5 M NaCl) and alkaline seawater (seawater + 1 M KOH). The corresponding iR-corrected OER polarization curves are compared in Figure 4b. There is an obvious increase in the overpotential in seawater media (η_{10} = 360 mV vs RHE) due to the presence of multiple ionic moieties in it, specifically chloride ions. The η_{10} and η_{20} values in all three media are listed in Table 1.

Table 1: The OER η_{10} and η_{20} values of ZIF67-S/GF obtained in all three media

Catalyst/GF	η_{10} (mV vs RHE)	η_{20} (mV vs RHE)
1 M KOH	310	331
1 M KOH + 0.5 M NaCl	318	334
Seawater + 1 M KOH	360	386

To compare the kinetics of the catalyst/GFs, their Tafel slopes were calculated from the overpotential vs log j plots in 1 M KOH (Figure 4c). Both ZIF67/GF and S@ZIF67/GF exhibit a slope of ~89 mV dec^{-1}, indicating that the rate-determining step may be associated with the OH^- ion adsorption on the active sites. On the other hand, ZIF67-S/GF exhibits a lower slope of 51 mV dec^{-1}, indicating that the OH^- ion adsorption to M-O sites to form oxyhydroxide (M-OOH) may be the RDS in this case [21]. The lower Tafel slope of ZIF67-S/GF confirms its faster reaction kinetics compared to the other catalysts. In simulated and alkaline seawater (Figure 4d), ZIF67-S/GF exhibit Tafel slopes of 51.4 and 63.9 mV dec^{-1}, respectively. This may indicate a slightly slower kinetics in seawater medium, with the RDS being the adsorption of the OH^- ions to the M-OH sites [5].

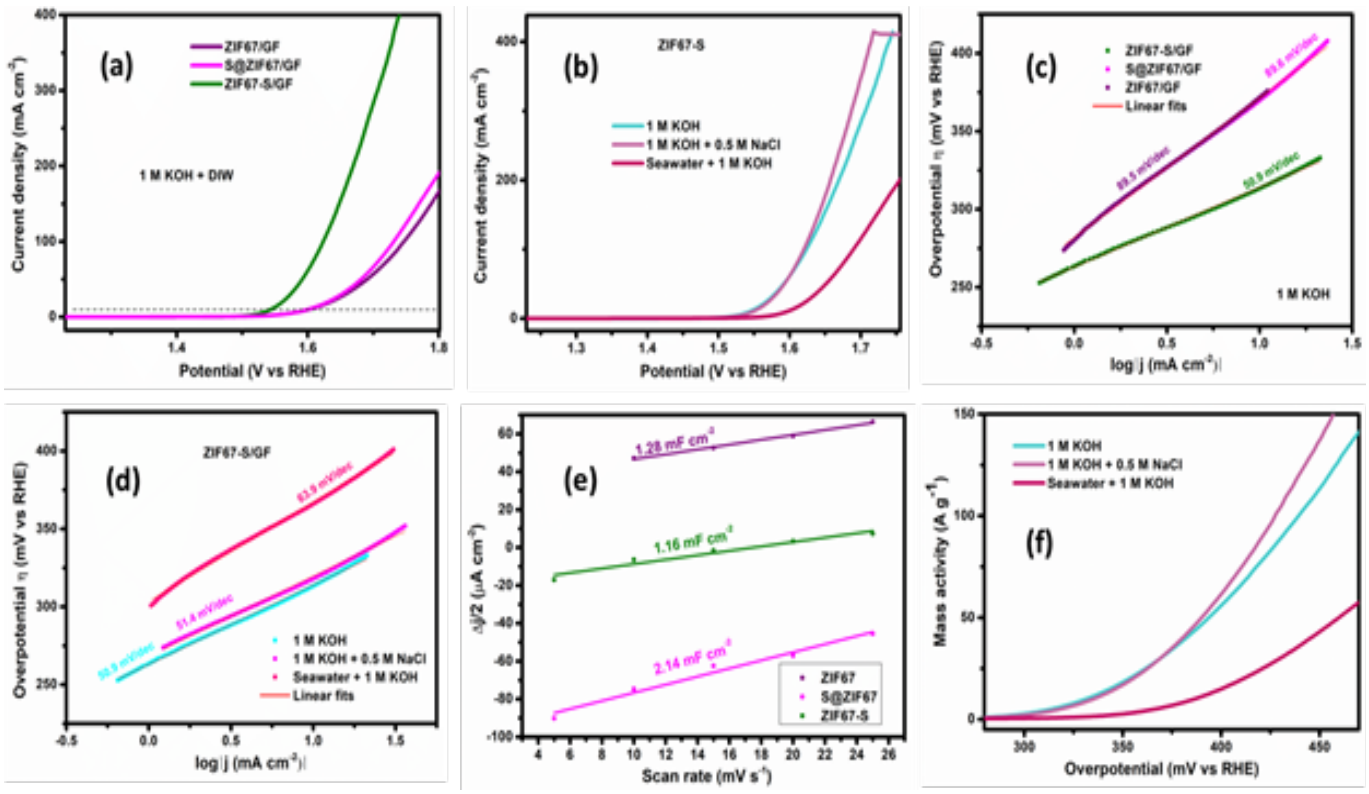

Fig. 4: (a) iR-corrected OER LSVs of the catalyst/GFs in 1 M KOH, (b) iR-corrected OER LSVs of ZIF67-S/GF in all three media, (c) Tafel slopes of the catalyst/GFs estimated in 1 M KOH, (d) Tafel slopes of ZIF67-S/GF in all three media, (e) C_{dl} values of the catalyst/GFs, and (f) mass activity of ZIF67-S/GF in all three media

Further, the electrochemical surface areas (ECSA) of the catalyst/GFs were estimated from the double layer capacitance values (C_{dl}) (Figures S3 and 4e) and are listed in Table 2. As reported earlier, the ECSA values do not seem to have an effect on the OER activity. The ZIF67-S/GF exhibits excellent mass activities (calculated as the current density divided by the catalyst loading (2 mg cm^{-2})) in all three media (Figure 4f).

To further correlate the performance of the catalyst/GFs, the concentration of the surface active sites was calculated (Supplementary section S1.4) from the area under the redox peaks observed in their CV in 1 M KOH (Figure S4) [5]. Higher surface active sites would imply more sites for the OER and HER reactions and faster kinetics. As seen in Table 2, the concentration varies as ZIF67-S/GF > S@ZIF67/GF > ZIF67/GF, validating the superiority of the melt-diffused ZIF67 sample (ZIF67-S).

Table 2: C_{dl}, ECSA, and surface concentration of active sites calculated for the catalyst/GFs

Catalyst/GF	C_{dl} (mF cm^{-2})	ECSA (cm^2)	Concentration of surface active sites (x 10^{16}) (cm^{-2})
ZIF67/GF	1.28	31.75	2.48
S@ZIF67/GF	2.14	52.92	4.39
ZIF67-S/GF	1.16	28.83	5.74

The activities of the catalyst/GFs towards HER were also measured in the three-electrode configuration. The stabilized CVs obtained prior to the polarization curves are shown in Figure S2b. In this case, the rapid increase in j along with bubble evolution corresponds to the hydrogen evolution at the electrode. The iR-corrected LSVs for HER of S@ZIF67/GF and ZIF67-S/GF in 1 M KOH (Figure 5a) depict a drastic improvement compared to ZIF67/GF. In our previous work [5], bare ZIF67/GF and ZIF67-derived materials did not show any activity towards HER. Interestingly, the incorporation of sulfur into the ZIF67 structure makes it active to HER, which may be attributed to the charge modulation occurring due to the strong interactions between the metal sites and sulfur [17]. The ZIF67-S/GF exhibits lower η_{50} value (321 mV vs RHE) compared to S@ZIF67 (402 mV vs RHE). The Tafel slope is also lower for ZIF67-S/GF (93 mV dec^{-1}) (Figure 5b). Hence, higher activity and faster kinetics for HER are observed for ZIF67-S/GF. The slopes obtained are in the range of 90 – 120 mV dec^{-1} which suggests that the RDS may be the Volmer step [10]. Further, the HER activities of the ZIF67-S/GF in simulated and alkaline seawater are shown in Figure 5c. The η_{50} and η_{100} values observed are listed in Table 3. It can be observed that the presence of ions boosts the HER activity, as it enhances the electrolyte conductivity. The Tafel slopes (Figure 5d) in this case also suggest that the Volmer step may be the RDS. The mass activities in all three media are expressed in Figure 5e.

Table 3: The HER η_{50} and η_{100} values of ZIF67-S/GF obtained in all three media

Catalyst/GF	η_{50} (mV vs RHE)	η_{100} (mV vs RHE)
1 M KOH	322	366
1 M KOH + 0.5 M NaCl	214	280
Seawater + 1 M KOH	282	350

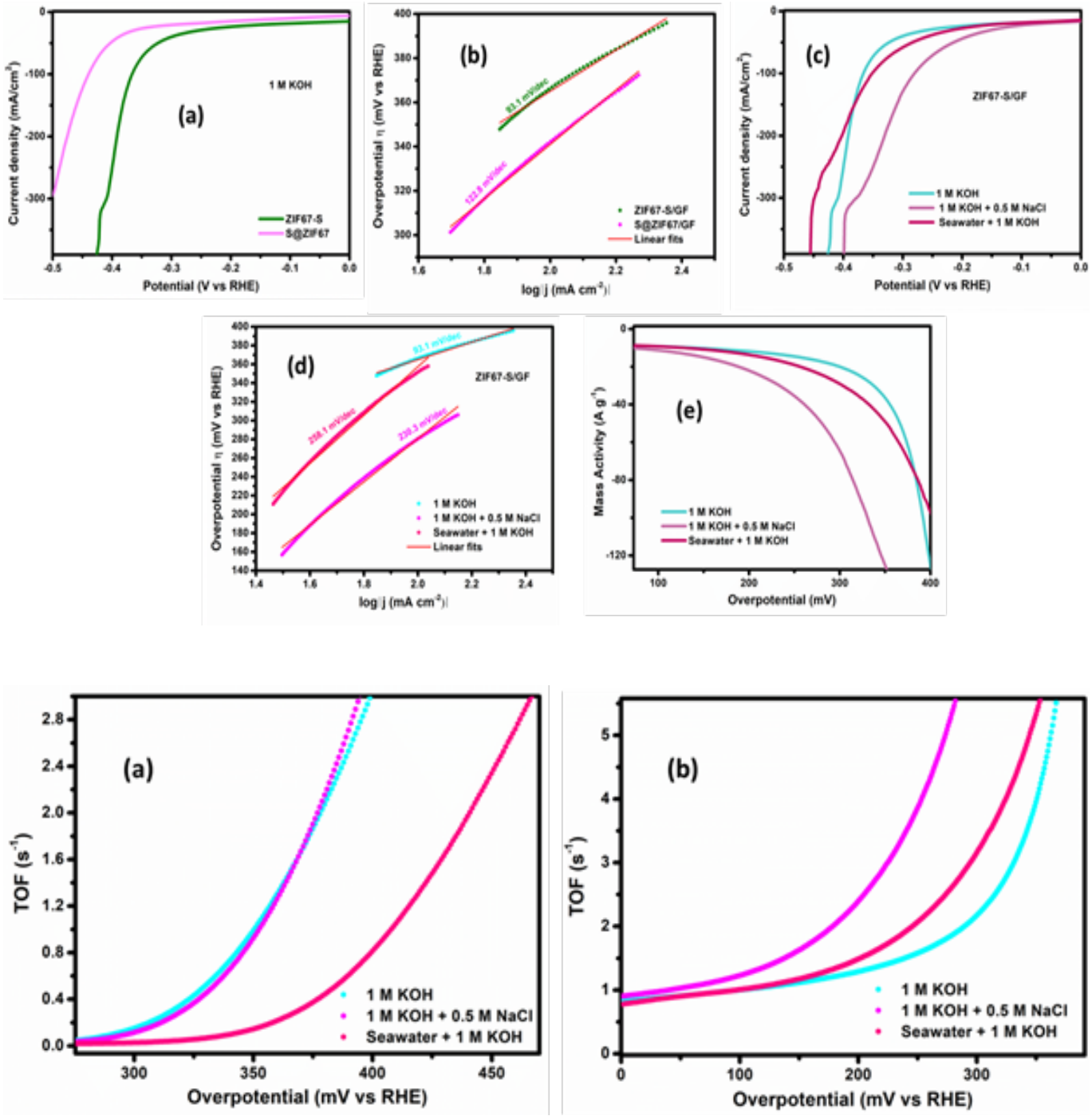

Fig. 5. (a) iR-corrected HER polarization curves and (b) Tafel plots of the catalyst/GFs in 1 M KOH, (c) iR-corrected HER polarization curves, (d) Tafel plots, and (e) mass activity of ZIF67-S/GF in all three media

The oxygen and hydrogen turnover frequencies (TOF) for ZIF67-S/GF calculated as described in Supplementary section S1.4 is depicted in Figure 6 (plotted versus overpotential). The TOFs obtained at specific overpotential values are listed in Table 4.

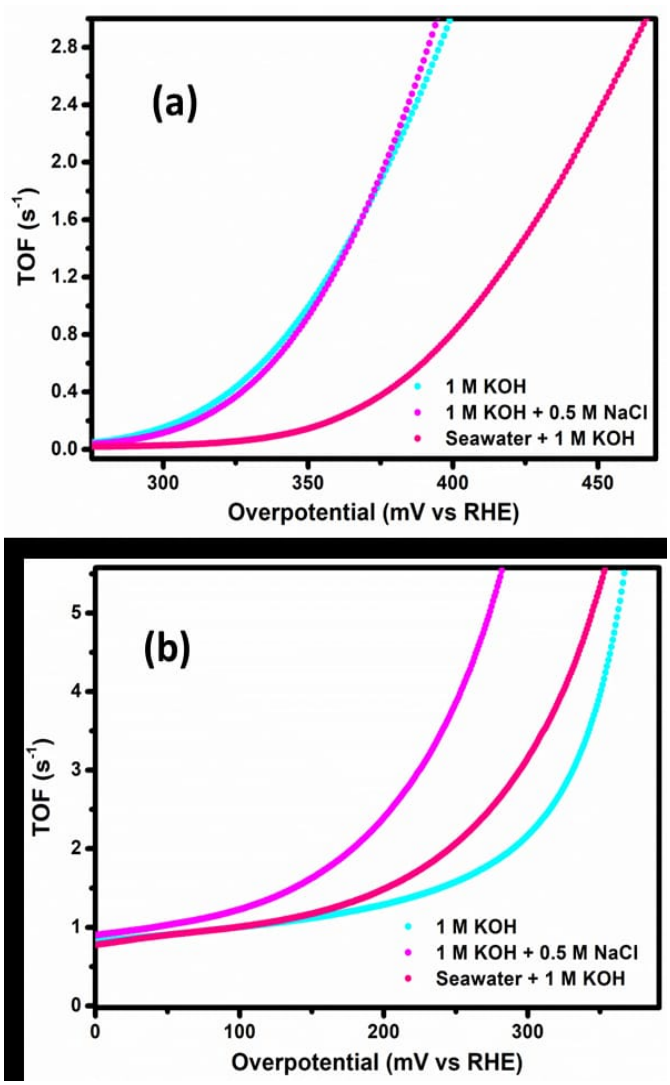

Fig. 6. (a) O_2 TOF and (b) H_2 TOF of ZIF67-S/GF in all three media

Table 4: The O_2 and H_2 TOF (s^{-1}) values of ZIF67-S/GF at specific overpotentials obtained in all three media

Catalyst/GF	O_2 TOF (s^{-1}) at η =		H_2 TOF (s^{-1}) at η=	
	310 mV	400 mV	200 mV	250 mV
1 M KOH	0.23	3.04	1.27	1.54
1 M KOH + 0.5 M NaCl	0.18	3.40	2.38	3.87
Seawater + 1 M KOH	0.03	0.82	1.46	2.10

3.3. Full-cell studies

Since the ZIF67-S catalyst exhibited superior performance for both OER and HER, it was considered further for the full-cell studies. The ZIF67-S/GF was taken as both anode and cathode, and the iR-corrected LSV was obtained in alkaline seawater (Figure 7a). A remarkably low overall splitting voltage of 1.86 V at 20 mA cm^{-2} (at room temperature) is observed for this ZIF67-S/GF||ZIF67-S/GF cell. For comparison, the iR-corrected LSV curve was also obtained in alkaline seawater using a standard combination of IrO_2/GF||Pt/C/GF (Figure S5). The overall splitting voltage obtained is 1.62 V at 20 mA cm^{-2}. This indicates that despite the absence of noble metals, the ZIF67-S catalyst can perform considerably well in alkaline seawater medium. The stability studies were also carried out in alkaline seawater at three different current densities (10, 15, and 20 mA cm^{-2}) for 15 h by the amperometric j-t technique. The ZIF67-S was coated on carbon paper (ZIF67-S/CP) for ease of post-electrolysis studies. Excellent stability is observed in all three cases (Figure 7b). To validate the efficacy of the catalyst for seawater electrolysis, the seawater after the stability study was subjected to a colorimetric hypochlorite detection test. As seen in Figure 7c, no colour change is observed after the addition of the reagent, which confirms the absence of hypochlorite.

3.4. Post-electrolysis studies

The ZIF67-S/CP after the stability study was subjected to post-electrolysis XRD to delve into the underlying origin of the splitting activity. As evident from Figure 7d, the original phase of the ZIF67-S is not observed in the patterns. The ZIF67 structure is known to immediately form a layer of cobalt oxide or oxyhydroxide on exposure to OH^- ions. Here, peaks corresponding to the fcc CoO structure (denoted by @) and Co_3O_4 (denoted by #) are observed, both before and after electrolysis [5]. This implies that a layer of CoO or Co_3O_4 may have formed during the coating process and further in-situ during the electrolysis. This in-situ formed layer further acts as the active layer for catalysis. The formation of this layer is also evident in the CV patterns of ZIF67-S/GF in all the media, i.e., the pair of redox peaks observed corresponds to the transformation of Co to CoO or Co_3O_4. Additionally, the pattern after HER comprises of a few unassigned peaks (denoted by *) which may be occurring due to the adsorption of several ions from the seawater [5].

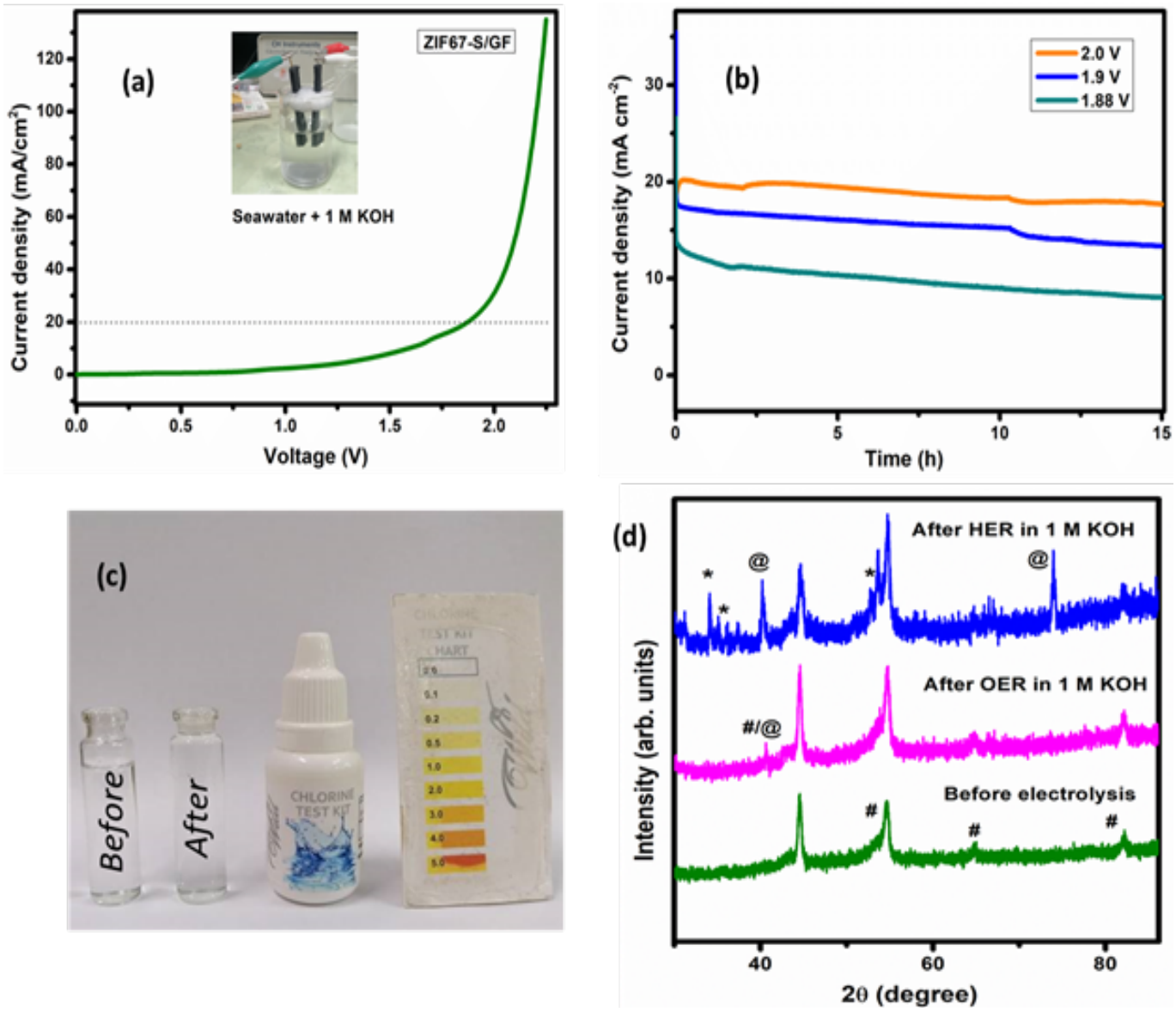

Comparison of η_{OER}, η_{HER}, and overall splitting voltages of similar reported catalysts

Fig. 7. (a) Full-cell polarization curve obtained for ZIF67-S/GF||ZIF67-S/GF in alkaline seawater, (b) stability study of ZIF67-S/CP||ZIF67-S/CP at different applied voltages in alkaline seawater, (c) hypochlorite test before and after the stability study, and (d) post-electrolysis XRD of the coated electrode

4. Conclusion

In this work, sulfur-incorporated ZIF67 nanocomposites are reported as highly efficient bifunctional catalysts for alkaline seawater electrolysis. The ZIF67 sample with melt-diffused sulfur sample (ZIF67-S) exhibited superior performance for both OER and HER. Apart from the synergistic catalytic activity of the abundant Co or Co oxide active sites, this may also be attributed to the uniform distribution of the sulfur in the ZIF67 structure enabled by the melt-diffusion technique. The presence of the electronegative sulfur effectively repelled the chloride ions and boosted the OER selectivity and efficiency. In addition, sulfur incorporation also made the ZIF67 active towards HER, which may be due to the charge modulation arising from strong Co-S interactions. The ZIF67-S catalyst demonstrated comparable OER, HER, and overall seawater splitting performance than similar reported catalysts (Table 5). The HER activity

can be further improved by the incorporation of Ni or Mo sites. Optimizing the sulfur content can also considerably improve the performance, as a balance needs to be struck between repelling the undesirable chloride ions versus the adsorption intermediates. The developed catalyst is a highly efficient and economical substitute for current water splitting catalysts owing to its easy synthesis (two-step method with mild heat treatment; no noble metals) and low-cost precursors. We believe that this work can pave the way for the development of chloride-resistant, efficient bifunctional catalysts for alkaline seawater electrolysis.

Table 5: Comparison of η_{OER}, η_{HER}, and overall splitting voltages of similar reported catalysts

Catalyst	**Medium**	**η_{OER} (mV vs RHE)@ Current density (mA cm^{-2})**	**η_{HER} (mV vs RHE)@ Current density (mA cm^{-2})**	**Overall splitting voltage (V) @ j (mA cm^{-2})**	**Ref. (Year)**
S-(Ni,Fe)OOH/ NF	Seawater + 1 M KOH	300@100	-	-	[22] (2020)
NiFe/NiS$_x$-Ni/ NF	Simulated seawater	300@400	370@500	2.1@400	[23] (2019)
NiCoS/NF	Seawater + 1 M KOH	280@10	-	-	[24] (2021)
Ni_3N/Ni_3S_2/NF	Seawater + 1 M KOH + buffer	404@100	197@100	1.8@48.3	[25] (2019)
S-$NiMoO_4$@Ni-Fe LDH/NF	1 M KOH + Seawater	315@100	220@100	1.73@100	[26] (2022)
Co-CoO@C/GF	1 M KOH + Seawater	374@10	-	-	[5]
ZIF67-S/GF	*1 M KOH + Seawater*	*360@10*	*284@50*	*1.86@20*	*This work*

Acknowledgements

The authors acknowledge the Indian Institute of Technology Madras (IITM), India for financial support.

Reference

[1] Jiang S, Suo H, Zhang T, Liao C, Wang Y, Zhao Q, et al. Recent Advances in Seawater Electrolysis. Catalysts 12(2022) https://doi.org/10.3390/catal12020123.

[2] Mohammed-Ibrahim J, Moussab H. Recent advances on hydrogen production through seawater electrolysis. Mater Sci Energy Technol 3(2020):780–807. https://doi.org/10.1016/j.mset.2020.09.005.

[3] Kumar SS, Himabindu V. Hydrogen Production by PEM Water Electrolysis – A Review. Mater Sci Energy Technol 2 (2019) :442–54. https://doi.org/10.1016/j.mset.2019.03.002.

[4] Zhang F, Yu L, Wu L, Luo D, Ren Z. Rational design of oxygen evolution reaction catalysts for seawater electrolysis. Trends Chem 3(2021):485–98. https://doi.org/10.1016/j.trechm.2021.03.003.

[5] Fathima TKS, Ghosh A, Ramaprabhu S. ZIF67-derived Co–CoO@C nanocomposites as highly efficient and selective oxygen evolution reaction

(OER) catalysts for seawater electrolysis. Int J Hydrogen Energy 49(2023):780–93. https://doi.org/10.1016/j.ijhydene.2023.09.122.

[6] Yang J, Wang Y, Yang J, Pang Y, Zhu X, Lu Y, et al. Quench-Induced Surface Engineering Boosts Alkaline Freshwater and Seawater Oxygen Evolution Reaction of Porous NiCo2O4 Nanowires. Small 18(2022):1–9. https://doi.org/10.1002/smll.202106187.

[7] You H, Wu D, Si D, Cao M, Sun F, Zhang H, et al. Monolayer NiIr-layered double hydroxide as a long-lived efficient oxygen evolution catalyst for seawater splitting. J Am Chem Soc 144(2022):9254–63. https://doi.org/10.1021/jacs.2c00242.

[8] Jadhav AR, Kumar A, Lee J, Yang T, Na S, Lee J, et al. Stable complete seawater electrolysis by using interfacial chloride ion blocking layer on catalyst surface. J Mater Chem A 8(2020):24501–14. https://doi.org/10.1039/d0ta08543j.

[9] Dionigi F, Reier T, Pawolek Z, Gliech M, Strasser P. Design Criteria, Operating Conditions, and Nickel-Iron Hydroxide Catalyst Materials for Selective Seawater Electrolysis. Chem Sus Chem 9(2016):962–72. https://doi.org/10.1002/cssc.201501581.

[10] Mahmood N, Yao Y, Zhang JW, Pan L, Zhang X, Zou JJ. Electrocatalysts for hydrogen evolution in alkaline electrolytes: Mechanisms, challenges, and prospective solutions. Adv Sci 5(2018). https://doi.org/10.1002/advs.201700464.

[11] Ďurovič M, Hnát J, Bouzek K. Electrocatalysts for the hydrogen evolution reaction in alkaline and neutral media. A comparative review. J Power Sources 493(2021)4229708. https://doi.org/10.1016/j.jpowsour.2021.229708.

[12] Xie X, Du L, Yan L, Park S, Qiu Y, Sokolowski J, et al. Oxygen evolution reaction in alkaline environment: material challenges and solutions. Adv Funct Mater 32(2022)3. https://doi.org/10.1002/adfm.202110036.

[13] Haq T ul, Haik Y. S doped Cu2O-CuO nanoneedles array: Free standing oxygen evolution electrode with high efficiency and corrosion resistance for seawater splitting. Catal Today 400–401:(2022)14–25. https://doi.org/10.1016/j.cattod.2021.09.015.

[14] Haq T ul, Haik Y. Strategies of anode design for seawater electrolysis: Recent development and future perspective. Small Sci 2(2022); https://doi.org/10.1002/smsc.202200030.

[15] Jung SY, Kang S, Kim KM, Mhin S, Kim JC, Kim SJ, et al. Sulfur-incorporated nickel-iron layered double hydroxides for effective oxygen evolution reaction in seawater. Appl Surf Sci 568(2021)150965. https://doi.org/10.1016/j.apsusc.2021.150965.

[16] Fan X, Li B, Zhu C, Yan F, Zhang X, Chen Y. Nitrogen and sulfur co-doped carbon-coated Ni_3S_2/MoO_2 nanowires as bifunctional catalysts for alkaline seawater electrolysis. Small (2024)2309655:1–11. https://doi.org/10.1002/smll.202309655.

[17] Zhang B, Xu W, Liu S, Chen X, Ma T, Wang G, et al. Enhanced interface interaction in Cu_2S@Ni core-shell nanorod arrays as hydrogen evolution reaction electrode for alkaline seawater electrolysis. J Power Sources 506(2021)230235. https://doi.org/10.1016/j.jpowsour.2021.230235.

[18] Garapati MS, Ajay AP, Sundara R. Synergy between partially exfoliated carbon nanotubes-sulfur cathode and nitrogen rich dual function interlayer for high performance lithium sulfur battery. Carbon 147(2019)364–376. https://doi.org/10.1016/j.carbon.2019.03.007.

[19] Abdelhamid HN. Dye encapsulated hierarchical porous zeolitic imidazolate frameworks for carbon dioxide adsorption. J Environ Chem Eng 8(2020)104008. https://doi.org/10.1016/j.jece.2020.104008.

[20] Wang Z, Dou Z, Cui Y, Yang Y, Wang Z, Qian G. Sulfur encapsulated ZIF-8 as cathode material for lithium-sulfur battery with improved cyclability. Microporous Mesoporous Mater 185(2014)929–6. https://doi.org/10.1016/j.micromeso.2013.11.011.

[21] Anantharaj S, Ede SR, Karthick K, Sam Sankar S, Sangeetha K, Karthik PE, et al. Precision and correctness in the evaluation of electrocatalytic

water splitting: Revisiting activity parameters with a critical assessment. Energy Environ Sci 11(2018)1744–71. https://doi.org/10.1039/c7ee03457a.

[22] Yu L, Wu L, McElhenny B, Song S, Luo D, Zhang F, et al. Ultrafast room-temperature synthesis of porous S-doped Ni/Fe (oxy)hydroxide electrodes for oxygen evolution catalysis in seawater splitting. Energy Environ Sci13(2020)13439–45. https://doi.org/10.1039/d0ee00921k.

[23] Kuang Y, Kenney MJ, Meng Y, Hung WH, Liu Y, Huang JE, et al. Solar-driven, highly sustained splitting of seawater into hydrogen and oxygen fuels. Proc Natl Acad Sci U S A 116(2019)1624–1629. https://doi.org/10.1073/pnas.1900556116.

[24] Wang C, Zhu M, Cao Z, Zhu P, Cao Y, Xu X, et al. Heterogeneous bimetallic sulfides based seawater electrolysis towards stable industrial-level large current density. Appl Catal B Environ 291(2021)120071. https://doi.org/10.1016/j.apcatb.2021.120071.

[25] Zhao Y, Jin B, Vasileff A, Jiao Y, Qiao SZ. Interfacial nickel nitride/sulfide as a bifunctional electrode for highly efficient overall water/seawater electrolysis. J Mater Chem A 7(2019)8117–21. https://doi.org/10.1039/9ta01903k.

[26] Wang H, Chen L, Tan L, Liu X, Wen Y, Hou W, et al. Electrodeposition of NiFe-layered double hydroxide layer on sulfur-modified nickel molybdate nanorods for highly efficient seawater splitting. J Colloid Interface Sci 613(2022)349–58. https://doi.org/10.1016/j.jcis.2022.01.044.

Supplementary information
Sulfur-Incorporated ZIF67 as Efficient and Chloride-Resistant Bifunctional Catalysts for Alkaline Seawater Splitting

Sana Fathima T. K.[a], *Sundara Ramaprabhu*[a],*

[a]*Alternative Energy and Nanotechnology Laboratory, Department of Physics, Indian Institute of Technology Madras, Chennai-36, Tamil Nadu, India*

**Corresponding author: ramp@iitm.ac.in*

S1. Materials and methods

S1.1. Materials

Cobalt nitrate hexahydrate ($Co(NO_3)_2.6H_2O$, Merck), 2-methylimidazole ($C_4H_6N_2$, TCI), methanol (CH_3OH, CDH Fine Chemicals), Sulfur (Sigma-Aldrich), potassium hydroxide (KOH, Sigma-Aldrich), sodium chloride (NaCl, SRL Chem), ethanol (C_2H_5OH, Changshu Hongsheng Fine Chemicals), Nafion® (Sigma-Aldrich), graphite felt (Nickunj), iridium oxide (Sigma Aldrich), Pt/C (46%, Tanaka), and Toray carbon paper (Nickunj) were used as received. Millipore deionized water (DIW, 18 MΩ) was used for all the electrochemical characterizations. Seawater was collected from Tiruvanmiyur Beach, Chennai, India, and treated with 1 M KOH. The supernatant after the KOH treatment was used for all the measurements and is termed alkaline seawater.

S1.2. Physical characterization

The phases in the synthesized composites were identified by X-Ray Diffraction [Aeris Benchtop XRD, nickel-filtered Cu K_α radiation, $2\theta = 5°$ to 60°]. The pre- and post-electrolysis studies of the coated electrodes were carried out by Rigaku XRD (nickel-filtered Cu K_α radiation, $2\theta =$ 30° to 80°). The presence of sulfur in the nanocomposite was confirmed by a Simultaneous Differential Scanning Calorimetry-Thermogravimetric Analyzer [SDT Q600, nitrogen atmosphere, RT-1000 °C, 20 °C/min]. The morphology and elemental composition of the samples were analyzed by Field Emission Scanning Electron Microscope [INSPECT F FESEM, 20 kV] equipped with Energy Dispersive X-Ray Spectroscopy (EDS).

S1.3. Preparation of electrodes

For all the electrochemical measurements, graphite felt electrodes coated with the synthesized catalysts were used. The catalyst slurry was first prepared by grinding 5 mg of the catalyst + 10 µL of Nafion (5 wt% in isopropyl alcohol) + adequate amount of ethanol in a mortar and pestle. The slurry was then coated on one side (1x1 cm^2 area) of a graphite felt (GF) cut into strips (dimensions: 7x1x0.4 cm^3) using a paint brush, and dried at 60 °C. The catalyst loading was estimated by weighing the graphite felt before and after coating. A loading of ~2 mg/cm^2 was maintained for all the samples.

S1.4. Electrochemical characterizations

The electrochemical studies were carried out using CHI6083C Electrochemical Workstation. To assess the OER and HER activities, half-cell measurements were done in the three-electrode setup. The catalyst-coated graphite felt (catalyst/GF) was taken as the working electrode, platinum wire was taken as the counter, and Ag/AgCl (3 M KCl) was taken as the reference electrode. Before each measurement, the Ag/AgCl reference electrode was calibrated with respect to reversible hydrogen electrode (RHE). The calibration was carried out by performing HER in a H_2-bubbled 1 M KOH solution using Pt wire as both anode and cathode, and Ag/AgCl (3 M KCl) as reference electrode. The calibration potential was estimated as the onset potential of HER. The potential values vs RHE were calculated as

E(RHE) = E(Ag/AgCl) - E0(Ag/AgCl) Where E(Ag/AgCl) is the potential observed during the experiments, and E0(Ag/AgCl) is the calibration potential obtained vs RHE in alkaline medium.

For each catalyst, cyclic voltammetry (CV) was performed at a scan rate of 50 mVs^{-1} until a stable voltammogram was achieved (~10 cycles) (Range: -0.1 to 1.2 V vs Ag/AgCl for OER and -0.2 to -1.8 V vs Ag/AgCl for HER). Further, the OER/HER polarization curves were obtained by recording linear sweep voltammograms (LSV) in the corresponding ranges at 5 mV s^{-1}. The iR-compensation (100%) was done by the workstation to account for the iR drop due to solution resistance. All the measurements were done in 1 M KOH, simulated seawater (1 M KOH

+ 0.5 M NaCl), and alkaline seawater (seawater + 1 M KOH) media. The OER overpotentials were calculated as η = E (vs RHE) – 1.23 V. The HER overpotentials were calculated as η = 0 - E (vs RHE) V. All measurements were done at room temperature (26 °C)

Further, the performance of the bifunctional catalysts was analyzed by two-electrode full cell measurements. The catalyst/GF was used as both the working electrode (anode) and counter cum reference electrode (cathode). First CV was run (-0.1 to 2.1 V; 50 mV s^{-1}) to stabilize the response followed by LSV (-0.1 to 2.1 V; 5 mV s^{-1}). The polarization curves were obtained in alkaline seawater (seawater + 1 M KOH). All experiments were repeated atleast twice. The cell was also subjected to stability study in full-cell mode. For ease of post-stability analysis, catalyst coated on carbon paper (1x1 cm^2) was used. To analyze the stability, the assembled cell was subjected to amperometric current density vs time (j-t) study at constant current densities of 20, 15, and 10 mA cm^{-2} for ~15 h each in alkaline seawater.

The surface concentration of active sites were determined by a method proposed by Anantharaj et al.[1]. For the calculation, the area of the reduction peak in the CV curves of the catalyst/GF in 1 M KOH recorded at 50 mV s^{-1} was used. The calculation is detailed elsewhere.[2]

The H_2 and O_2 turnover frequencies were calculated as follows:[2]

$$TOF = \frac{j * N_A}{n * F * \Gamma}$$

Where j - current density (A cm^{-2})

N_A - Avogadro no.

n - Number of electrons involved (4 for OER, 2 for HER)

F – Faraday constant (96485 C)

Γ – Surface concentration of active sites or number of participating atoms in catalyst material

S1.5. Hypochlorite detection test

The absence of hypochlorite in the seawater after electrolysis was ensured by a colorimetric chlorine test kit (Wild). In the presence of any chlorine-containing solution, a colour change is observed (yellow) when the reagent is added. To confirm hypochlorite-free electrolysis, 5 drops of the reagent were added to 5 ml of the seawater + 1 M KOH solution after the stability study, and colour change was monitored.

S2. Results

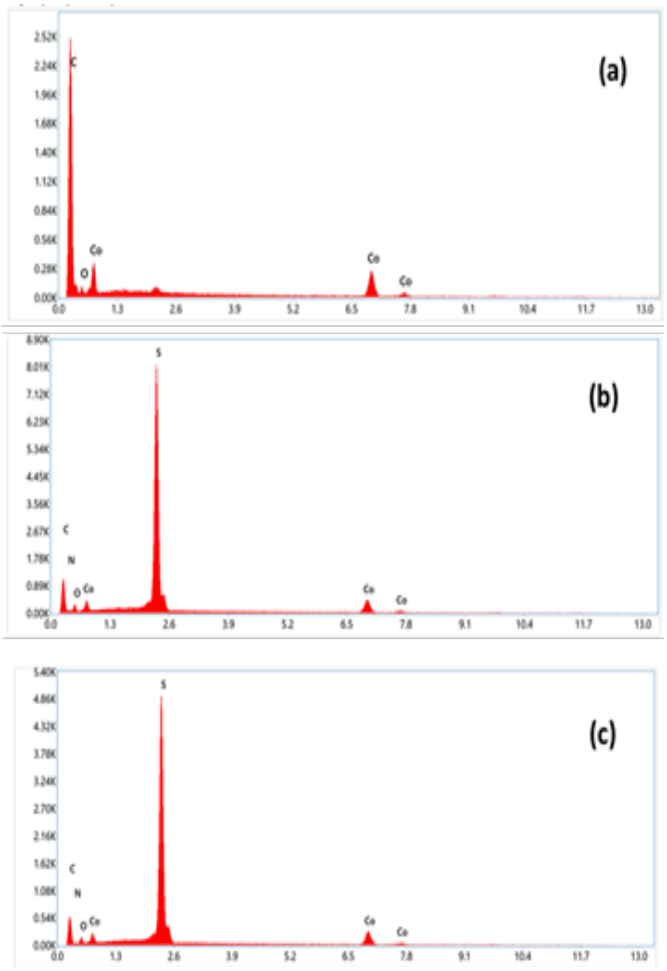

Figure S1: EDS spectra of (a) ZIF67, (b) ZIF67-S, and S@ZIF67

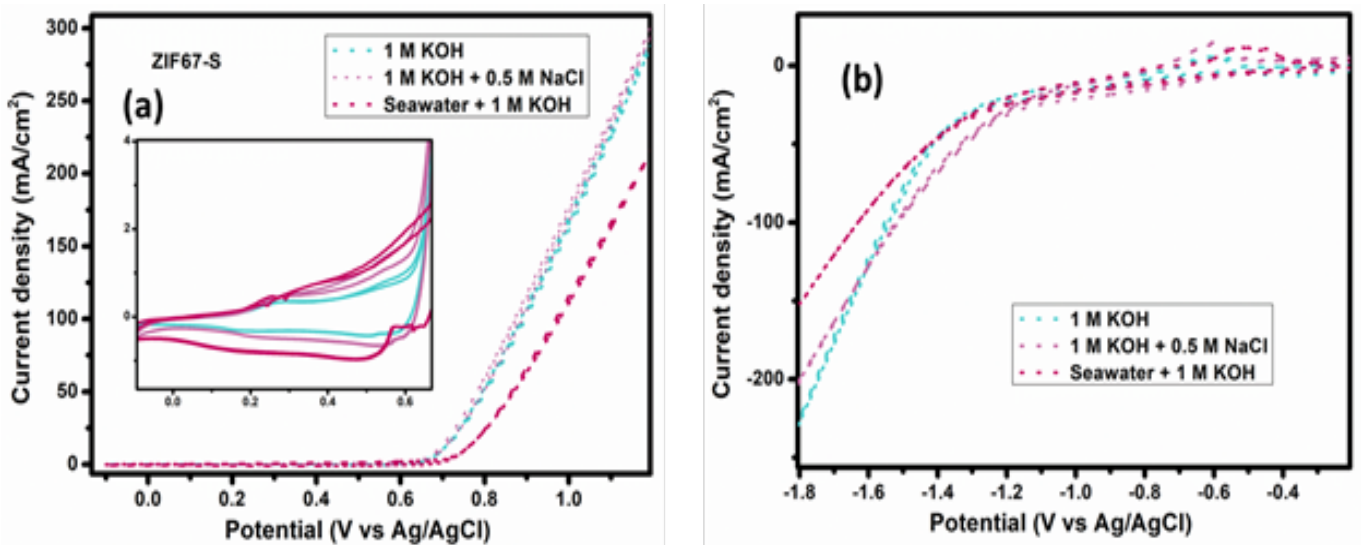

Figure S2: Stabilized (a) OER and (b) HER CV curves of ZIF67-S/GF obtained in 1 M KOH, simulated seawater, and alkaline seawater.

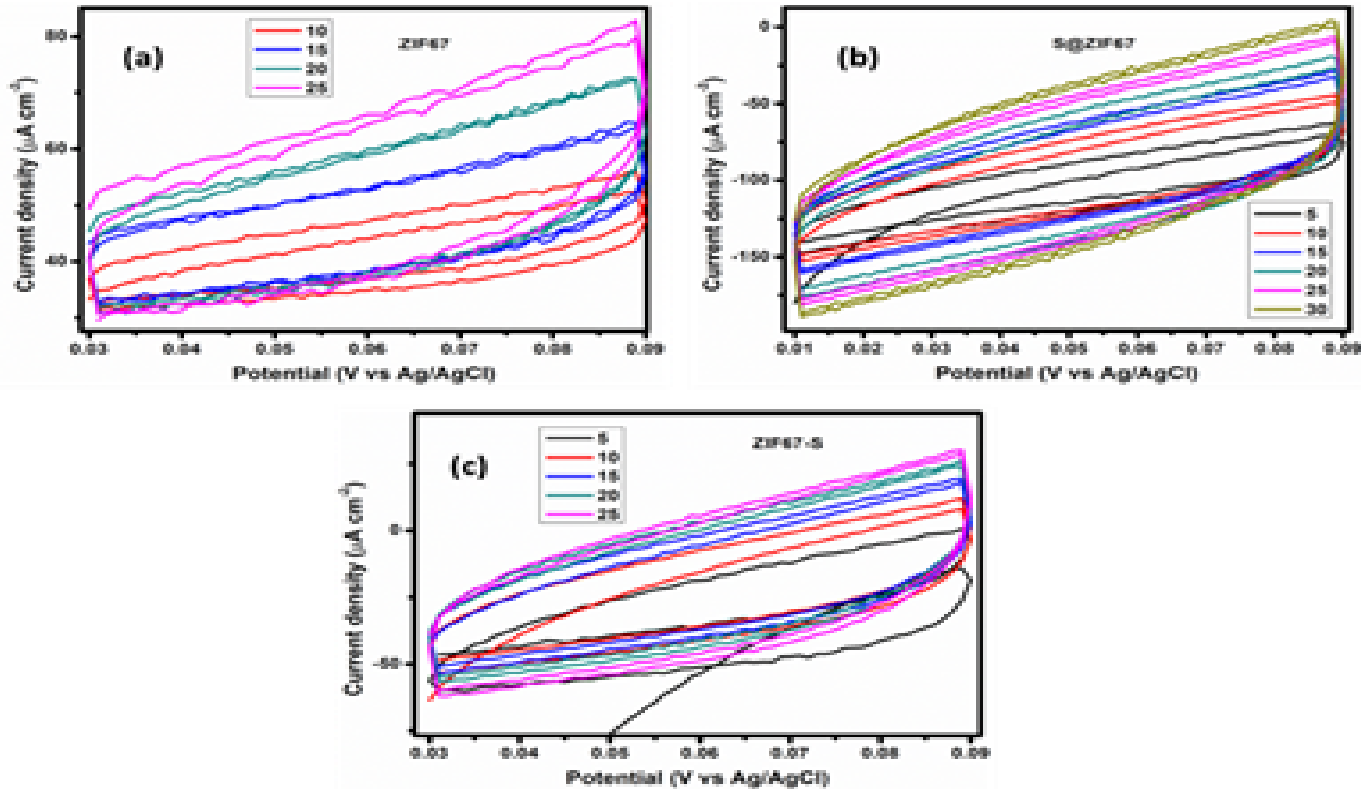

Figure S3: CV curves obtained for (a) ZIF67, (b) S@ZIF67, and (c) ZIF67-S in the non-faradaic region at a scan rate of 50 mV s^{-1} for C_{dl} and ECSA calculations

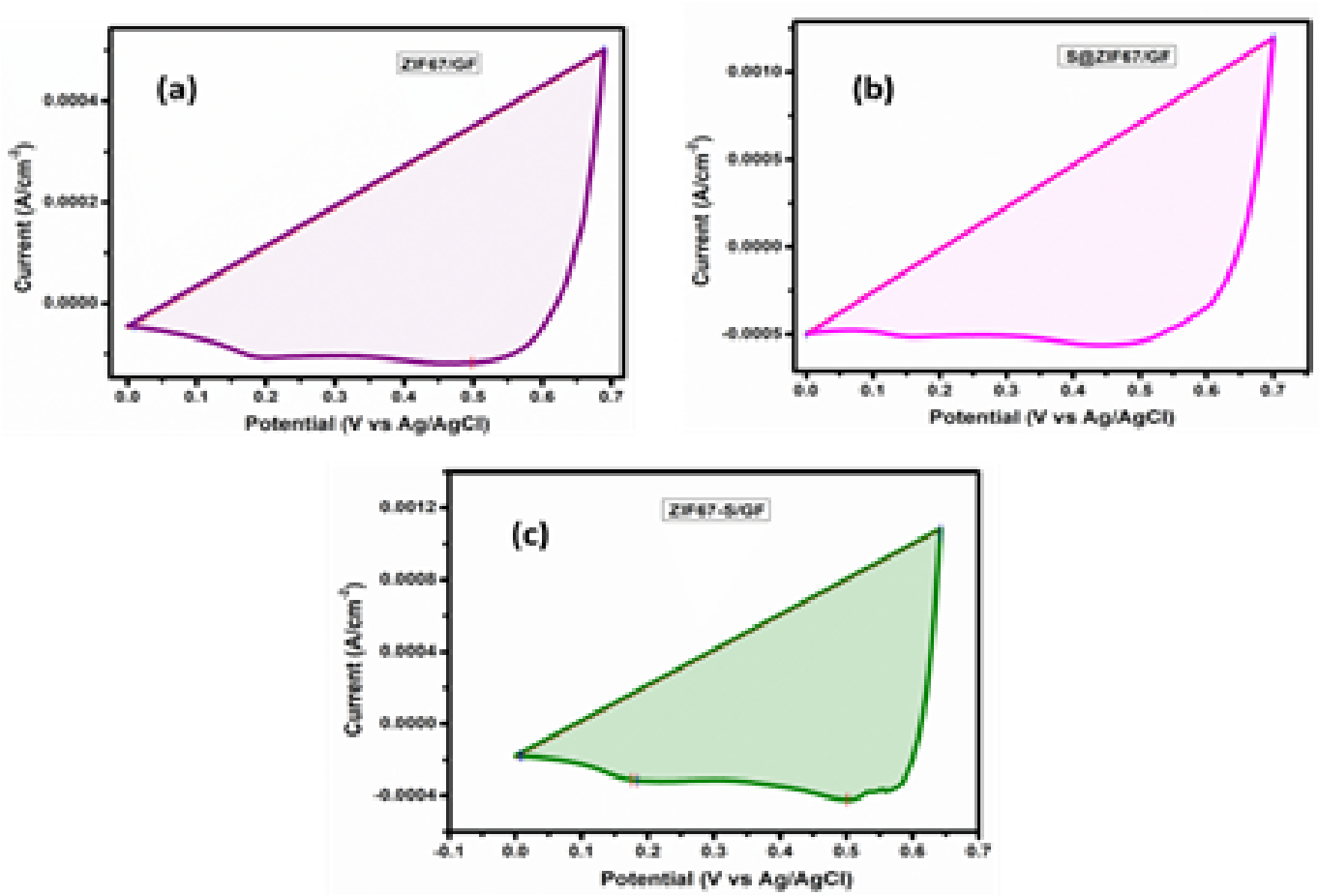

Figure S4: The areas under the reduction peaks of (a) ZIF67, (b) S@ZIF67, and (c) ZIF67-S for the calculation of surface concentaration of active sites

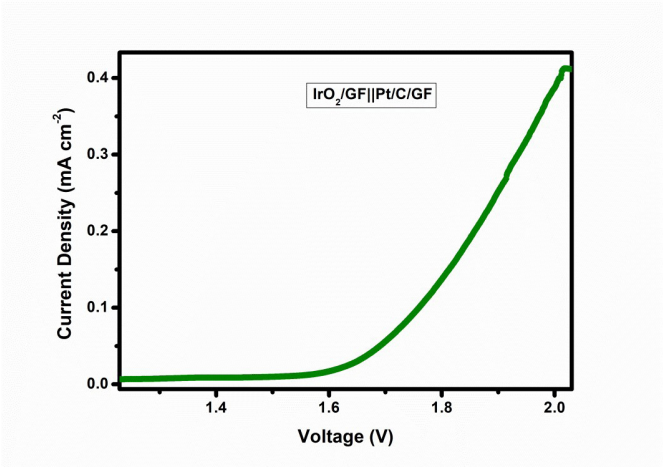

Figure S5: iR-corrected LSV polarization curve of IrO_2/GF||Pt/C/GF in alkaline seawater

Reference

[1] Anantharaj S, Ede SR, Karthick K, Sam Sankar S, Sangeetha K, Karthik PE, et al. Precision and correctness in the evaluation of electrocatalytic water splitting: Revisiting activity parameters with a critical assessment. Energy Environ Sci 11(2018):744. https://doi.org/10.1039/c7ee03457a.

[2] Fathima TKS, Ghosh A, Ramaprabhu S. ZIF67-derived Co–CoO@C nanocomposites as highly efficient and selective oxygen evolution reaction (OER) catalysts for seawater electrolysis. Int J Hydrogen Energy 46(2023)780–93. https://doi.org/10.1016/j.ijhydene.2023.09.122.

Electrolyzers: Evolution, Prospects and Challenges

*Anoop Naikkath[a,b], Venkatesan Natesan[b], Ramanathan Srinivasan[a] and Kothandaraman Ramanujam[b]**

aDepartment of Chemical Engineering, Indian Institute of Technology Madras (IITM), Chennai, India 600036
bDepartment of Chemistry, Indian Institute of Technology Madras (IITM), Chennai, India 600036
**Corresponding author: anoopmeleri@gmail.com & rkraman@iitm.ac.in*

Abstract

Amid escalating climate change, transformation to sustainable energy sources has become imperative. Green hydrogen, produced via water electrolysis, emerges as a crucial element in this transition, offering a carbon-free alternative to fossil fuels. This review outlines the various types of electrolyzers that facilitate green hydrogen production. Alkaline electrolyzers (AEs), proton exchange membrane (PEM) electrolyzers, solid oxide electrolyzers (SOEC), and anion exchange membrane (AEM) electrolyzers each bring unique advantages and operational mechanisms. Furthermore, we discuss the emerging concept of decoupled electrolyzers, which promise enhanced efficiency and safety by separating hydrogen and oxygen evolution processes. Despite the promising potential of green hydrogen, several challenges remain, including high production costs, technological hurdles, and the need for robust infrastructure. This review aims to provide an overview of water electrolysis technologies while addressing the challenges facing the green hydrogen economy, paving the way for future research and development in this vital field.

Keywords: *Green hydrogen, Electrolyzers, Hydrogen economy, Decoupled electrolyzer*

1.Introduction

Global energy consumption has significantly increased in recent decades due to population growth and advancements in personal comfort [1]. According to studies by the International Energy Agency (IEA), fossil fuels remain the primary source of energy supply [2]. However, fossil fuels are expected to be depleted in the near future, and the carbon footprint associated with their use is a major contributor to global warming and climate change [3]. One approach to mitigating climate change and its adverse effects caused by fossil fuels is to gradually transition to energy sources such as wind energy, solar energy, biomass energy, and green hydrogen energy [4-7]. Hydrogen produced without emitting any greenhouse gases into the atmosphere is known as green hydrogen [8]. It uses electricity from renewable sources such as windmills, solar etc. to split water by electrolysis [9, 10]. Among these options, green hydrogen offers several benefits, including the ready and uninterrupted availability of water compared to season-dependent solar and wind energy, and a higher calorific value compared to biomass derived fuels[11]. Renewable energy-driven hydrogen production is also regarded as an effective alternative for mitigating greenhouse gas emissions and combating climate change [12].

Hydrogen can be produced from various feedstocks. The main pathways of hydrogen production and their applications are illustrated in Fig. 1. Among the different sources such as natural gas, coal, naphtha, and water, fossil fuel sources currently dominate hydrogen production [13]. Reports suggest that approximately 78% of hydrogen is produced through fossil fuel reforming, around 18% through coal gasification, and less than 4% through water electrolysis [1, 14]. The reliance on fossil fuels for hydrogen production is due to their lower cost compared to green hydrogen. Hydrogen produced through steam methane reforming and coal gasification costs less than $1/kg, whereas green hydrogen generated from nuclear-powered electricity costs around $3/kg [15]. Similarly, when examining hydrogen consumers, oil refineries, bulk chemical producers, and steel plants currently dominate the market [16, 17]. However, the depletion of fossil fuels and global climate change scenarios could drive the adoption of green hydrogen in the power and transportation sectors [18]. Despite the potential of green hydrogen, this transition may take several decades.

Electrolyzer technology has been known since the early 19th century. During the 19th and early 20th centuries, it was primarily used for ammonia production from hydropower sources [19]. At that time, electrolyzers were based on alkaline systems, and a significant breakthrough was the replacement of hazardous asbestos-based separators with composite material membranes [19]. In the mid-20th century, the advent of polymer chemistry led to the invention of PEM electrolyzers. By the late 20th century, PEM electrolyzer designs had become much more compact, and production capacities had reached a few hundred kilowatts. Since 2010, the integration of photovoltaics with electrolyzer technology has opened new possibilities for renewable energy. Currently, the focus is on developing novel materials and achieving a production level of gigawatt scale, with an emphasis on finding stable materials [20].

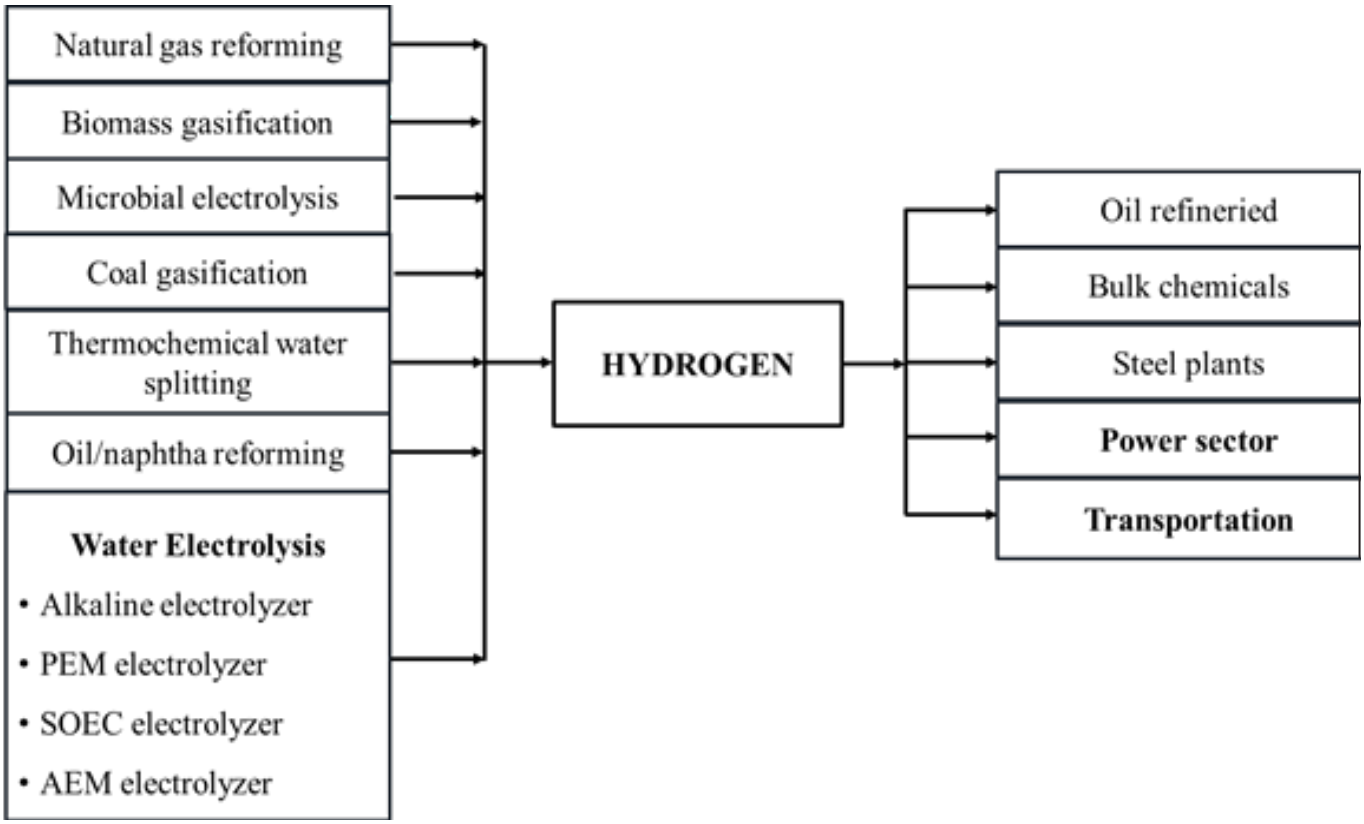

Fig. 1. Various pathways for hydrogen production and its applications (Our focus in this paper and future aspects of hydrogen are highlighted in bold letters)

In this mini review, a brief introduction to water electrolysis is presented. The main types of electrolyzers, viz. alkaline electrolyzers (AE), proton exchange membrane (PEM) electrolyzers, solid oxide (SOEC) electrolyzers, and anion exchange membrane (AEM) electrolyzers are described along with their operating mechanisms. In conventional water electrolysis, the hydrogen evolution reaction (HER) and oxygen evolution reaction (OER) are coupled, which can lead to crossover and, in the worst case, the formation of an explosive H_2/O_2 mixture [21, 22]. A decoupled water electrolyzer can separate the HER and OER reactions. This review also discusses the working mechanism of decoupled water electrolyzers. Despite the significant surge in the field of green hydrogen, many challenges remain. This review highlights the current and expected obstacles to establishing a green hydrogen-based economy.

2. Electrolyzer Technologies and Mechanism

The operational mechanism of hydrogen production differs among various types of electrolyzers, but the fundamental principle remains the same. Electrolysis involves the process of breaking down complex compounds into ions or atoms through the application of electric current. Generally, industrial water electrolyzers can be classified into four categories.

- Alkaline electrolyzers (AE),
- Proton exchange membrane electrolyzers (PEM),
- Solid oxide electrolyzers (SOEC), and
- Anion exchange membrane electrolyzers (AEM).

This categorization is based on the differences in the electrolytes used and the operating conditions. The anodic and cathodic reactions in different electrolyzers are presented in Table 1 and the reactions and separator/membrane details are illustrated in Fig. 2(a)-(d).

Table 1. Half-cell reactions in different types of electrolyzers.

S. No	Type of electrolyzers	Anodic reaction	Cathodic reaction
1	Alkaline electrolyzer	$4OH^- \leftrightarrow 2H_2O + O_2 + 4e^-$	$4H_2O + 4e^- \leftrightarrow 2H_2 + 4OH^-$
2	Proton exchange membrane electrolyzer	$2H_2O \leftrightarrow O_2 + 4H^+ + 4e^-$	$4H^+ + 4e^- \leftrightarrow 2H_2$
3	Solid oxide electrolyzer	$2O^{2-} \leftrightarrow O_2 + 4e^-$	$2H_2O + 4e^- \leftrightarrow 2H_2 + 2O^{2-}$
4	Anion exchange membrane electrolyzer	$4OH^- \leftrightarrow 2H_2O + O_2 + 4e^-$	$4H_2O + 4e^- \leftrightarrow 2H_2 + 4OH^-$

2.1 Alkaline Electrolyzers (AE)

Alkaline water electrolyzers are much more advanced than the other three types of electrolyzers and are considered a commercially matured method for producing cost-effective hydrogen [23]. They utilize readily available and accessible electrolytes, such as sodium hydroxide or potassium hydroxide, which enhances their lifespan and cost-effectiveness [24, 25]. The concentration of alkaline electrolytes may vary from 20% to 30% by weight [26]. Conventional AEs use nickel-based electrodes and porous diaphragm separators [27, 28]. Despite significant advancements in commercial-scale alkaline electrolyzers, there is still a need for improvements in operating current density, compact design, startup time, and safety aspects, such as preventing product crossover [29, 30].

2.2 Proton Exchange Membrane Electrolyzers (PEM)

Proton exchange membrane electrolyzers can operate at lower pH levels, with lower cell voltage

and higher current densities compared to alkaline electrolyzers. Additionally, they have a fast response time and produce high-purity hydrogen. They use a polymer membrane-based electrolyte with platinum and iridium-based cathode and anode respectively. Thus, the high material cost is a drawback of PEM water electrolyzers. Furthermore, cross-permeation at high pressure and the need for dehumidification to remove moisture from the produced hydrogen are also limitations of this technique [31, 32]. With ongoing research on materials and technologies, these challenges can be resolved in the near future.

2.3 Solid Oxide Electrolyzers (SOEC)

Research on solid oxide electrolyzers has gained significant momentum over the past two decades. In solid oxide water electrolyzers, steam is introduced directly to the porous cathode. When sufficient potential is applied, water molecules dissociate at the cathode's active sites, producing hydrogen and oxide ions. These oxide ions then diffuse to the anode, where they oxidize to form oxygen. SOECs operating at high temperatures can generate hydrogen at a faster rate and with lower

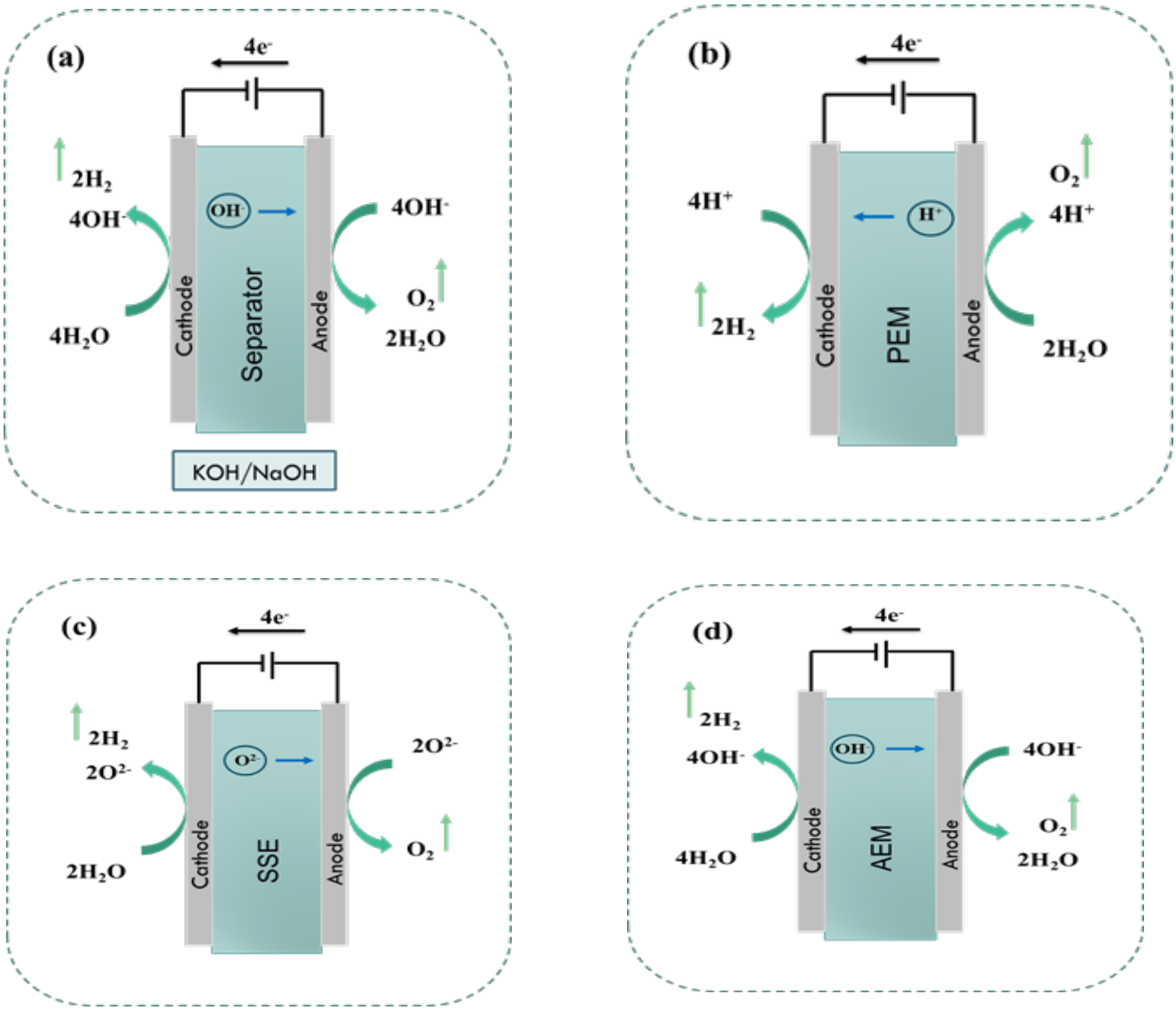

energy input compared to alkaline and PEM electrolyzers [33, 34]. However, the system lifetime of SOEC is much lower compared to the alkaline and PEM electrolyzers [35].

2.4 Anion Exchange Membrane Electrolyzers (AEM)

Anion exchange membrane electrolyzers are relatively new compared to the other water electrolyzers described above. They combine the advantages of alkaline and PEM electrolyzers by using a hydrocarbon-based anion exchange membrane and a less caustic bicarbonate or carbonate-based electrolyte [36, 37]. The AEM electrolyzers are still in the developmental stage and require further improvements in electrode and membrane stability, as well as operating parameters [38, 39]. A list of salient features of these four types of electrolyzers is provided in Table 2.

Fig. 2. The working mechanism of (a) Alkaline electrolyzer (b) Proton exchange membrane electrolyzer (c) Solid oxide electrolyzer (d) Anion exchange membrane electrolyzer.

Table 2. Salient features of different types of electrolyzers [1, 20, 40-42].

Components and parameters	AE	PEM	SOEC	AEM
Operating temperature $(^{\circ}C)$	70-90	50-80	700-850	40-60
Operating pressure (bar)	1-30	30-80	1	< 35
Electrolyte	KOH	Polymer membrane	Yttria-stabilized Zirconia	Divinyl benzene supported with KOH/ $NaHCO_3$
Separator	Asbestos/ Zirfon / NiO	Solid electrolyte	Solid electrolyte	Solid electrolyte
Cathode	Nickel-coated stainless steel	Platinum on carbon black	Yttria-stabilized Zirconia	Nickel (High surface area)
Anode	Nickel-coated stainless steel	Iridium oxide	Nickel mesh or foam	Ni/NiFeCo alloys
Transport layer (cathode)	Nickel mesh	Porous titanium or carbon cloth	Nil	Nickel foam or carbon cloth
Transport layer (anode)	Nickel mesh	Platinum-coated porous titanium	Course Nickel mesh or foam	Nickel foam
Cell voltage (V)	1.8-2.4	1.8-2.2	0.95-1.3	1.8-2.2
Current density (A cm^2)	<0.5	1-2	0.3-1	1-2
Cell area (m^2)	3-3.6	<0.13	<0.06	---
Voltage efficiency (%)	62-82	67-82	81-86	---
System lifetime (years)	20-30	10-20	---	---
Hydrogen purity (%)	99.5	99.999	99.9	99.99
System startup time (min)	15	<15	>60	<15
Technology readiness level	Widely commercialized	Commercialized	R&D	R&D

3. Decoupled Water Electrolysis

Research on decoupled water electrolysis has recently become a notable area in hydrogen production, offering a flexible alternative to existing water electrolysis systems.[43-45]. In conventional water electrolysis, hydrogen and oxygen production are explicitly coupled. For one mole of oxygen produced at the anode, two moles of hydrogen are generated at the cathode. The anodic and cathodic compartments are typically separated by an ion exchange membrane or ion-permeable separator to prevent crossover. However, when electrolyzers operate at a low load, gas crossover can occur, reducing hydrogen production efficiency or, in the worst case, forming an explosive H_2/O_2 mixture.

In a decoupled electrolysis system, OER is

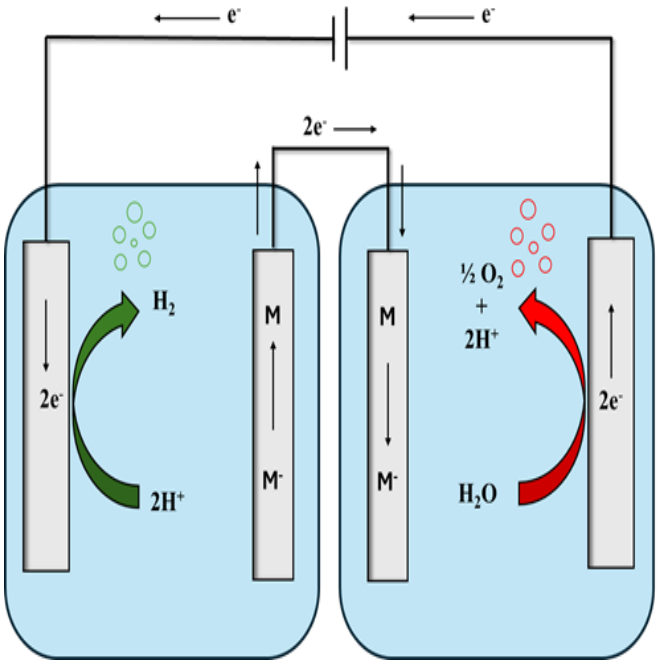

paired with the reduction of a redox mediator, which is subsequently re-oxidized to supply the electron needed for HER. Figure 3 illustrates a decoupled water splitting system. The electrochemical reactions in this system are represented by eqn. (1) and (2). The overall reactions for a decoupled water electrolyzers are the same as those of a conventional electrolyzer (Eqn. 3).

The hydrogen side electrochemical half-cell reactions can be written as

$$2H^+ + 2e^- \rightarrow H_2$$

$$2M^- \rightarrow 2M + 2e^-$$

$$2H^+ + 2M^- \rightarrow H_2 + 2M \qquad (1)$$

On the oxygen evolution side

The overall reaction is

$$H_2O \rightarrow H_2 + \frac{1}{2}O_2 \qquad (3)$$

In the above equations 'M' represents the redox mediator, which decouples the HER and OER reactions. M can be solid materials such as NiOOH/$Ni(OH)_2$ or redox species such as $[Fe(CN)_6]^{3+/4+}$ or $V^{2+/}V^{3+}$ [46]. The advancement of decoupled water electrolyzers can offer several benefits, including eliminating the need for costly membrane systems, generating high-pressure hydrogen without membranes, reducing the risk of H_2 and O_2 mixing, and enhancing flexibility in coupling with renewable energy sources. However, the long-term performance and stability of the decoupled water-splitting systems are yet to be understood.

Fig. 3. A schematic of the decoupled water electrolysis system.

4. Green Hydrogen Economy: Challenges and Future Aspect

Green hydrogen is considered a potential fuel source to replace fossil fuels in the industrial and transportation sectors. However, the transformation to a green hydrogen economy faces several challenges, including financial, scientific, social, and political scenarios. Among the challenges associated with green hydrogen, the

primary concern is its cost [47, 48]. According to the International Renewable Energy Agency (IRENA) reports, green hydrogen production is still in its early stages, and to compete with other forms of hydrogen (such as black and blue hydrogen), its cost must be more comparable [49]. Ammonia production is one of the major industrial sectors that utilize hydrogen in large quantities. Currently, hydrogen for the Haber-

Bosch (H-B) process is primarily produced through steam methane reforming [50]. The dependence on fossil fuels for hydrogen production results from the lower cost of grey hydrogen compared to other forms of hydrogen, as discussed in the introduction section. Ammonia production with green hydrogen is significantly more expensive compared to ammonia production using SMR hydrogen [51]. In the short term, imposing carbon taxes is the only viable way to promote the use of green or blue hydrogen for ammonia production [52]. However, recent techno-economic studies suggest that a carbon tax of at least \$62 per ton of CO_2 is necessary to make blue hydrogen a competitive raw material for ammonia production [53]. In addition, the cost of electrolyzers and electricity has a significant impact on the green hydrogen cost. Even though the price of renewable electricity from solar and wind energy has dropped significantly in the past decade, the investment cost in hydrogen electrolyzers remains substantial [54].

Beyond cost considerations, the green hydrogen initiative faces challenges related to the absence of global standards and social support. [55]. Therefore, a global framework and strategy are essential for establishing universal hydrogen terminology and standards [56]. While the research framework demonstrates the technical feasibility of green hydrogen, social acceptance is equally important. The primary concern among the public revolves around the risk of explosions at hydrogen (H_2) refueling stations [57]. Studies indicate that families are more likely to oppose the establishment of such stations near their residences, due to safety concerns [58]. This concern will be more prominent in developing and underdeveloped nations. Effective communication is essential to address safety concerns related to hydrogen (H_2) and to clarify misunderstandings. Alongside all these challenges, the availability of water and land will also impact the global outlook on green hydrogen projects.

Despite these challenges, the future potential of the green hydrogen market remains huge. It promises to reduce emissions across industries, transportation, power systems, and buildings. Green hydrogen can also drive the development of renewable energy sources and enhance the flexibility of the power system. Furthermore, it serves as a long-term energy storage solution to balance seasonal energy variations. A lot of R&D and scaling-up efforts are needed to make a large-scale implementation of green hydrogen a reality.

5. Conclusions

Green hydrogen can play a crucial role in combating climate change as it provides a carbon-free energy source that can significantly reduce greenhouse gas emissions from industries, transportation, power generation, etc. In this review , we described various types of water electrolyzers and their mechanisms. Among the four major technologies, alkaline and PEM electrolyzers are well-established, whereas SOECs and AEM electrolyzers are still in the R&D stage. Safety in water electrolysis remains a concern, and we briefly explore the mechanism of decoupled electrolyzers which can address the safety concerns. Despite the significant interest in hydrogen energy, the hydrogen economy has a long way to go before its widespread adaptation becomes a reality.

Acknowledgment

The authors acknowledge funding through the Energy Consortium- IIT Madras (SP/2223/1245/CPETWO/EGYHOC and SB/2324/1531/CPAAAA/EGYHOC). A.N. acknowledges the Department of Education, India for the PMRF fellowship.

Declaration of competing interest

The authors declare that they have no known competing financial interests or personal relationships that could have appeared to influence the work reported in this article.

References

[1] M. David, C. Ocampo-Martínez, R. Sánchez Peña, Advances in alkaline water electrolyzers: A review, Journal of Energy Storage 23 (2019) 392-403. https://doi.org/10.1016/j.est.2019.03.001.

[2] I.E. Agency, Key World Energy Statistics, International Energy Agency (2016).

[3] K.O. Yoro, M.O. Daramola, CO_2 emission sources, greenhouse gases, and the global warming effect, Advances in carbon capture, Elsevier2020, pp. 3-28. https://doi.org/10.1016/B978-0-12-819657-1.00001-3.

[4] K. Govindan, Pathways to low carbon energy transition through multi-criteria assessment of offshore wind energy barriers, Technological Forecasting Social Change 187 (2023) 122131. https://doi.org/10.1016/j.techfore.2022.122131.

[5] C.M.S. Kumar, S. Singh, M.K. Gupta, Y.M. Nimdeo, R. Raushan, A.V. Deorankar, T.A. Kumar, P.K. Rout, C. Chanotiya, V.D. Pakhale, Solar energy: A promising renewable source for meeting energy demand in Indian agriculture applications, Sustainable Energy Technologies Assessments 55 (2023) 102905. https://doi.org/10.1016/j.seta.2022.102905.

[6] S.W. Sharshir, A. Joseph, M.M. Elsayad, A.A. Tareemi, A.W. Kandeal, M.R. Elkadeem, A review of recent advances in alkaline electrolyzer for green hydrogen production: Performance improvement and applications, International Journal of Hydrogen Energy 49 (2024) 458-488. https://doi.org/10.1016/j.ijhydene.2023.08.107.

[7] C. Wang, S.A. Raza, T.S. Adebayo, S. Yi, M.I. Shah, The roles of hydro, nuclear and biomass energy towards carbon neutrality target in China: a policy-based analysis (vol 262, 125303, 2022), Energy 272 (2023) 125303. https://doi.org/10.1016/j.energy.2023.126994.

[8] A.V. Abad, P.E. Dodds, Green hydrogen characterisation initiatives: Definitions, standards, guarantees of origin, and challenges, Energy Policy 138 (2020) 111300. https://doi.org/10.1016/j.enpol.2020.111300.

[9] G. Weidong, Y. Zhuoyong, Research on non-grid-connected wind power/water-electrolytic hydrogen production system, International Journal of Hydrogen Energy 37(1) (2012) 737-740. https://doi.org/10.1016/j.ijhydene.2011.04.109.

[10] W.W. Clark II, The green hydrogen paradigm shift: Energy generation for stations to vehicles, Utilities Policy 16(2) (2008) 117-129. https://doi.org/10.1016/j.jup.2007.11.010.

[11] A. Hussain, A.S. Nishat, The Energy Challenge: Moving from Fossil Fuels to Biofuels, Hydrogen, and Green Energy Sources, (2022).

[12] M. Benghanem, A. Mellit, H. Almohamadi, S. Haddad, N. Chettibi, A.M. Alanazi, D. Dasalla, A. Alzahrani, Hydrogen Production Methods Based on Solar and Wind Energy: A Review, Energies 16(2) (2023) 757. https://doi.org/10.3390/en16020757.

[13] M.G. Sürer, H.T. Arat, State of art of hydrogen usage as a fuel on aviation, European Mechanical Science 2(1) (2018) 20-30. https://doi.org/10.26701/ems.364286.

[14] D.Y. Lee, A. Elgowainy, Q. Dai, Life cycle greenhouse gas emissions of hydrogen fuel production from chlor-alkali processes in the United States, Applied Energy 217 (2018) 467-479. https://doi.org/10.1016/j.apenergy.2018.02.132.

[15] P. Parthasarathy, K.S. Narayanan, Hydrogen production from steam gasification of biomass: influence of process parameters on hydrogen yield–a review, Renewable energy 66 (2014) 570-579. https://doi.org/10.1016/j.renene.2013.12.025.

[16] W.G. Liu, H.B. Zuo, J.S. Wang, Q.G. Xue, B.L. Ren, F. Yang, S.L. Co, The production and application of hydrogen in steel industry, International Journal of Hydrogen Energy 46(17) (2021) 10548-10569. https://doi.org/10.1016/j.ijhydene.2020.12.123.

[17] R. Ramachandran, R.K. Menon, An overview of industrial uses of hydrogen, International Journal of Hydrogen Energy 23(7) (1998) 593-598. https://doi.org/10.1016/S0360-3199(97)00112-2.

[18] H.C. Lau, The role of fossil fuels in a hydrogen economy, International Petroleum Technology Conference, IPTC, 2021, p. D012S045R191.

[19] D.M.F. Santos, C.A.C. Sequeira, J.L. Figueiredo, Hydrogen Production by Alkaline Water Electrolysis, Quim Nova 36(8) (2013) 1176-1193. https://doi.org/10.1590/S0100-40422013000800017.

[20] E. Taibi, R. Miranda, M. Carmo, H. Blanco, Green hydrogen cost reduction, International Renewable Energy Agency (IRENA) (2020).

[21] H. Janssen, J.C. Bringmann, B. Emonts, V. Schroeder, Safety-related studies on hydrogen production in high-pressure electrolysers, International Journal of Hydrogen Energy 29(7) (2004) 759-770. https://doi.org/10.1016/j.ijhydene.2003.08.014.

[22] S.A. Grigoriev, V.I. Porembskiy, S.V. Korobtsev, V.N. Fateev, F. Auprêtre, P. Millet, High-pressure PEM water electrolysis and corresponding safety issues, International Journal of Hydrogen Energy 36(3) (2011) 2721-2728. https://doi.org/10.1016/j.ijhydene.2010.03.058.

[23] C. Daoudi, T. Bounahmidi, Overview of alkaline water electrolysis modeling, International Journal of Hydrogen Energy 49 (2024) 646-667. https://doi.org/10.1016/j.ijhydene.2023.08.345.

[24] S. Marini, P. Salvi, P. Nelli, R. Pesenti, M. Villa, M. Berrettoni, G. Zangari, Y. Kiros, Advanced alkaline water electrolysis, Electrochimica Acta 82 (2012) 384-391. https://doi.org/10.1016/j.electacta.2012.05.011.

[25] Z.Y. Yu, Y. Duan, X.Y. Feng, X. Yu, M.R. Gao, S.H. Yu, Clean and Affordable Hydrogen Fuel from Alkaline Water Splitting: Past, Recent Progress, and Future Prospects, Advanced Materials 33(31) (2021) e2007100. https://doi.org/10.1002/adma.202007100.

[26] D. Aili, M.R. Kraglund, J. Tavacoli, C. Chatzichristodoulou, J.O. Jensen, Polysulfone-polyvinylpyrrolidone blend membranes as electrolytes in alkaline water electrolysis, Journal of Membrane Science 598 (2020) 117674. https://doi.org/10.1016/j.memsci.2019.117674.

[27] D. Aili, M.R. Kraglund, S.C. Rajappan, D. Serhiichuk, Y. Xia, V. Deimede, J. Kallitsis, C. Bae, P. Jannasch, D. Henkensmeier, J.O. Jensen, Electrode Separators for the Next-Generation Alkaline Water Electrolyzers, ACS Energy Letters 8(4) (2023) 1900-1910. https://doi.org/10.1021/acsenergylett.3c00185.

[28] V.N. Kuleshov, S.V. Kurochkin, N.V. Kuleshov, A.A. Gavrilyuk, I.V. Pushkareva, M.A. Klimova, O.Y. Grigor'eva, Alkaline Water Electrolysis with Anion-Exchange Membranes and Nickel-Based Catalysts, Russian Journal of Electrochemistry 59(11) (2023) 915-929. https://doi.org/10.1134/S1023193523110101.

[29] Q. Cai, W. Hong, C. Jian, X. He, W. Liu, Recent Development of Self-Supported Alkaline Hydrogen Evolution Reaction Electrocatalysts for Industrial Electrolyzer, Advanced Energy Sustainability Research 4(6) (2023) 2200178. https://doi.org/10.1002/aesr.202200178.

[30] F. Gambou, D. Guilbert, M. Zasadzinski, H. Rafaralahy, A Comprehensive Survey of Alkaline Electrolyzer Modeling: Electrical Domain and Specific Electrolyte Conductivity, Energies 15(9) (2022) 3452. https://doi.org/10.3390/en15093452.

[31] M. Carmo, D.L. Fritz, J. Merge, D. Stolten, A comprehensive review on PEM water electrolysis, International Journal of Hydrogen Energy 38(12) (2013) 4901-4934. https://doi.org/10.1016/j.ijhydene.2013.01.151.

[32] D. Falcão, Pinto, A review on PEM electrolyzer modelling: Guidelines for beginners, AMFR Journal of cleaner production 261 (2020) 121184. https://doi.org/10.1016/j.jclepro.2020.121184.

[33] M. Ni, M.K.H. Leung, D.Y.C. Leung, Technological development of hydrogen production by solid oxide electrolyzer cell (SOEC), International Journal of Hydrogen Energy 33(9) (2008) 2337-2354. https://doi.org/10.1016/j.ijhydene.2008.02.048.

[34] Y.F. Tian, N. Abhishek, C.C. Yang, R. Yang, S. Choi, B. Chi, J. Pu, Y.H. Ling, J.T.S. Irvine, G. Kim, Progress and potential for symmetrical solid oxide electrolysis cells, Matter 5(2) (2022) 482-514. https://doi.org/10.1016/j.matt.2021.11.013.

[35] A. Nechache, S. Hody, Alternative and innovative solid oxide electrolysis cell materials: A short review, Renewable & Sustainable Energy Reviews 149 (2021) 111322. https://doi.org/10.1016/j.rser.2021.111322.

[36] C.Q. Li, J.B. Baek, The promise of hydrogen production from alkaline anion exchange membrane electrolyzers, Nano Energy 87 (2021) 106162. https://doi.org/10.1016/j.nanoen.2021.106162.

[37] K. Ham, S. Hong, S. Kang, K. Cho, J. Lee, Extensive Active-Site Formation in Trirutile $CoSb_2O_6$ by Oxygen Vacancy for Oxygen Evolution Reaction in Anion Exchange Membrane Water Splitting, ACS Energy Letters 6(2) (2021) 364-370. https://doi.org/10.1021/acsenergylett.0c02359.

[38] P. Shirvanian, A. Loh, S. Sluijter, X. Li, Novel components in anion exchange membrane water electrolyzers (AEMWE's): Status, challenges and future needs. A mini review, Electrochemistry Communications 132 (2021) 107140. https://doi.org/10.1016/j.elecom.2021.107140.

[39] I. Vincent, D. Bessarabov, Low cost hydrogen production by anion exchange membrane electrolysis: A review, Renewable & Sustainable Energy Reviews 81 (2018) 1690-1704. https://doi.org/10.1016/j.rser.2017.05.258.

[40] I. Dincer, C. Acar, Review and evaluation of hydrogen production methods for better sustainability, International Journal of Hydrogen Energy 40(34) (2015) 11094-11111. https://doi.org/10.1016/j.ijhydene.2014.12.035.

[41] A. Buttler, H. Spliethoff, Current status of water electrolysis for energy storage, grid balancing and sector coupling via power-to-gas and power-to-liquids: A review, Renewable & Sustainable Energy Reviews 82 (2018) 2440-2454. https://doi.org/10.1016/j.rser.2017.09.003.

[42] Q. Xu, L. Zhang, J. Zhang, J. Wang, Y. Hu, H. Jiang, C. Li, Anion exchange membrane water electrolyzer: electrode design, lab-scaled testing system and performance evaluation, EnergyChem 4(5) (2022) 100087. https://doi.org/10.1016/j.enchem.2022.100087.

[43] Z.P. Ifkovits, J.M. Evans, M.C. Meier, K.M. Papadantonakis, N.S. Lewis, Decoupled electrochemical water-splitting systems: a review and perspective, Energy & Environmental Science 14(9) (2021) 4740-4759. https://doi.org/10.1039/d1ee01226f.

[44] A. Paul, M.D. Symes, Decoupled electrolysis for water splitting, Current Opinion in Green and Sustainable Chemistry 29 (2021) 100453. https://doi.org/10.1016/j.cogsc.2021.100453.

[45] A.G. Wallace, M.D. Symes, Decoupling Strategies in Electrochemical Water Splitting and Beyond, Joule 2(8) (2018) 1390-1395. https://doi.org/10.1016/j.joule.2018.06.011.

[46] L. Chen, X. Dong, Y. Wang, Y. Xia, Separating hydrogen and oxygen evolution in alkaline water electrolysis using nickel hydroxide, Nature Communications 7(1) (2016) 11741. https://doi.org/10.1038/ncomms11741.

[47] H. Insights, A perspective on hydrogen investment, market development and cost competitiveness, Hydrogen Council (2021).

[48] H. Council, Path to hydrogen competitiveness: a cost perspective, (2020).

[49] IRENA, Making the breakthrough: green hydrogen policies and technology costs, Abu Dhabi: International Renewable Energy Agency (2021).

[50] A. Dechany, K. Van Geem, J. Proost, Process implications of electrifying ammonia production, Current Opinion in Chemical Engineering 40 (2023) 100915. https://doi.org/10.1016/j.coche.2023.100915.

[51] J.R. Bartels, A feasibility study of implementing an Ammonia Economy, Iowa State University2008.

[52] S. Park, Y. Shin, E. Jeong, M. Han, Techno-economic analysis of green and blue hybrid processes for ammonia production, Korean Journal Chemical Engineering 40(11) (2023) 2657-2670. https://doi.org/10.1007/s11814-023-1520-1.

[53] S. Oh, H. Mun, J. Park, I. Lee, Techno-economic comparison of ammonia production processes under various carbon tax scenarios for the economic transition from grey to blue ammonia, Journal of Cleaner Production 434 (2024) 139909. https://doi.org/10.1016/j.jclepro.2023.139909.

[54] R. Agarwal, Transition to a Hydrogen-Based Economy: Possibilities and Challenges, Sustainability 14(23) (2022) 15975. https://doi.org/10.3390/su142315975.

[55] S.O. Bade, O.S. Tomomewo, A. Meenakshisundaram, P. Ferron, B.A. Oni, Economic, social, and regulatory challenges of green hydrogen production and utilization in the US:

A review, International Journal of Hydrogen Energy 49 (2024) 314-335. https://doi.org/10.1016/j.ijhydene.2023.08.157.

[56] R. Scita, P.P. Raimondi, M. Noussan, Green hydrogen: the holy grail of decarbonisation? An analysis of the technical and geopolitical implications of the future hydrogen economy, FEEM Working Paper Series (2020). https://doi.org/10.2139/ssrn.3709789.

[57] J.A. Gordon, N. Balta-Ozkan, S.A. Nabavi, Beyond the triangle of renewable energy acceptance: The five dimensions of domestic hydrogen acceptance, Applied Energy 324 (2022) 119715. https://doi.org/10.1016/j.apenergy.2022.119715.

[58] S.M. Han, J.H. Kim, S.H. Yoo, The public's acceptance toward building a hydrogen fueling station near their residences: The case of South Korea, International Journal of Hydrogen Energy 47(7) (2022) 4284-4293. https://doi.org/10.1016/j.ijhydene.2021.11.106.

The Evolution of Hydrogen Production Catalysts from Enzymes to Artificial Bio-Hybrid Systems

Abhishek Saini[a], Piyali Majumder[b], and Arnab Dutta[a,b,c,d]*

[a]*Chemistry Department, Indian Institute of Technology Bombay, Mumbai, Maharashtra, India-400076.*

[b]*UrjanovaC Pvt. Ltd., Powai, Mumbai, Maharashtra, India-400076.*

[c]*Centre for Climate Studies, Indian Institute of Technology Bombay, Mumbai Maharashtra, India-400076*

[d]*National Centre of Excellence in Carbon Capture and Utilization, Mumbai Maharashtra, India-400076*

* *Corresponding author* arnab.dutta@iitb.ac.in

Abstract

The production of hydrogen, a clean and sustainable energy carrier, has been a major focus of research in recent decades. Hydrogenase enzymes, have long set the benchmark for efficiency in hydrogen production, catalyzing the reversible conversion of protons to molecular hydrogen with a remarkable speed and minimal overpotential requirement. However, their sensitivity to oxygen and instability beyond their native environment present significant challenges for their direct practical applications. This review explores the journey from natural hydrogenase enzymes to synthetic and bio-hybrid systems designed to understand its mechanism and overcome these limitations. We trace the evolution of hydrogen production technologies, beginning with the mimicry of hydrogenase active sites using small-molecule catalysts and progressing to the incorporation of these catalysts into protein frameworks. The review discusses key challenges, including sensitivity, scalability, integration into devices, and highlights future perspectives, such as the development of bio-inspired catalysts and their potential in creating next-generation hydrogen production systems. By examining these developments, we underscore the progress made in strategic replicating and surpassing the efficiency of natural hydrogenases, paving the way for more robust and scalable hydrogen production technologies for a greener future.

Keywords: Electrocatalytic Hydrogen Production, Hydrogenase, Biomimetic Catalyst Design, Artificial Metalloprotein, Metallopeptide.

Introduction

The global pursuit of sustainable energy solutions has positioned hydrogen as a critical component in the transition to a low-carbon economy and future energy systems.[1] As an energy carrier, hydrogen offers a clean and versatile solution, capable of powering a wide range of applications, from transportation to industrial processes.[2] However, the efficient and environmentally friendly scalable production of hydrogen remains a formidable challenge, particularly in a world seeking to reduce its reliance on fossil fuels.[3,4] In nature, the enzyme Hydrogenase provides an elegant and efficient route for hydrogen production, catalyzing the reversible conversion of protons to hydrogen under ambient conditions.[5] Hydrogenase enzymes, primarily found in microorganisms, have evolved to perform this task

with extraordinary catalytic efficiency, making them a benchmark for hydrogen production (**Fig. 1**). These enzymes operate with high turnover frequencies and minimal overpotential, setting a standard that synthetic systems strive to achieve.[6] However, the existing technologies, such as photoelectrochemical cells, electrolyzers, and proton-exchange-membrane fuel cells (PEMFC), utilizes platinum (Pt) or palladium (Pd)-based materials due to its exceptional catalytic abilities.[7] Interestingly, hydrogenases have emerged as a potential rival to state-of-the-art catalyst Pt, while utilizing only first-row transition metals, specifically nickel and/or iron, at their active sites.[8,9] This makes them a promising alternative to expensive and sparsely available platinum in the green hydrogen technologies. Despite their impressive natural efficiency, hydrogenase enzymes face significant challenges when considered for practical applications. One of the major issues is their inherent sensitivity to oxygen, which can irreversibly inactivate the enzyme. This oxygen sensitivity limits their use in environments where oxygen is present, such as in industrial settings or in open-air conditions.[6,10–12] Additionally, the stability of hydrogenase enzymes outside their native biological contexts is often compromised, making it difficult to integrate them into engineered systems.[13,14] The complexity of these enzymes also poses challenges for large-scale production and integration into devices like electrolyzers, where stability, scalability, and cost are critical parameters. These challenges have spurred extensive research into mimicking the function of hydrogenase through synthetic catalysts, proteins, peptides and bio-hybrids.[15,16] By replicating the active site of hydrogenase using small molecular complexes, researchers aim to capture the enzyme's catalytic prowess while overcoming its limitations. This biomimetic approach has led to the development of an array of synthetic catalysts that, while promising, often fall short of replicating the full efficiency and robustness of natural hydrogenase.[17,18] In parallel, there has been a growing interest in exploring proteins and peptides as alternative platforms for hydrogen production. These biological scaffolds [also defined as the outer coordination sphere (OCS)], offer unique advantages, including biocompatibility, structural versatility, and the potential for fine-tuning catalytic environments. By incorporating molecular catalysts into proteins, researchers have been able to create bio-hybrid systems that combine the catalytic strength of synthetic complexes with the sophisticated structural control inherent to biological molecules.[19,20] This approach represents a significant advancement, moving closer to the goal of replicating the efficiency of natural hydrogenase in a stable and scalable form. This review traces the evolution of hydrogen production strategies, beginning with the pioneering studies on hydrogenase enzymes and extending to the most recent developments in protein- and peptide-based systems. We will explore the key milestones and innovations in the field, culminating in a unique future direction, where we discussed the possibility of integrating a molecular catalyst into stable protein scaffolds and utilize them for H_2 production in electrolyzer assembly. This review not only addresses some of the fundamental challenges associated with hydrogenase but also opens new possibilities for sustainable hydrogen Productions

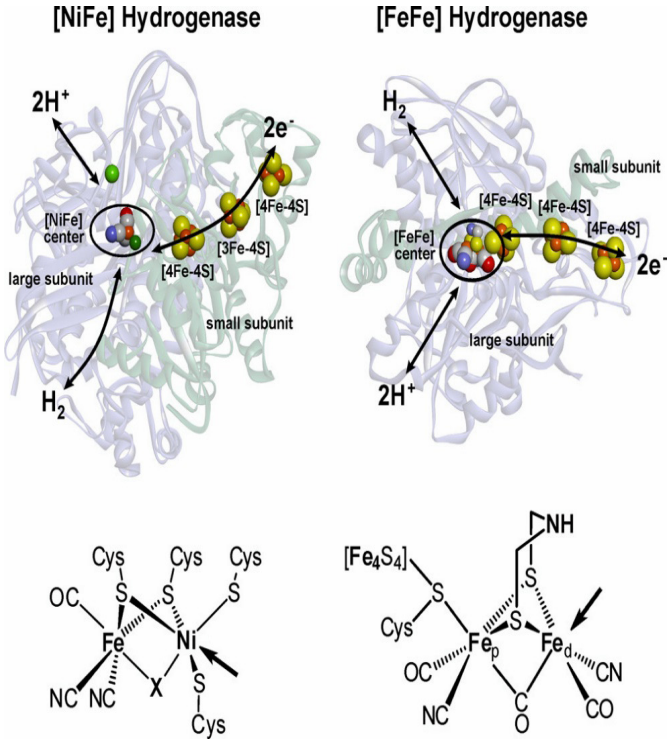

Figure 1. The structures of the [NiFe] hydrogenase from *DvMF*[21] and the [FeFe] hydrogenase from *Dd*[22] are depicted, along with schematic representations of the electron transfer (ET) chain via iron–sulfur centers, as well as pathways for dihydrogen (H_2) and proton (H^+) transfer. At the bottom, the chemical structures of the active sites for both types of hydrogenases are shown, with arrows indicating the open metal coordination sites. The figure is taken from ref [6], copyright ACS [2014].

Hydrogenase Enzymes: Nature's Own H_2 production Unit

The study of certain organisms, including bacteria, archaea, and algae, has led to the remarkable discovery that hydrogen can be both produced and utilized as a source of low-potential electrons within living cells, playing a role in a global hydrogen cycle.[23] A notable example is the bacterium *Ralstonia eutropha*, a chemolithoautotrophic organism, that uses hydrogen as its sole energy source.[24] Similarly, microalgae like *Chlamydomonas reinhardtii*, under specific conditions, can harness sunlight to reverse the typical reaction, i.e. reducing H^+ into H_2 by extracting electrons from water.[24,25] This remarkable biochemical process is enabled by metalloenzymes known as *Hydrogenases*.[24,26] These metalloenzymes are a diverse group that catalyze one of the simplest molecular reactions: the conversion of dihydrogen into protons and electrons, as well as the reverse process, the generation of dihydrogen.[27]

$$H_2 (\rightleftharpoons H^+ + H^-) \rightleftharpoons 2H^+ + 2e^- \qquad \textbf{(Equation 1)}$$

This reaction occurs at a specialized metal center, which significantly enhances the acidity of H_2, leading to its heterolytic splitting—a process strongly accelerated by the presence of a nearby base. The reverse reaction, the synthesis of H_2, involves the coupling of H^+ and H^-. Based on the metal ions in their active sites, hydrogenases are categorized as [FeFe] and [NiFe] hydrogenases **(Fig.1)**, which perform the catalysis of these reactions at minimal overpotential and at remarkably high rates, converting 1,500 to 20,000 molecules of H_2 per second at 37°C in neutral water.[28–30] The third type, [Fe]-hydrogenase, also known as Hydrogen-forming methylene-tetrahydromethanopterin dehydrogenase (Hmd), is unique to methanogenic archaea, where it activates H_2 only in the presence of a hydride (H^-) acceptor/donor substrate necessary for the reaction.[31] [FeFe]-hydrogenases are distinguished by a sophisticated active site known as the H-cluster, which comprises a [2Fe] subcluster or diiron center connected to a [4Fe-4S] cubane cluster.[22,32] The diiron center is coordinated by carbon monoxide (CO) and cyanide (CN^-) ligands which was first detected by FTIR spectroscopy, are essential for catalysis.[33,34] These

ligands act as strong π-accepting ligands to iron, facilitating metal-to-ligand back bonding resulting in the stabilization of the low oxidation states of iron. Additionally, several hydrogen bonds to the CN^- ligands help stabilize a specific orientation of the diiron subcluster within the active site.[35,36] The [4Fe-4S] cluster plays a critical role in electron transfer, enabling the efficient reduction of H^+ to H_2.[37] Conversely, [NiFe]-hydrogenases feature a bimetallic active site composed of nickel and iron ions, with the iron ion similarly coordinated by CO and CN^- ligands. The Ni site of the enzyme participates directly in catalysis, while specifically positioned surrounding iron-sulfur clusters {[3Fe,4S], [4Fe,4S]} provide pathways for electron transfer.[38,39] The high-field of CO and CN^- ligands stabilize the iron center which remains in a low-spin Fe(II) state, while the nickel center alternates between Ni(II) and Ni(III) oxidation states.[40] Hence, in both the cases, the active site is embedded in an augmented protein matrix that provides ligands for the metal ions and creates a pocket for the catalytic reaction, along with the channels for products and reactants to reach the protein surface. Generally, [NiFe]-hydrogenases are more active towards H_2 oxidation, while [FeFe]-hydrogenases excel in Hydrogen Evolution Reaction (HER). However, depending on their cellular location, hydrogenases can be modulated for either hydrogen evolution or uptake.[6,12,41] The intricate architecture of these enzymes ensures a highly efficient catalytic process, finely tuned by the enveloping protein environment. However, despite this finely tuned architecture, several challenges arise when working with hydrogenase in terms of stability. The enzyme's sensitivity to oxygen is one of the most significant hurdles, as exposure to even trace amounts can result in irreversible inactivation. Furthermore, maintaining the enzyme's structural integrity under varying thermal conditions is difficult, with high temperatures often leading to denaturation. Additionally, the enzyme's performance is highly dependent on pH, as deviations from its optimal range can disrupt the catalytic efficiency and long-term stability, making it challenging to maintain activity in diverse environments.

Hydrogenase Mimics: Challenges and Progress

Intense research is currently focused on understanding the mechanism of enzymatic function, particularly the inactivation by O_2, and on the detailed characterization of the few O_2-tolerant hydrogenases.[42,43] Therefore, designing active site analogues through a biomimetic approach is crucial for developing stable, noble-metal-free catalysts for H_2 evolution and uptake.[44,45] Over the past two decades, more than 400 new systems have been developed, focusing on mimicking the key features of the [FeFe] and [NiFe] hydrogenase in a synthetic platform.[46,47] However, many of these compounds closely resemble the natural site but employ abiological phosphine or carbene ligands, resulting in electrocatalytic proton reduction albeit at high overpotential requirements.[48–50] The synthesis of dithiolate-bridged hexacarbonyl diiron complexes, which is an analogue of the active site for [FeFe]-hydrogenases, dates back to 1929 with the work of Reihlen and colleagues.[51]

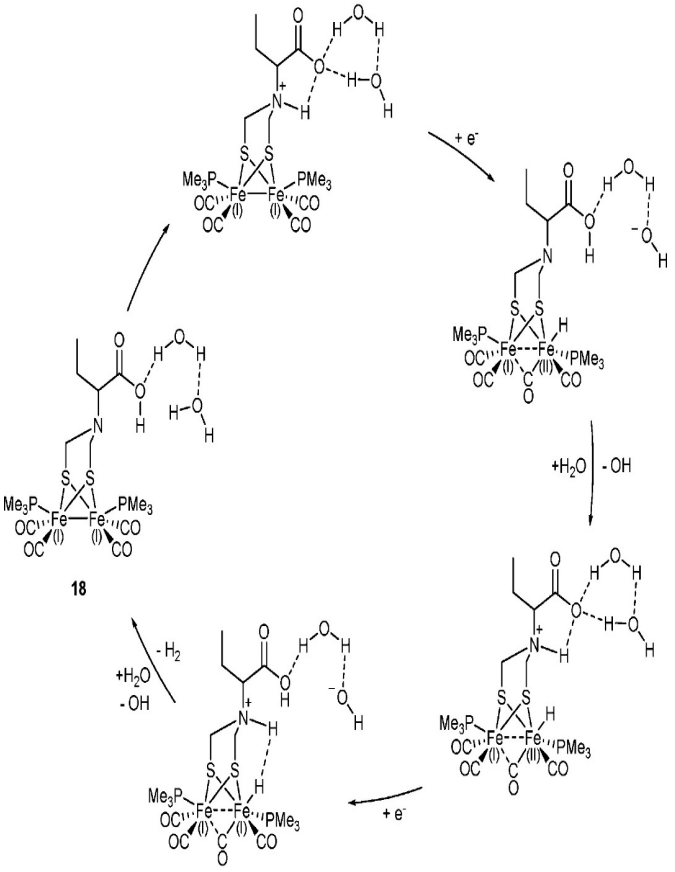

Figure 2: Proposed catalytic mechanism for the electrocatalytic reduction of H^+ in aqueous media, illustrating the mooted role of the carboxylate group as a proton transfer relay. This figure is taken from ref. [18], copyright ELSEVIER [2014]

Recent research has explored the impact of modifying the bridging group in [FeFe]-mimics, particularly by using higher group chalcogens to replace bridging dithiolates, leading to varied effects on electrocatalytic H^+ reduction.[52–56] For instance, Hou et al. synthesized an [FeFe]-mimic with a diselenolate bridge, which showcased activity towards H^+ reduction using p-toluenesulfonic acid.[57] Next, to design diiron model systems with redox properties closer to the thermodynamic potential for H^+ reduction, researchers have explored the inclusion of substituted aromatic dithiolato bridgeheads.[58] **(Fig. 2)** Another critical factor influencing the enhanced performance of enzymes is the difference between bridging and terminal binding modes of hydrides.[59,60] While most hydride models exhibit a bridging configuration and serve as active electrocatalysts for proton reduction, many studies were conducted towards the comparative catalytic studies on terminal hydride derivatives. These studies provided valuable insights into the bias of natural system toward a specific hydride mode (bridging versus terminal) and the underlying reasons for such a preference.[50] Rauchfuss and co-workers later conducted detailed investigations into the role of proton relays, suggesting that incorporating a pendant base group, like an azadithiolate bridge, would kinetically favor the formation of terminal hydride species.[49] They also proposed that this modification would lead to a lower overpotential compared to systems with bridging hydride species.[52,61–63] The exploration of electron transfer relays, which is the vital components in natural enzymes, was first attempted by Tard *et al.*, who incorporated a cubane $[Fe4S4]^-$ cluster and a $[2Fe3S]^-$ model via a sulfur ligand. Although this system functioned as an electrocatalyst for proton reduction, it had large overpotential and lacked the ability to perform the reverse process. Despite significant progress in developing [FeFe]-mimics, replicating the [4Fe–4S] cluster function has received limited attention.[64,65] In case of [NiFe] mimics, to date, only a few active synthetic catalysts have been reported, but the mononuclear $[Ni(P^R_2N^{R'}_2)_2]^{2+}$ complexes, developed by DuBois and co-workers, stand out as some of the most efficient bioinspired catalysts for hydrogen production.[18,66,67] These complexes are also the only known series capable of catalytic H_2 oxidation. The key to their high catalytic performance lies in the pendant amine groups incorporated into the diphosphine ligands of the Ni ion, which serve as crucial proton relays.

This design enables efficient H^+/H_2 interconversion at moderate overpotentials.[20] W. Shaw and co-workers have leveraged these complexes to explore the impact of enzyme-like functionalities such as amino acids, amino-ester derivatives, and peptides in the outer coordination sphere on catalytic rates **(Fig. 3A)**.[68–70] Complexes with acidic or basic side chains exhibited up to a fivefold increase in the rate of electrocatalytic H_2 evolution in water/acetonitrile mixtures compared to their unmodified counterparts **(Fig. 3B)**. Additionally, terminal propionic acid groups were employed to introduce a highly structured, sterically constrained β-hairpin 10-mer peptide into the related $[Ni(PPH_2N^{Ar})_2]^{2+}$ complex **(Fig. 3C)**.[71] However, the peptide system proved too flexible, complicating efforts to consistently study the relationship between catalytic activity and the nature of the protein-based second coordination sphere. Hence, these biomimetic systems inspired by the [FeFe] and [NiFe] catalytic cofactors found in hydrogenase active sites have struggled to match the remarkable efficiency of the natural enzymes.

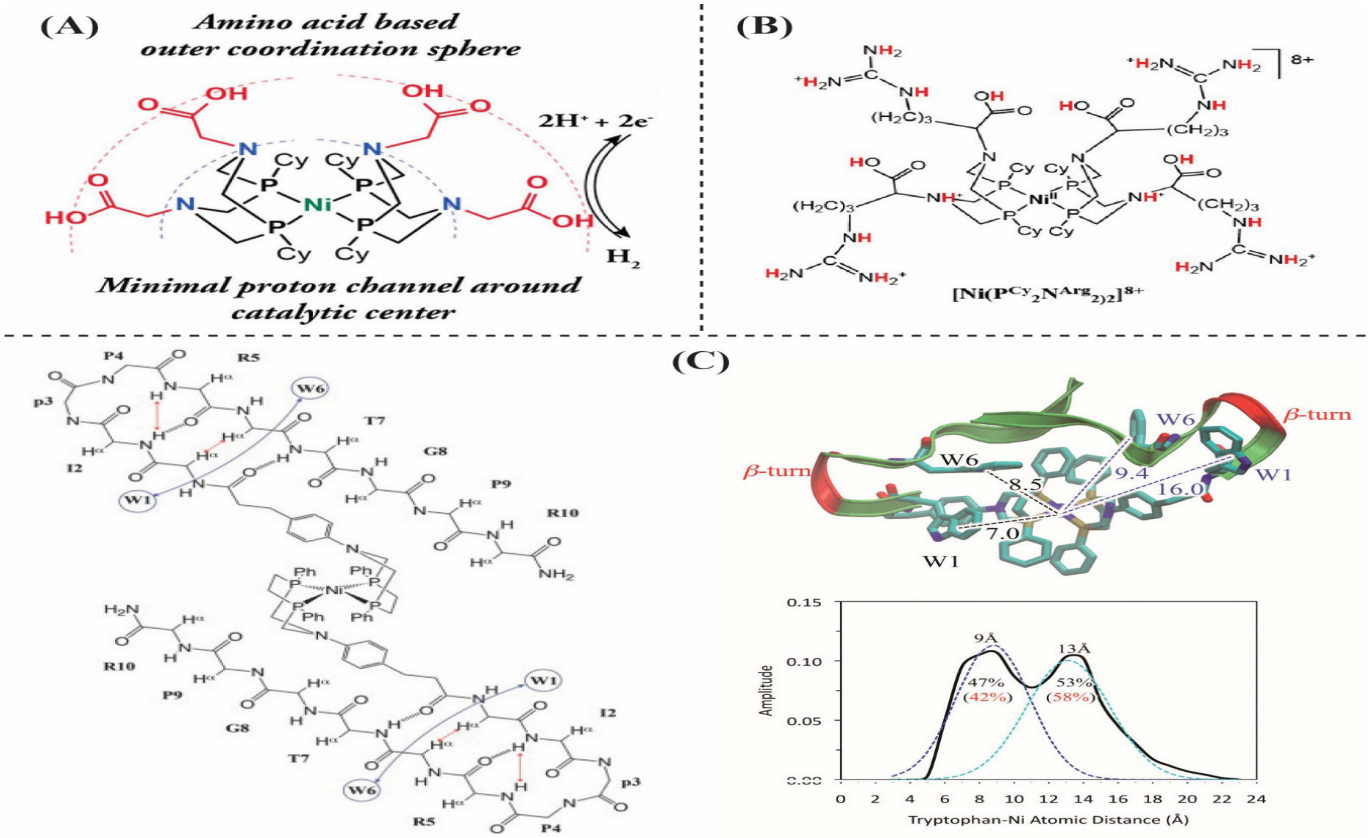

Figure 3: (A) The amine of glycine was incorporated directly into $[Ni^{II}(P^{Cy}_2N^{Gly}_2)_2]^{4+}$. The resulting complex was observed to transfer protons rapidly between the pendant amine and the COOH. This figure is taken from ref. [72], copyright ACS [2014] **(B)** $[Ni^{II}(P^{Cy}_2N^{Arg}_2)_2]^{8+}$ is an active H_2 oxidation catalyst at all pH values, with the fastest rates at low pH, conditions most relevant for fuel cells. Overpotentials also vary as

a function of pH, demonstrating a dependence on proton or electron transfer or both at high rates. This figure is taken from ref. [72], copyright ACS [2014] **(C)** $[Ni(^{PP}H_2N^{NNA-hairpin})_2]^{2+}$ complex is an active H_2 production catalyst. This figure is taken from ref. [69], copyright ACS [2014]

This distinct gap in reactivity between the enzymatic systems and these synthetic small molecule models can be attributed to two key factors: (i) the need for the synthetic models to operate in non-aqueous solvents, and (ii) the absence of a protein environment, which plays a crucial role in modulating catalytic activity through outer coordination sphere interactions.

Experimental aspects of testing Enzymes for hydrogen production:

To evaluate enzyme-catalyzed hydrogen production, cyclic voltammetry (CV), bulk electrochemistry, and gas chromatography (GC) are commonly employed. Initially, CV studies are performed in a typical three-electrode setup consisting of a working electrode, reference electrode, and counter electrode. The enzyme is immobilized on the working electrode surface within an electrochemical cell, and the potential is swept over a defined range to monitor its redox and catalytic behavior. This technique provides valuable insights into the enzyme's electrochemical activity, onset potential, overpotential, and overall efficiency in hydrogen production. The catalytic current observed during CV directly correlates with the enzyme's ability to produce hydrogen under specific conditions. To further evaluate hydrogen production, bulk electrochemistry is performed after CV. In this step, the enzyme-coated electrode is held at a constant potential for an extended period, enabling sustained hydrogen generation. Once hydrogen is produced electrochemically, GC is used for quantification. The headspace gas from the electrochemical cell is sampled and injected into the GC system, where the hydrogen is separated and detected, providing precise measurements. Together, these techniques offer a comprehensive analysis of the enzyme's hydrogen production capability.

Transition to Proteins and Peptides: Incorporating Artificial Molecular Catalysts into Proteins

The exceptional performance of metalloenzymes is largely due to the precise control over reactivity, which is achieved through a complex interaction between the metal at the active site, the surrounding metal-coordinating atoms or the outer coordination sphere (OCS) and the dynamic protein scaffold that both encapsulates and extends beyond the active site. Bioinorganic research has been keenly focused on unraveling the structure-function relationships essential for this controlled reactivity.[73–77] Recent studies have highlighted the protein scaffold as a highly versatile element, significantly influencing metalloenzyme chemistry.[78,79] Although the full extent of the protein scaffold's impact is not yet fully understood, it is believed to directly affect catalytic activity in several ways: (1) fostering favorable interactions between the scaffold and the metal or cofactor, (2) strategically positioning residues and excluding solvent to regulate the electrostatic environment, (3) embedding active sites within specific pockets to facilitate the entry of reactants while limiting solvent or inhibitor access, and (4) enabling or restricting conformational changes throughout the catalytic cycle.[80] Various synthetic strategies have been employed to replicate the influence of enzymatic scaffolds on catalytic activity within synthetic systems. One prominent approach is the reengineering of metal-binding proteins. Early work by Lombardi and Lu's groups

showcased successful examples of such protein reengineering.[77] Building on this, Shafaat and colleagues later redesigned rubredoxin, substituting Ni for Fe, thereby creating a simplified structural and functional model of [NiFe]-hydrogenase.[81] This engineered Ni-complex demonstrated significant electrocatalytic activity for H_2 production, unlike the Fe-complex, which did not exhibit such activity. The active site surrounding Ni effectively mimics the geometry of [NiFe]-hydrogenase. Further investigations utilizing molecular dynamics simulations, resonance Raman spectroscopy, and quantitative electrochemical analysis identified a plausible reaction mechanism, where thiol inversion followed by hydride formation constitutes the rate-limiting step. Modifying the second coordination sphere with two independent valine-to-histidine variants revealed distinct roles for this outer coordination sphere. The V8H construct exhibited nearly a four-fold increase in catalytic activity compared to the wild type (WT), whereas the V34H variant maintained similar activity levels.

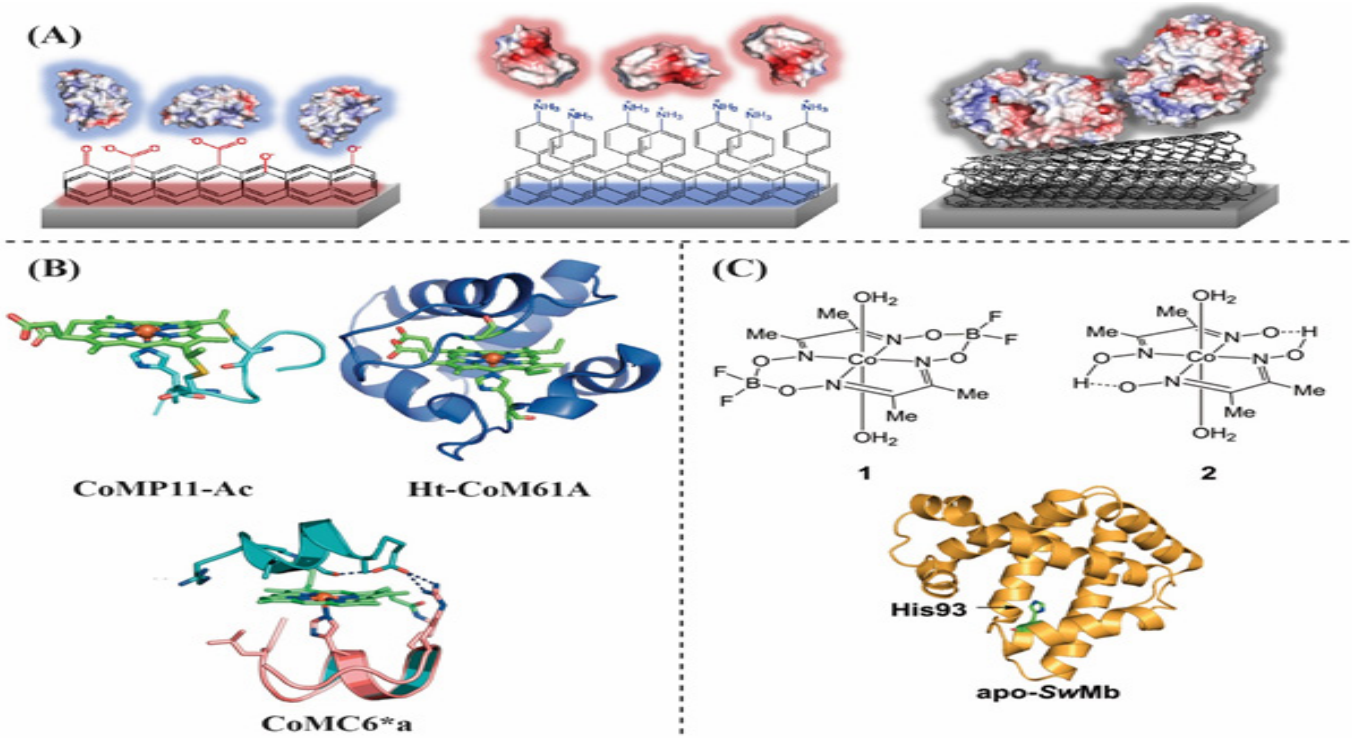

Figure 4: (A) Surface of unmodified graphitic electrodes is typically negatively charged, favoring electrostatic adsorption of positively charged proteins and molecules [left]. Aniline-functionalized surfaces are positively charged, favoring electrostatic adsorption of positively charged proteins and molecules [centre]. Nanotube-coated surfaces are hydrophobic, favoring adsorption of large, hydrophobic, or zwitterionic proteins and molecules [right]. This figure is taken from ref. [82], copyright ACS [2020] **(B)** Figures of cytochrome c-derived heme-peptide complex, microperoxidase-11 **CoMP11-Ac (PDB ID: 1CRC)**, a cobalt-substituted mutant of *Hydrogenobacter thermophilus* cytochrome c552 **Ht-CoM61A (PDB ID: 1AYG)**, a synthetic cobalt-heme mini-protein **CoMC6*a** (Model). This figure is taken from ref. [83], copyright ACS [2019] **(C)** Structures of the model of **apo-SwMb** (sperm-whale myoglobin) showing H93 of the binding pocket (PDB ID: IUFJ) This figure is taken from ref. [83], copyright ACS [2014].

Notably, the V8H mutant showed turnover frequencies (TOFs) that were independent of pH, in contrast to the V34H mutant, which was pH-dependent. These findings underscore the outer coordination sphere's sensitivity to subtle environmental changes.[84] Another crucial factor in improving the efficiency of these systems is achieving rapid interfacial electron transfer rates between the enzyme and electrode, which enables precise electrochemical control of redox-active enzymes immobilized on the electrode surface. Pioneering electrochemical studies by Armstrong and co-workers demonstrated that even minimal amounts of [NiFe] hydrogenase adsorbed on pyrolytic graphite electrodes could produce remarkably high catalytic currents, allowing for the measurement of catalytic and affinity constants.[29] More recently, Shafaat and co-workers have elaborated on various methodologies for the covalent attachment of nickel-substituted rubredoxin (NiRd) to unmodified graphite electrodes through amide bond formation **(Fig. 4A)**.[82] The resulting electrodes exhibited high activity for H_2 evolution over several weeks. This simple and effective approach has the potential to be widely applied to various redox-active proteins and enzymes, enhancing the stability of these systems over extended periods. However, challenges remain, such as reduced protein dynamics and limited oxygen tolerance in some cases, which continue to hinder their practical applications. To tackle this challenge, various cobalt complexes and their bio-hybrids have demonstrated promising potential for enhanced hydrogen production. Noteworthy contributions in this field have been made by Bren and team. One of the earliest and simplest catalysts developed is CoMP11-Ac **(Fig. 4B)**, a cobalt-porphyrin-based catalyst that operates in water and boasts a respectable turnover number (TON) of 25,000. This catalyst is synthesized by substituting cobalt for iron in the cytochrome c-derived heme-peptide complex, microperoxidase-11 (MP11), followed by acetylation of the free amines. CoMP11-Ac features cobalt protoporphyrin IX covalently linked to an 11-amino acid chain through a Cys-Xaa-Xaa-Cys-His motif, providing an axial histidine ligand on the porphyrin's proximal side. Unlike many porphyrin-based catalysts, CoMP11-Ac is functional in water. However, its short lifespan spurred the development of other biocatalysts with a similar cobalt porphyrin active site, but with polypeptides on both sides of the porphyrin. One such catalyst is Ht-CoM61A[85] **(Fig. 4B)**, a cobalt-substituted mutant of *Hydrogenobacter thermophilus* cytochrome c552, which is more robust, lasting approximately 5 hours and achieving a tenfold increase in TON to 270,000. Another notable cobalt-porphyrin-based catalyst is the synthetic cobalt-heme mini-protein CoMC6*a[86] **(Fig. 4B)**, which not only lowers overpotential but also enhances catalyst longevity, with a TON of 230,000. Another strategy for designing catalysts involves enhancing proton availability and delivery to the active site. One example of this approach is the addition of a bioinspired outer-coordination sphere to the widely studied Cobaloxime, which is known for its excellent oxygen tolerance and water solubility. Artero and co-workers developed two cobaloxime derivatives featuring difluoroboronyl (1) and proton-bridged (2) glyoxime ligands, which were incorporated into sperm-whale myoglobin, resulting in SwMb·1 and SwMb·2, respectively **(Fig. 4C)**.[87] These hybrids demonstrated activity in photocatalytic hydrogen production. Although their turnover numbers (TON) were modest (~5), this work successfully introduced synthetic catalysts into a protein scaffold, creating a water-compatible system with H_2-evolution activity. Later, Lisa M.

Utschig and her team incorporated cobaloxime into ferredoxin, which improved its TON (~85) while maintaining its activity only towards photocatalytic H_2 production capability.

Over the past five years, our group has been dedicated to enhancing the activity of cobaloximes through modifications with amino acids, neurotransmitters, vitamin B6, drug molecules, and nucleic bases. We observed that each modification, featuring an improved outer coordination sphere with strategically positioned basic functionalities, led to a significant increase in electrocatalytic hydrogen production. To further explore the untapped potential of this catalyst, we are currently exploring the possibility of incorporating the cobaloxime core into a robust protein scaffold (like azurin) to create a synthetic metalloprotein. Here we aim to harness the unique interplay between the transition metal active site and the protein-based OCS. Azurin (Az) exemplifies a sophisticated synergy between the Cu-based active site and the adaptable protein-based outer coordination sphere (OCS), while it remains resilient to mutation in the protein scaffold. Hence, Az provides a perfect tuneable platform, providing a well-defined secondary coordination sphere to host variable metal cofactors and investigate the resulting catalytic efficiency and selectivity. Additionally, this durable constructs can be integrated into operational electrolyzers for generating hydrogen from neutral water, further underscoring its applicability in diverse real-world scenarios.

Current Challenges and Future Perspectives

While the field of hydrogen production using enzymes, proteins, and peptides has made remarkable strides, several significant challenges remain that must be addressed to realize the full potential of these bio-inspired systems in practical applications. While hydrogenase enzymes are highly efficient in their natural contexts, replicating this efficiency in synthetic or biohybrid systems remains difficult. Synthetic mimics often struggle to achieve the same turnover numbers and overpotentials as their natural counterparts. Additionally, integrating enzymes or synthetic mimics into practical devices like electrolyzers or fuel cells poses its own set of challenges. The delicate nature of these catalysts requires careful control of the operational environment to maintain their activity and stability. Moreover, the need for efficient electron transfer between the catalyst and the electrode materials adds another layer of complexity. Achieving the optimal interface between the biological or biohybrid catalyst and the inorganic components of a device is crucial for maximizing performance but remains a significant engineering challenge. Hence, an ideal enzyme should be robust, exhibit thermal stability and resistance to harsh conditions, such as varying pH levels and high temperatures, which are common in industrial processes.

Advances in protein engineering and synthetic biology offer exciting possibilities for enhancing the oxygen tolerance and stability of hydrogenase enzymes. By introducing mutations that protect the active site from oxygen damage or by encapsulating the enzyme in protective matrices, it may be possible to extend the utility of these catalysts to a wider range of environments. Also, the integration of synthetic catalysts into protein frameworks represents a promising strategy to combine the best attributes of both natural and synthetic systems. These bio-hybrid systems could leverage the structural complexity and specificity of proteins while benefiting from the robustness and scalability of synthetic catalysts. Furthermore, the development of multi-component catalytic systems, where different components work

synergistically to enhance overall performance, could lead to breakthroughs in both efficiency and stability. Moreover, scaling up these systems from laboratory experiments to industrial-scale applications will require close collaboration between researchers in catalysis, materials science, and chemical engineering. Demonstrating the viability of these systems in real-world applications, such as in electrolyzers that operate on seawater or other challenging environments, will be a key step toward their broader adoption.

Conclusion

The quest to harness the efficiency of hydrogenase enzymes for practical hydrogen production has driven significant advancements in both biological and synthetic catalysis. Despite their unmatched catalytic prowess, the challenges of oxygen sensitivity, stability, and scalability have limited the direct application of hydrogenases in industrial settings. This mini-review has highlighted the journey from natural enzymes to innovative biohybrid and synthetic systems that seek to replicate and surpass the performance of hydrogenase catalysts. Efforts to engineer stable catalysts, exploring alternative metal centers, and developing biohybrid systems have shown promise in addressing these challenges. Moreover, the integration of these catalysts into practical devices, such as electrolyzers, operational in seawater are the tools to guide catalyst design as critical steps forward. As the field progresses, the development of robust, efficient, and scalable hydrogen production technologies will be essential for the transition to a sustainable hydrogen economy. The future of hydrogen production lies in the successful combination of nature's design principles with human innovation, leading to systems that not only match but exceed the capabilities of their natural counterparts. Continued research and interdisciplinary collaboration will be key to overcoming the remaining obstacles and realizing the full potential of these bio-inspired approaches in the energy landscape of the future.

Conflicts of interest

The authors declare no conflicts of interest.

Acknowledgment

The authors would like to thank Indian Institute of Technology Bombay (IITB) and DST, India-supported National Centre of Excellence (DST/TMD/CCUS/CoE/202/IITB), for this research activity.

References

(1) Bullock, R. M.; Dey, A. Introduction: Catalysis beyond the First Coordination Sphere. *Chem. Rev.* **2022**, *122* (14), 11897–11899. https://doi.org/10.1021/acs.chemrev.2c00428.

(2) Lewis, N. S.; Nocera, D. G. Powering the Planet: Chemical Challenges in Solar Energy Utilization. *Proceedings of the National Academy of Sciences* **2006**, *103* (43), 15729–15735. https://doi.org/10.1073/pnas.0603395103.

(3) Awasthi, M. K.; Saini, A.; Das, C.; Banerjee, A.; Shah, N. A.; Lahiri, G. K.; Dutta, A. Bio-Inspired Design of Bidirectional Oxygen Reduction and Oxygen Evolution Reaction Molecular Electrocatalysts. *European Journal of Inorganic Chemistry n/a* (n/a), e202300204. https://doi.org/10.1002/ejic.202300204.

(4) Nocera, D. G. Solar Fuels and Solar Chemicals Industry. *Acc. Chem. Res.* **2017**, *50* (3), 616–619. https://doi.org/10.1021/acs.accounts.6b00615.

(5) Armstrong, F. A.; Evans, R. M.; Hexter, S. V.; Murphy, B. J.; Roessler, M. M.; Wulff, P. Guiding Principles of Hydrogenase Catalysis Instigated and Clarified by Protein Film Electrochemistry. *Acc. Chem. Res.* **2016**, *49* (5), 884–892. https://doi.org/10.1021/acs.accounts.6b00027.

(6) Lubitz, W.; Ogata, H.; Rüdiger, O.; Reijerse, E. Hydrogenases. *Chem. Rev.* **2014**, *114* (8), 4081–4148. https://doi.org/10.1021/cr4005814.

(7) Rasmussen, M.; Abdellaoui, S.; Minteer, S. D. Enzymatic Biofuel Cells: 30 Years of Critical Advancements. *Biosensors and Bioelectronics* **2016**, *76*, 91–102. https://doi.org/10.1016/j.bios.2015.06.029.

(8) Reisner, E. Solar Hydrogen Evolution with Hydrogenases: From Natural to Hybrid Systems. *European Journal of Inorganic Chemistry* **2011**, *2011* (7), 1005–1016. https://doi.org/10.1002/ejic.201000986.

(9) Turner, J. A. Sustainable Hydrogen Production. *Science* **2004**, *305* (5686), 972–974. https://doi.org/10.1126/science.1103197.

(10) Brooke, E. J.; Evans, R. M.; Islam, S. T. A.; Roberts, G. M.; Wehlin, S. A. M.; Carr, S. B.; Phillips, S. E. V.; Armstrong, F. A. Importance of the Active Site "Canopy" Residues in an O2-Tolerant [NiFe]-Hydrogenase. *Biochemistry* **2017**, *56* (1), 132–142. https://doi.org/10.1021/acs.biochem.6b00868.

(11) Petrik, I. D.; Liu, J.; Lu, Y. Metalloenzyme Design and Engineering through Strategic Modifications of Native Protein Scaffolds. *Current Opinion in Chemical Biology* **2014**, *19*, 67–75. https://doi.org/10.1016/j.cbpa.2014.01.006.

(12) Fourmond, V.; Wiedner, E. S.; Shaw, W. J.; Léger, C. Understanding and Design of Bidirectional and Reversible Catalysts of Multielectron, Multistep Reactions. *J. Am. Chem. Soc.* **2019**, *141* (28), 11269–11285. https://doi.org/10.1021/jacs.9b04854.

(13) Ward, T. R. Artificial Metalloenzymes Based on the Biotin−Avidin Technology: Enantioselective Catalysis and Beyond. *Acc. Chem. Res.* **2011**, *44* (1), 47–57. https://doi.org/10.1021/ar100099u.

(14) Dutta, A.; Appel, A. M.; Shaw, W. J. Designing Electrochemically Reversible H2 Oxidation and Production Catalysts. *Nat Rev Chem* **2018**, *2* (9), 244–252. https://doi.org/10.1038/s41570-018-0032-8.

(15) Jae Jeong, W.; Yu, J.; Ju Song, W. Proteins as Diverse, Efficient, and Evolvable Scaffolds for Artificial Metalloenzymes. *Chemical Communications* **2020**, *56* (67), 9586–9599. https://doi.org/10.1039/D0CC03137B.

(16) Armstrong, F. A.; Hirst, J. Reversibility and Efficiency in Electrocatalytic Energy Conversion and Lessons from Enzymes. *Proceedings of the National Academy of Sciences* **2011**, *108* (34), 14049–14054. https://doi.org/10.1073/pnas.1103697108.

(17) Caserta, G.; Roy, S.; Atta, M.; Artero, V.; Fontecave, M. Artificial Hydrogenases: Biohybrid and Supramolecular Systems for Catalytic Hydrogen Production or Uptake. *Current Opinion in Chemical Biology* **2015**, *25*, 36–47. https://doi.org/10.1016/j.cbpa.2014.12.018.

(18) Simmons, T. R.; Berggren, G.; Bacchi, M.; Fontecave, M.; Artero, V. Mimicking Hydrogenases: From Biomimetics to Artificial Enzymes. *Coordination Chemistry Reviews* **2014**, *270–271*, 127–150. https://doi.org/10.1016/j.ccr.2013.12.018.

(19) Artero, V.; Fontecave, M. Some General Principles for Designing Electrocatalysts with Hydrogenase Activity. *Coordination Chemistry Reviews* **2005**, *249* (15), 1518–1535. https://doi.

org/10.1016/j.ccr.2005.01.014.

(20) Jain, A.; Lense, S.; Linehan, J. C.; Raugei, S.; Cho, H.; DuBois, D. L.; Shaw, W. J. Incorporating Peptides in the Outer-Coordination Sphere of Bioinspired Electrocatalysts for Hydrogen Production. *Inorg. Chem.* **2011**, *50* (9), 4073–4085. https://doi.org/10.1021/ic1025872.

(21) Ogata, H.; Hirota, S.; Nakahara, A.; Komori, H.; Shibata, N.; Kato, T.; Kano, K.; Higuchi, Y. Activation Process of [NiFe] Hydrogenase Elucidated by High-Resolution X-Ray Analyses: Conversion of the Ready to the Unready State. *Structure* **2005**, *13* (11), 1635–1642. https://doi.org/10.1016/j.str.2005.07.018.

(22) Nicolet, Y.; Piras, C.; Legrand, P.; Hatchikian, C. E.; Fontecilla-Camps, J. C. Desulfovibrio Desulfuricans Iron Hydrogenase: The Structure Shows Unusual Coordination to an Active Site Fe Binuclear Center. *Structure* **1999**, *7* (1), 13–23. https://doi.org/10.1016/S0969-2126(99)80005-7.

(23) Thauer, R. K. Hydrogenases and the Global H2 Cycle. *European Journal of Inorganic Chemistry* **2011**, *2011* (7), 919–921. https://doi.org/10.1002/ejic.201001255.

(24) Vincent, K. A.; Parkin, A.; Armstrong, F. A. Investigating and Exploiting the Electrocatalytic Properties of Hydrogenases. *Chem. Rev.* **2007**, *107* (10), 4366–4413. https://doi.org/10.1021/cr050191u.

(25) Thauer, R. K.; Klein, A. R.; Hartmann, G. C. Reactions with Molecular Hydrogen in Microorganisms: Evidence for a Purely Organic Hydrogenation Catalyst. *Chem. Rev.* **1996**, *96* (7), 3031–3042. https://doi.org/10.1021/cr9500601.

(26) Fontecilla-Camps, J. C.; Volbeda, A.; Cavazza, C.; Nicolet, Y. Structure/Function Relationships of [NiFe]- and [FeFe]-Hydrogenases. *Chem. Rev.* **2007**, *107* (10), 4273–4303. https://doi.org/10.1021/cr050195z.

(27) Vignais, P. M.; Billoud, B. Occurrence, Classification, and Biological Function of Hydrogenases: An Overview. *Chem. Rev.* **2007**, *107* (10), 4206–4272. https://doi.org/10.1021/cr050196r.

(28) Jones, A. K.; Sillery, E.; Albracht, S. P. J.; Armstrong, F. A. Direct Comparison of the Electrocatalytic Oxidation of Hydrogen by an Enzyme and a Platinum Catalyst. *Chem. Commun.* **2002**, No. 8, 866–867. https://doi.org/10.1039/B201337A.

(29) Pershad, H. R.; Duff, J. L. C.; Heering, H. A.; Duin, E. C.; Albracht, S. P. J.; Armstrong, F. A. Catalytic Electron Transport in Chromatium Vinosum [NiFe]-Hydrogenase: Application of Voltammetry in Detecting Redox-Active Centers and Establishing That Hydrogen Oxidation Is Very Fast Even at Potentials Close to the Reversible H+/H2 Value. *Biochemistry* **1999**, *38* (28), 8992–8999. https://doi.org/10.1021/bi990108v.

(30) Madden, C.; Vaughn, M. D.; Díez-Pérez, I.; Brown, K. A.; King, P. W.; Gust, D.; Moore, A. L.; Moore, T. A. Catalytic Turnover of [FeFe]-Hydrogenase Based on Single-Molecule Imaging. *J. Am. Chem. Soc.* **2012**, *134* (3), 1577–1582. https://doi.org/10.1021/ja207461t.

(31) Schleucher, J.; Griesinger, C.; Schwoerer, B.; Thauer, R. K. H2-Forming N5,N10-Methylenetetrahydromethanopterin Dehydrogenase from Methanobacterium Thermoautotrophicum Catalyzes a Stereoselective Hydride Transfer As Determined by Two-Dimensional NMR Spectroscopy. *Biochemistry* **1994**, *33* (13), 3986–

3993. https://doi.org/10.1021/bi00179a027.

(32) Dance, I. Structural Variability of the Active Site of Fe-Only Hydrogenase and Its Hydrogenated Forms. *Chemical Communications* **1999**, *0* (17), 1655–1656. https://doi.org/10.1039/A903803E.

(33) Roseboom, W.; De Lacey, A. L.; Fernandez, V. M.; Hatchikian, E. C.; Albracht, S. P. J. The Active Site of the [FeFe]-Hydrogenase from Desulfovibrio Desulfuricans. II. Redox Properties, Light Sensitivity and CO-Ligand Exchange as Observed by Infrared Spectroscopy. *J Biol Inorg Chem* **2006**, *11* (1), 102–118. https://doi.org/10.1007/s00775-005-0040-2.

(34) Yan, L.; Dapper, C. H.; George, S. J.; Wang, H.; Mitra, D.; Dong, W.; Newton, W. E.; Cramer, S. P. Photolysis of Hi-CO Nitrogenase – Observation of a Plethora of Distinct CO Species Using Infrared Spectroscopy. *European Journal of Inorganic Chemistry* **2011**, *2011* (13), 2064–2074. https://doi.org/10.1002/ejic.201100029.

(35) Siegbahn, P. E. M.; Tye, J. W.; Hall, M. B. Computational Studies of [NiFe] and [FeFe] Hydrogenases. *Chem. Rev.* **2007**, *107* (10), 4414–4435. https://doi.org/10.1021/cr050185y.

(36) de Lacey, A. L.; Hatchikian, E. C.; Volbeda, A.; Frey, M.; Fontecilla-Camps, J. C.; Fernandez, V. M. Infrared-Spectroelectrochemical Characterization of the [NiFe] Hydrogenase of Desulfovibrio Gigas. *J. Am. Chem. Soc.* **1997**, *119* (31), 7181–7189. https://doi.org/10.1021/ja963802w.

(37) Zhou, T.; Mo, Y.; Liu, A.; Zhou, Z.; Tsai, K. R. Enzymatic Mechanism of Fe-Only Hydrogenase: Density Functional Study on H−H Making/Breaking at the Diiron Cluster with Concerted Proton and Electron Transfers. *Inorg. Chem.* **2004**, *43* (3), 923–930. https://doi.org/10.1021/ic0342301.

(38) Volbeda, A.; Charon, M.-H.; Piras, C.; Hatchikian, E. C.; Frey, M.; Fontecilla-Camps, J. C. Crystal Structure of the Nickel–Iron Hydrogenase from Desulfovibrio Gigas. *Nature* **1995**, *373* (6515), 580–587. https://doi.org/10.1038/373580a0.

(39) Tsay, C.; Peters, J. C. Thermally Stable N2 and H_2 Adducts of Cationic Nickel(II). *Chem. Sci.* **2012**, *3* (4), 1313–1318. https://doi.org/10.1039/C2SC01033J.

(40) Volbeda, A.; Fontecilla-Camps, J. C. Catalytic Nickel–Iron–Sulfur Clusters: From Minerals to Enzymes. In *Bioorganometallic Chemistry*; Simonneaux, G., Ed.; Springer: Berlin, Heidelberg, 2006; pp 57–82. https://doi.org/10.1007/3418_003.

(41) Shafaat, H. S.; Rüdiger, O.; Ogata, H.; Lubitz, W. [NiFe] Hydrogenases: A Common Active Site for Hydrogen Metabolism under Diverse Conditions. *Biochimica et Biophysica Acta (BBA) - Bioenergetics* **2013**, *1827* (8), 986–1002. https://doi.org/10.1016/j.bbabio.2013.01.015.

(42) Stripp, S. T.; Goldet, G.; Brandmayr, C.; Sanganas, O.; Vincent, K. A.; Haumann, M.; Armstrong, F. A.; Happe, T. How Oxygen Attacks [FeFe] Hydrogenases from Photosynthetic Organisms. *Proceedings of the National Academy of Sciences* **2009**, *106* (41), 17331–17336. https://doi.org/10.1073/pnas.0905343106.

(43) Liebgott, P.-P.; de Lacey, A. L.; Burlat, B.; Cournac, L.; Richaud, P.; Brugna, M.; Fernandez, V. M.; Guigliarelli, B.; Rousset, M.; Léger, C.; Dementin, S. Original Design of an Oxygen-Tolerant [NiFe] Hydrogenase: Major Effect of a Valine-to-Cysteine Mutation near the Active Site. *J. Am. Chem. Soc.* **2011**, *133* (4), 986–997. https://doi.org/10.1021/ja108787s.

(44) Fritsch, J.; Scheerer, P.; Frielingsdorf, S.;

Kroschinsky, S.; Friedrich, B.; Lenz, O.; Spahn, C. M. T. The Crystal Structure of an Oxygen-Tolerant Hydrogenase Uncovers a Novel Iron-Sulphur Centre. *Nature* **2011**, *479* (7372), 249–252. https://doi.org/10.1038/nature10505.

(45) Grubel, K.; Holland, P. L. New Iron-Sulfur Clusters Help Hydrogenases Tolerate Oxygen. *Angew Chem Int Ed Engl* **2012**, *51* (14), 3308–3310. https://doi.org/10.1002/anie.201108761.

(46) Tard, C.; Pickett, C. J. Structural and Functional Analogues of the Active Sites of the [Fe]-, [NiFe]-, and [FeFe]-Hydrogenases. *Chem. Rev.* **2009**, *109* (6), 2245–2274. https://doi.org/10.1021/cr800542q.

(47) Khrizanforova, V. V.; Karasik, A. A.; Budnikova, Y. H. Synthetic Organometallic Models of Iron-Containing Hydrogenases as Molecular Electrocatalysts for Hydrogen Evolution or Oxidation. *Russ. Chem. Rev.* **2017**, *86* (4), 298. https://doi.org/10.1070/RCR4676.

(48) Galinato, M. G. I.; Whaley, C. M.; Lehnert, N. Vibrational Analysis of the Model Complex (μ-Edt)[Fe(CO)3]2 and Comparison to Iron-Only Hydrogenase: The Activation Scale of Hydrogenase Model Systems. *Inorg Chem* **2010**, *49* (7), 3201–3215. https://doi.org/10.1021/ic9022135.

(49) Barton, B. E.; Rauchfuss, T. B. Terminal Hydride in [FeFe]-Hydrogenase Model Has Lower Potential for H2 Production Than the Isomeric Bridging Hydride. *Inorg. Chem.* **2008**, *47* (7), 2261–2263. https://doi.org/10.1021/ic800030y.

(50) Justice, A. K.; Nilges, M. J.; Rauchfuss, T. B.; Wilson, S. R.; De Gioia, L.; Zampella, G. Diiron Dithiolato Carbonyls Related to the H(Ox) CO State of [FeFe]-Hydrogenase. *J Am Chem Soc* **2008**, *130* (15), 5293–5301. https://doi.org/10.1021/ja7113008.

(51) Darensbourg, M. Y.; Lyon, E. J.; Zhao, X.; Georgakaki, I. P. The Organometallic Active Site of [Fe]Hydrogenase: Models and Entatic States. *Proceedings of the National Academy of Sciences* **2003**, *100* (7), 3683–3688. https://doi.org/10.1073/pnas.0536955100.

(52) Harb, M. K.; Niksch, T.; Windhager, J.; Görls, H.; Holze, R.; Lockett, L. T.; Okumura, N.; Evans, D. H.; Glass, R. S.; Lichtenberger, D. L.; El-khateeb, M.; Weigand, W. Synthesis and Characterization of Diiron Diselenolato Complexes Including Iron Hydrogenase Models. *Organometallics* **2009**, *28* (4), 1039–1048. https://doi.org/10.1021/om800748p.

(53) Song, L.-C.; Li, Q.-L.; Feng, Z.-H.; Sun, X.-J.; Xie, Z.-J.; Song, H.-B. Synthesis, Characterization, and Electrochemical Properties of Diiron Propaneditellurolate (PDTe) Complexes as Active Site Models of [FeFe]-Hydrogenases. *Dalton Trans.* **2013**, *42* (5), 1612–1626. https://doi.org/10.1039/C2DT31976D.

(54) Aguado, S.; Vicent, D. J.; Casarrubios, L.; Ramírez de Arellano, C.; Sierra, M. A. Two Complementary Approaches to Silicon-Supported Soluble [FeFe]-Hydrogenase Mimics. *Organometallics* **2022**, *41* (22), 3281–3292. https://doi.org/10.1021/acs.organomet.2c00277.

(55) Watanabe, M.; Honda, Y.; Hagiwara, H.; Ishihara, T. [FeFe]-Hydrogenase and Its Organic Molecule Mimics—Artificial and Bioengineering Application for Hydrogenproduction. *Journal of Photochemistry and Photobiology C: Photochemistry Reviews* **2017**, *33*, 1–26. https://doi.org/10.1016/j.jphotochemrev.2017.09.001.

(56) Escudero, D. A Silicon-Heteroaromatic System as Photosensitizer for Light-Driven Hydrogen Production by Hydrogenase Mimics. *European Journal of Inorganic Chemistry* **2013**.

(57) Gao, S.; Fan, J.; Sun, S.; Peng, X.; Zhao, X.; Hou, J. Selenium-Bridged Diiron Hexacarbonyl Complexes as Biomimetic Models for the Active Site of Fe–Fe Hydrogenases. *Dalton Trans.* **2008**, No. 16, 2128–2135. https://doi.org/10.1039/B717497G.

(58) Harb, M. K.; Görls, H.; Sakamoto, T.; Felton, G. A. N.; Evans, D. H.; Glass, R. S.; Lichtenberger, D. L.; El-khateeb, M.; Weigand, W. Synthesis and Characterization of [FeFe]-Hydrogenase Models with Bridging Moieties Containing (S, Se) and (S, Te). *European Journal of Inorganic Chemistry* **2010**, *2010* (25), 3976–3985. https://doi.org/10.1002/ejic.201000278.

(59) Song, L.-C.; Yang, Z.-Y.; Bian, H.-Z.; Liu, Y.; Wang, H.-T.; Liu, X.-F.; Hu, Q.-M. Diiron Oxadithiolate Type Models for the Active Site of Iron-Only Hydrogenases and Biomimetic Hydrogen Evolution Catalyzed by Fe2(μ-SCH2OCH2S-μ)(CO)6. *Organometallics* **2005**, *24* (25), 6126–6135. https://doi.org/10.1021/om0507373.

(60) Zhao, X.; Georgakaki, I. P.; Miller, M. L.; Mejia-Rodriguez, R.; Chiang, C.-Y.; Darensbourg, M. Y. Catalysis of H2/D2 Scrambling and Other H/D Exchange Processes by [Fe]-Hydrogenase Model Complexes. *Inorg. Chem.* **2002**, *41* (15), 3917–3928. https://doi.org/10.1021/ic020237r.

(61) Niu, S.; Nelson, A. E.; De La Torre, P.; Li, H.; Works, C. F.; Hall, M. B. Photoinduced Terminal Hydride of [FeFe]-Hydrogenase Biomimetic Complexes. *Inorg. Chem.* **2019**, *58* (20), 13737–13741. https://doi.org/10.1021/acs.inorgchem.9b01738.

(62) Liu, Y.-C.; Chu, K.-T.; Jhang, R.-L.; Lee, G.-H.; Chiang, M.-H. [FeFe] Hydrogenase Active Site Modeling: A Key Intermediate Bearing a Thiolate Proton and Fe Hydride. *Chemical Communications* **2013**, *49* (42), 4743–4745. https://doi.org/10.1039/C3CC39008J.

(63) Ezzaher, S.; Gogoll, A.; Bruhn, C.; Ott, S. Directing Protonation in [FeFe] Hydrogenase Active Site Models by Modifications in Their Second Coordination Sphere. *Chemical Communications* **2010**, *46* (31), 5775–5777. https://doi.org/10.1039/C0CC00724B.

(64) Zeng, X.; Li, Z.; Xiao, Z.; Wang, Y.; Liu, X. Using Pendant Ferrocenyl Group(s) as an Intramolecular Standard to Probe the Reduction of Diiron Hexacarbonyl Model Complexes for the Sub-Unit of [FeFe]-Hydrogenase. *Electrochemistry Communications* **2010**, *12* (3), 342–345. https://doi.org/10.1016/j.elecom.2009.12.023.

(65) Tard, C.; Liu, X.; Ibrahim, S. K.; Bruschi, M.; Gioia, L. D.; Davies, S. C.; Yang, X.; Wang, L.-S.; Sawers, G.; Pickett, C. J. Synthesis of the H-Cluster Framework of Iron-Only Hydrogenase. *Nature* **2005**, *433* (7026), 610–613. https://doi.org/10.1038/nature03298.

(66) Simmons, T. R.; Artero, V. Catalytic Hydrogen Oxidation: Dawn of a New Iron Age. *Angewandte Chemie International Edition* **2013**, *52* (24), 6143–6145. https://doi.org/10.1002/anie.201302908.

(67) DuBois, D. L. Development of Molecular Electrocatalysts for Energy Storage. *Inorg. Chem.* **2014**, *53* (8), 3935–3960. https://doi.org/10.1021/ic4026969.

(68) van der Vlugt, J. I.; Rauchfuss, T. B.; Wilson, S. R. Electron-Rich Diferrous–Phosphane–Thiolates Relevant to Fe-Only Hydrogenase: Is Cyanide "Nature's Trimethylphosphane"? *Chemistry – A European Journal* **2006**, *12* (1), 90–98. https://doi.org/10.1002/chem.200500752.

(69) Reback, M. L.; Buchko, G. W.; Kier, B. L.; Ginovska-Pangovska, B.; Xiong, Y.; Lense, S.; Hou, J.; Roberts, J. A. S.; Sorensen, C. M.; Raugei, S.;

Squier, T. C.; Shaw, W. J. Enzyme Design from the Bottom Up: An Active Nickel Electrocatalyst with a Structured Peptide Outer Coordination Sphere. *Chemistry – A European Journal* **2014**, *20* (6), 1510–1514. https://doi.org/10.1002/chem.201303976.

(70) Ginovska-Pangovska, B.; Dutta, A.; Reback, M. L.; Linehan, J. C.; Shaw, W. J. Beyond the Active Site: The Impact of the Outer Coordination Sphere on Electrocatalysts for Hydrogen Production and Oxidation. *Acc. Chem. Res.* **2014**, *47* (8), 2621–2630. https://doi.org/10.1021/ar5001742.

(71) Reback, M. L.; Ginovska, B.; Buchko, G. W.; Dutta, A.; Priyadarshani, N.; Kier, B. L.; Helm, M. L.; Raugei, S.; Shaw, W. J. Investigating the Role of Chain and Linker Length on the Catalytic Activity of an H2 Production Catalyst Containing a β-Hairpin Peptide. *Journal of Coordination Chemistry* **2016**, *69* (11–13), 1730–1747. https://doi.org/10.1080/00958972.2016.1188924.

(72) Ginovska-Pangovska, B.; Dutta, A.; Reback, M. L.; Linehan, J. C.; Shaw, W. J. Beyond the Active Site: The Impact of the Outer Coordination Sphere on Electrocatalysts for Hydrogen Production and Oxidation. *Acc. Chem. Res.* **2014**, *47* (8), 2621–2630. https://doi.org/10.1021/ar5001742.

(73) Ross, M. R.; White, A. M.; Yu, F.; King, J. T.; Pecoraro, V. L.; Kubarych, K. J. Histidine Orientation Modulates the Structure and Dynamics of a de Novo Metalloenzyme Active Site. *J. Am. Chem. Soc.* **2015**, *137* (32), 10164–10176. https://doi.org/10.1021/jacs.5b02840.

(74) Dawson, J. H. Probing Structure-Function Relations in Heme-Containing Oxygenases and Peroxidases. *Science* **1988**, *240* (4851), 433–439. https://doi.org/10.1126/science.3358128.

(75) Low, D. W.; Hill, M. G. Rational Fine-Tuning of the Redox Potentials in Chemically Synthesized Rubredoxins. *J. Am. Chem. Soc.* **1998**, *120* (44), 11536–11537. https://doi.org/10.1021/ja982920b.

(76) Warshel, A.; Sharma, P. K.; Kato, M.; Xiang, Y.; Liu, H.; Olsson, M. H. M. Electrostatic Basis for Enzyme Catalysis. *Chem. Rev.* **2006**, *106* (8), 3210–3235. https://doi.org/10.1021/cr0503106.

(77) Hosseinzadeh, P.; Marshall, N. M.; Chacón, K. N.; Yu, Y.; Nilges, M. J.; New, S. Y.; Tashkov, S. A.; Blackburn, N. J.; Lu, Y. Design of a Single Protein That Spans the Entire 2-V Range of Physiological Redox Potentials. *Proceedings of the National Academy of Sciences* **2016**, *113* (2), 262–267. https://doi.org/10.1073/pnas.1515897112.

(78) Wraight, C. A. Chance and Design—Proton Transfer in Water, Channels and Bioenergetic Proteins. *Biochimica et Biophysica Acta (BBA) - Bioenergetics* **2006**, *1757* (8), 886–912. https://doi.org/10.1016/j.bbabio.2006.06.017.

(79) Cui, Q.; Karplus, M. Is a "Proton Wire" Concerted or Stepwise? A Model Study of Proton Transfer in Carbonic Anhydrase. *J. Phys. Chem. B* **2003**, *107* (4), 1071–1078. https://doi.org/10.1021/jp021931v.

(80) A. Laureanti, J.; O'Hagan, M.; J. Shaw, W. Chicken Fat for Catalysis: A Scaffold Is as Important for Molecular Complexes for Energy Transformations as It Is for Enzymes in Catalytic Function. *Sustainable Energy & Fuels* **2019**, *3* (12), 3260–3278. https://doi.org/10.1039/C9SE00229D.

(81) Slater, J. W.; Shafaat, H. S. Nickel-Substituted Rubredoxin as a Minimal Enzyme Model for Hydrogenase. *J. Phys. Chem. Lett.* **2015**, *6* (18), 3731–3736. https://doi.org/10.1021/acs.jpclett.5b01750.

(82) Treviño, R. E.; Slater, J. W.; Shafaat, H. S. Robust Carbon-Based Electrodes for Hydrogen Evolution through Site-Selective Covalent Attachment of an Artificial Metalloenzyme. *ACS Appl. Energy Mater.* **2020**, *3* (11), 11099–11112. https://doi.org/10.1021/acsaem.0c02069.

(83) Le, J. M.; Bren, K. L. Engineered Enzymes and Bioinspired Catalysts for Energy Conversion. *ACS Energy Lett.* **2019**, *4* (9), 2168–2180. https://doi.org/10.1021/acsenergylett.9b01308.

(84) Slater, J. W.; Marguet, S. C.; Cirino, S. L.; Maugeri, P. T.; Shafaat, H. S. Experimental and DFT Investigations Reveal the Influence of the Outer Coordination Sphere on the Vibrational Spectra of Nickel-Substituted Rubredoxin, a Model Hydrogenase Enzyme. *Inorg. Chem.* **2017**, *56* (7), 3926–3938. https://doi.org/10.1021/acs.inorgchem.6b02934.

(85) Kandemir, B.; Chakraborty, S.; Guo, Y.; Bren, K. L. Semisynthetic and Biomolecular Hydrogen Evolution Catalysts. *Inorg. Chem.* **2016**, *55* (2), 467–477. https://doi.org/10.1021/acs.inorgchem.5b02054.

(86) Firpo, V.; M. Le, J.; Pavone, V.; Lombardi, A.; L. Bren, K. Hydrogen Evolution from Water Catalyzed by Cobalt-Mimochrome VI*a, a Synthetic Mini-Protein. *Chemical Science* **2018**, *9* (45), 8582–8589. https://doi.org/10.1039/C8SC01948G.

(87) Bacchi, M.; Berggren, G.; Niklas, J.; Veinberg, E.; Mara, M. W.; Shelby, M. L.; Poluektov, O. G.; Chen, L. X.; Tiede, D. M.; Cavazza, C.; Field, M. J.; Fontecave, M.; Artero, V. Cobaloxime-Based Artificial Hydrogenases. *Inorg. Chem.* **2014**, *53* (15), 8071–8082. https://doi.org/10.1021/ic501014c.

Bioimpedance-based investigation of anti-oxidant nanotherapeutics against intracellular oxidative stress

Gaurav Pandey[1,2,] Murugan Veerapandian[1,2]*

[1]*Electrodics and Electrocatalysis Division, CSIR-Central Electrochemical Research Institute, Karaikudi 630 003, Tamil Nadu*

[2]*Academy of Scientific & Innovative Research (AcSIR), Ghaziabad 201 002, India*

**Corresponding Author: vmurugan@cecri.res.in*

Abstract:

This study presents a non-invasive bioimpedance-based investigation using an electric cell-substrate impedance sensing system (ECIS) to evaluate the pharmacological effects of molybdenum trioxide hybridized Kaempferol nanoparticles (MoHK NPs) against intracellular oxidative stress. Employing gold-microelectrode array wells, we monitored the real-time responses of RAW 264.7 cells to various physical and chemical oxidative stress stimuli. The ECIS-derived biophysical parameters, including impedance, resistance, and capacitance, demonstrated the anti-oxidant properties of MoHK NPs, corroborated by conventional assays. This comprehensive spatial assessment provides a valuable framework for similar cellomics studies.

Keywords: *oxidative stress; cell-nanomaterial interface; ECIS; nanomedicine; semi-synthetic anti-oxidants*

1.Introduction

Cellular oxidative stress is a primary cause of chronic inflammation [1]. Therefore, there is an increasing need to understand the pathophysiology of cellular oxidative stress and develop preventative medication [1–3]. The cells under persistent radical oxygen species (ROS) attack predominate pathophysiological conditions, escalating oxidative stress [4,5]. Further, it activates various transcription factors, which cause the expression of respective genes associated with inflammatory pathways [6,7]. Hence, cells need anti-oxidant to control ROS under severe stress, either by catalysis or through a radical scavenging mechanism [5]. With the advent of cellular oxidative stress, anti-oxidants garnered significant interest as a health supplements. Dietary polyphenols contribute various biological function, including prevention of oxidative stress and degenerative illnesses. They are regarded as effective ROS scavengers because of its aromaticity and hydroxyl groups in a highly conjugated system, they can prevent oxidative damage to biomolecules (lipids, proteins, and DNA) by suppressing cellular oxidative stress and reducing tissue inflammation. Pre-clinical studies show that the long-term consumption of high polyphenol diets offers protection against the emergence of various chronic diseases, including cancer, cardiovascular, diabetes, infectious, and neurodegenerative diseases [6]. However, polyphenols suffer with standardization and bioavailability. For instance, polyphenols may reach the colon because of their insufficient absorption, where they are digested by the gastrointestinal tract (GIT) microbiota and produce several bacterial metabolites. Hence, it can be potentially toxic during prolonged use [8]. Therefore, increasing the bioavailability through different tools such as a prodrug, linker chemistry, bypassing GIT, and size reduction is of prime importance. Nanotherapeutics is a growing novel drug discovery field with several potential advantages over traditional drugs. NPs can be designed with specific properties, such as surface charge, hydrophobicity, and biocompatibility, to enhance interaction with biological systems [9]. The NP-based delivery system has shown improved pharmacokinetics compared to traditional drugs, resulting in increased bioavailability, site-specific delivery, enhanced therapeutic efficacy, reduced toxicity, and stability. The ability to manipulate and use the properties of NPs for targeted delivery has made

nanotherapeutics a rapidly growing area of research and development in drug discovery [10]. Utilizing nano-chemistry, herein, hydrophobic polyphenol, *i.e.,* kaempferol, is hybridized with molybdenum trioxide (MoO_3) NPs to form molybdenum tri-oxide hybridized kaempferol (MoHK) NPs. MoO_3 stands out among transition metal oxides (TMOs) due to its versatile properties and wide range of applications [11,12]. Unlike many other TMOs, MoO_3 can exist in various stoichiometries, with intermediate phases that exhibit distinct biological properties [13]. This variability is crucial for applications in cellular biology. Molybdenum of MoO_x is a well-known cellular micronutrient and metal cofactor for several enzyme, metalloprotein, and possess enzyme mimicking activity [14]. Similarly, Kaempferol has been known to possess anti-oxidant and anti-inflammatory properties [15]. Moreover, the presence of conjugated π-bonds and nucleophilic sites/ steric arrangement resulting from oxygenated functional groups renders Kaempferol a favorable option for coordination with metals [16]. Kaempferol demonstrates both direct and indirect pathways to eliminate reactive oxygen species by producing anti-oxidant enzymes. Kaempferol mitigates oxidative stress by disrupting immune-metabolic and NF-κB signaling pathways [15]. MoO_3 in hybridized systems found to enhance the synergism for effective biomedical properties [16,17]. Owing to its nano chemistry and anti-oxidant activity, herein, MoO_3-hybridized Kaempferol has been chosen as model system to monitor the oxidative stress scavenging assay.

These MoHK NPs are investigated using electric cell-substrate impedance sensing (ECIS) as a potential preventive medicine against differently induced oxidative stress. ECIS provides an edge over other *in vitro* methods due to its *in situ*, *non-invasive*, and real-time monitoring characteristics *via* electrical resistance signals [18–21]. Bioimpedance methods have recently emerged as a promising technique for assessing metastasis, regenerative and personalized medicine, infections, and environmental toxicants [20–23]. Additionally, excluding conventional labeling is possible when resistance is used as a cellular readout. This can restore cells to their natural and physiologically relevant state and avoid their detrimental effects on cellular activities. In addition, the ECIS system provides kinetic data on initial cell attachment and sustained steady-state adhesion in real-time. Therefore, ECIS can discriminate biophysical cellular events like morphological changes, adhesion, proliferation, pathological condition, and response to xenobiotics. Capacitance/resistance/impedance originating from the cellular event, such as motility on or off the working electrode, can provide details with a spatial resolution of less than 1 nm. Thus, ECIS enables quantitative real-time measurement, eliminating the need for periodic frequent sample collection and tedious post-experimental processing.

Herein, the ECIS ZΘ system (Applied Biophysics, USA) with electrode array of eight wells, each containing ten gold-microelectrodes (8W10E), are utilized. ECIS modelling is performed in constant phase element (CPE) alternative to capacitor considering the non-homogeneity of the system. The ECIS system capable of recording impedance (Z), resistance (R), and capacitance (C), at the same time for multiple frequencies. Therefore, it enables a better understanding of the cells' structural and chemical dispersity. The approach works by monitoring changes in the AC impedance of tiny gold-film microelectrodes (*d*: 250 μm) utilized as a growth substrate. Compared to conventional methods, which often rely on invasive procedures and continuous monitoring, using ECIS as an alternative assay platform does not require complex experimental processing with comparable results to cell and animal models. Thus, different physical (photoirradiation and thermal exposure) and chemical (oxidative and inflammatory agents) induced oxidative

stress, and the healing function of nanotherapeutics are studied utilizing ECIS. It is envisioned that this cellular electrical impedimetric assay platform will be a valuable tool in the rapid preclinical investigation of potential anti-oxidant drug leads.

2. Materials and methods

Reagents and materials used for this work is provided in supplementary information (SI).Information on instruments used in this work is provided in SI.

MoO_3 hybridized Kaempferol nanoparticles (MoHK NPs)were synthesized based on our earlier report [24] and the synthesis procedure is provided in SI. Each ECIS chip was pre-treated with 10 mM L-cysteine for 10 min, rinsed thrice with DI water, dried, and stored for further experiments.

Cell sub-culturing and seeding on ECIS chips was carried out as follows :

Once the RAW 264.7 cell line reached approximately 90% confluency, it is selected for sub-culturing. Firstly, the culture medium is aspirated from the T-25 flask. Followed by trypsinization using trypsin-EDTA (~1.5 mL) than incubating T-25 flask at 37 °C for 5 minutes. Post incubation, the cells are detached by gently tapping the sides of flask. Fresh DMEM media is then added to the flask to neutralize the EDTA. The cell suspension is gently pipetted to ensure thorough mixing. A small aliquot of the suspended cells is subsequently transferred to a hemocytometer for cell counting. Prior to cell seeding, the ECIS chips are equilibrated with a serum-free medium inside a CO_2 incubator. Based on the cell count, the cells are transferred to the new growth media and seeded into wells of ECIS chips at a density of approximately 3 to 5 × 10^5 cells/cm^2.

UV light-induced ROS generation was carried out as follows :

For UV irradiation, the cells are transferred into Eppendorf's tube and divided into half as treated and untreated; all the aliquots are incubated for 5 h in a CO_2 incubator before UV exposure. The UV treatment was performed for 2, 5, and 10 min using a UV-C lamp (λ = 254 nm) as a source. Post-irradiated cells were then inoculated in ECIS chip containing wells for bioimpedance measurement. The cells without treatment are chosen as control and PBS as a blank (B).

For heat shock generation, an Eppendorf's tubes were loaded with RAW 264.7 cells (5 × 10^5 cells/cm^2) before heat shock treatment. Following, both sample-treated and untreated vials were cultured in a CO_2 incubator for 5 h. For inducing the heat shock, vials are kept in a hot water bath maintained at 45 °C temperature for 2, 5, and 10 min. Followed by seeding in wells of chips for ECIS analysis. Cells with no treatment acted as control.

Oxidative stress was induced using 3.5 µL of 30% H_2O_2. MoO_3, Kaempferol, and MoHK are added in 5 µg concentration. Ascorbic acid and gallic acid are used as a reference at 27.5 and 38.2 µM [25,26], respectively. DMEM medium without and with H_2O_2 treatment is taken as negative (NC) and positive control (PC), respectively.

A 5 µg of MoO_3 NPs, Kaempferol, and MoHK NPs were inoculated at 16 h in ECIS wells. After a confluent stage, PGE2 of two concentrations (10 µg and 10 ng) was added at 44 h. Similarly, a cell containing DMEM with and without PGE2 treatment was taken as an PC and NC, and PBS as blank for comparative analysis.

Conventional cellular assay was carried out for Cytocompatibility assay a 100 µL aliquot of DMEM containing approximately 5×10^4 RAW 264.7 cells/cm^2 was seeded into 96 well (flat bottom) tissue culture plates with 5, 10, and 30 µg of samples. After 24 h of incubation, 10 µL of MTT labeling reagent (0.5 mg/mL) is added to each well. Following an additional 4 h incubation with the MTT reagent, 100 µL of solubilization buffer is added to each well and incubated for 24 h. Afterward, the solubilized purple formazan crystals were measured

at λ 580 nm.

For H_2O_2 assay RAW 264.7 (5×10^4 cells/cm^2) cells were pre-incubated with test samples and standard anti-oxidants for 24 h. Followed by 100 μM of H_2O_2 was added and incubated for 1 h to determine the influence of test samples. Afterward, an assay buffer was added and kept aside for an additional hour. The intracellular H_2O_2 concentration is determined at an $\lambda_{ex}/\lambda_{em}$ of 490/520 nm.

For Anti-oxidant assay test sample treated RAW 264.7 (5×10^4 cells/cm^2) cells are pre-incubated for 4 h in black-colored polystyrene 96 well plates, followed by treatment with PGE2 (10 μg) and incubated for 24 h. 20 μL DCFDA at a concentration of 100 μM was added into each well and incubated for another 30 min. After the reagent, cells in the medium was maintained in a CO_2 incubator. The fluorescence measured at λ_{ex} of 485 and λ_{em} of 530 nm.

3. Results and Discussion

3.1 ECIS-based cyto-viability assay

Figure:1 shows the representative ECIS well-based electrode system for measuring the bioimpedance against different external stimuli. From the ECIS-cell interface the cell coverage capacitance (C; farad/ F), and cell barrier function are correlated by monitoring the electrical resistance (R/ Ω). With multifrequency ECIS modeling, changes in the capacitance at the cell membrane (C_m; μF/Ω-cm^2), intercellular resistance (R_b; Ω-cm^2), and cell-substrate basolateral adhesion (α; Ω-cm$^{1/2}$) are studied (please refer SI for more information). Due to the specific geometry of gold electrodes and the deduction of external resistive factor, the involvement of electrode capacitance (C_E) and resistance (R_E, R_{med}, and R_{sub}) to the whole circuit becomes negligible [21]. The area of the lateral cell membrane is calculated using the macrophage cellular dimension (radius: 10-20 μm, thickness: 15-30 μm). Refined estimation of the area of the lateral cell membrane accounting for the dimensions of RAW 264.7 cells in equation (S1) enabled us to find the models that best fit our data. This correlation is used to comprehend the physical characteristics of RAW 264.7 cells and its membranous activities, such as adhesion, transport, and signaling. At first, the L-cysteine pretreated ECIS 8W10E wells are subjected to frequency scan and stabilization. L-cysteine facilitates the formation of cell monolayer over the gold-microelectrode owing to binding with filopodia of cells. The cell-free capacitance of the electrode is found to be 30 ± 5 nF.

Figure 2(a) shows no resistance change in initial cell adherence. After 2 h, cells bind on the gold-microelectrode through extracellular matrix (ECM) proteins and filopodia. The cells' attachment and spreading are observed with an increased well resistance. At t = 20 h, the wells are inoculated with test samples, and no cell-substrate detachment is observed other than MoO_3 NPs. Additionally, cell micromotion is traced through oscillating resistance. Until the cell growth reaches its full confluence, asynchronous growth observed in the well-reflected with the gradual increase in resistance. The culture media are replenished at t = 40 and t = 70 h. The sample-treated wells showed faster confluent barrier formation. As observed under the sub-confluence stage, electrode resistance found proportional to the cell numbers with a sudden decrease in resistance post-sample inoculation implied cytotoxicity. Upon reaching confluency, the cell growth-associated morphological changes raised a series of peaks and valleys. The cell status is observed by tracking the resistance at different periods showing a higher resistance for MoHK for prolonged time (**Fig**. S3). The EC_{50} concentration for MoHK NPs is found from dose response curve, which is observed to be ~5 μg (**Fig**. S4). This concentration is used for further experiments

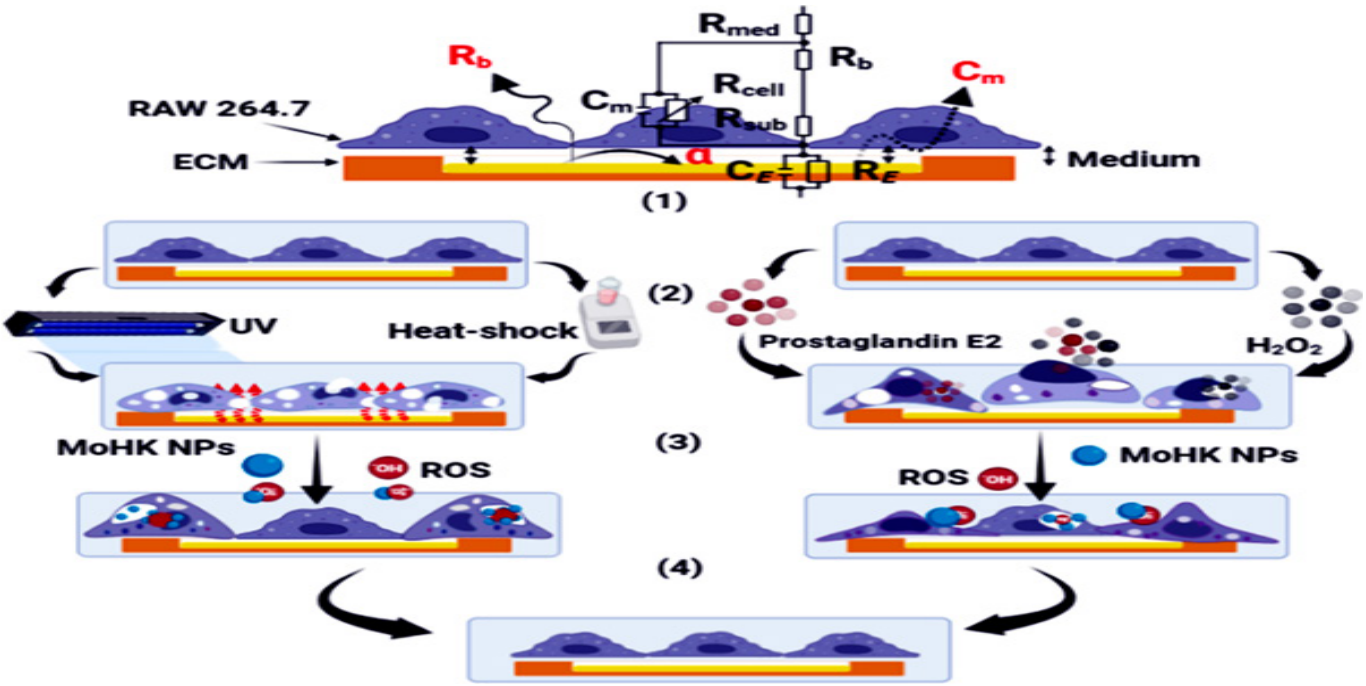

Figure 1. Illustrate the ECIS experimental workflow. ECIS gold-microelectrode chip grown RAW 264.7 cells represented with an equivalent circuit diagram showing the electrical components responsible for bioimpedance, (1) *in situ* grown cells on gold microelectrode. (2) Induction of oxidative stress *via* both physical (left panel) and chemical (right panel) to study biophysical dysfunction in cells. (3) Post-cellular oxidative stress and inoculation of MoHK as an anti-oxidant by ROS scavenging. (4) Cell healing process *via* ROS scavenging mediated by MoHK NPs.

Figure 2(a) shows no resistance change in initial cell adherence. After 2 h, cells bind on the gold-microelectrode through extracellular matrix (ECM) proteins and filopodia. The cells' attachment and spreading are observed with an increased well resistance. At t = 20 h, the wells are inoculated with test samples, and no cell-substrate detachment is observed other than MoO_3 NPs. Additionally, cell micromotion is traced through oscillating resistance. Until the cell growth reaches its full confluence, asynchronous growth observed in the well-reflected with the gradual increase in resistance. The culture media are replenished at t = 40 and t = 70 h. The sample-treated wells showed faster confluent barrier formation. As observed under the sub-confluence stage, electrode resistance found proportional to the cell numbers with a sudden decrease in resistance post-sample inoculation implied cytotoxicity. Upon reaching confluency, the cell growth-associated morphological changes raised a series of peaks and valleys. The cell status is observed by tracking the resistance at different periods showing a higher resistance for MoHK for prolonged time (**Fig**. S3). The EC_{50} concentration for MoHK NPs is found from dose response curve, which is observed to be ~5 µg (**Fig**. S4). This concentration is used for further experiments

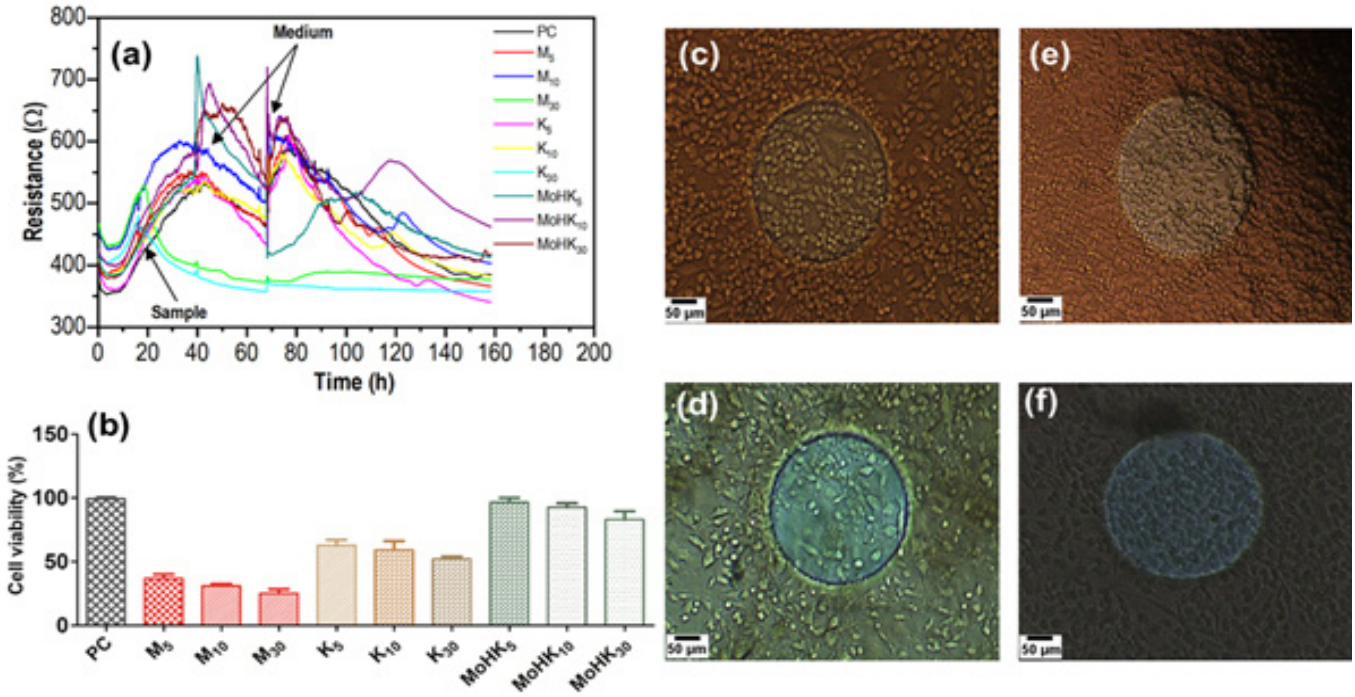

Figure 2. (a) Represents ECIS resistance *vs* time-based cells biophysical response data for all wells. (b) MTT assay with a significant difference in cytocompatibility concerning treated test sample (P<.001) determined using One-way ANOVA and optical microscope images where (c) Positive control, (d) MoO_3, (e) MoHK, and (f) Kaempferol at 20×.

Resistance data suggest that the MoHK NP treated wells formed cell monolayer efficiently compared to MoO_3 and Kaempferol, even at 30 µg. The resistance vs frequency data details the electrical characteristics of cells cultivated on the substrate. The multiple frequency analysis (**Fig**. S5) shows the concentration-effect on cell growth for test samples for range of frequencies (62.5 Hz to 64 kHz), which can be further converted to traceable capacitance and cellular capacitance. It can be observed that there has been a resistance variance for the same concentration of the different tested samples. Changes in the spreading and adhesion of cells on the substrate are reflected in the reduction of resistance with respect to frequency. The magnitude and velocity of this decline suggest a firm substrate and cell adhesion phenomenon. The time-dependent variations in resistance at various frequencies suggest the cell viability and vitality. A fall in resistance was observed with increased frequency because of a build-up in barriers across the cell due to cell growth and proliferation that prevented the passage of electrical current. **Fig**. S6 shows the modeled data for R_b (a), α (b), and C_m (c). Herein, MoHK NPs treated wells exhibit superior cell attachment, spreading/micromotion, and proliferation throughout the study as observed in the model fit providing the R_b, α, and C_m at 0.13 $\Omega.cm^2$, 1.4 $cm.\Omega^5$, and 0.001 $\mu F/cm^2$, respectively, with a minimum drift of 1.7 % and root mean squared error (RMSE) of 0.005.

Conventional MTT assay for MoHK NPs are tested using Raw 264.7 cells. The cells are seeded into 96-well plates, treated with different concentrations *viz*. 5, 10, 30 µg of MoHK NPs as well as pristine MoO_3 and kaempferol along with control (medium) and 10% FBS (fetal bovine serum) for 24 h. It can be seen that 10 µg and above concentrations of kaempferol have shown a toxic effect on cell viability, while MoO_3 and MoHK NPs at the given concentrations found to be non-toxic. MoO_3 NPs at 5 and 10 µg and MoHK NPs at concentrations 5, 10, and 30 µg have shown no adverse effect on cell viability and proliferation. Notably, both MoO_3 and MoHK NPs are found to be non-cytotoxic and did not elicit a negative response with cell viabilities for all dilutions tested (**Fig.** 2b). However, at 30 µg both pristine test samples enabled a drastic decline in the resistance, indicating a detrimental effect on the treated cell lines. This particular result is in coherence with the MTT assay results. Microscopic images taken at t = 70 h show cells attached to gold-microelectrode. Cell proliferation is observed in the order of MoHK > control > kaempferol > MoO_3. Distinctively, MoHK and kaempferol possess superior cytocompatibility at higher doses of 30 µg (**Fig**. 2 c-f). In the resistance *vs* time plot, a high concentration of MoO_3 shows cell mortality, as observed with decreased resistance response. Cells with high dosing of MoO_3 NPs caused cell death and lost the adherence character. Hence, detached from the gold microelectrode. MoHK provided superior cell viability compared to MoO_3 and kaempferol, even at a high concentration of 30 µg. This ECIS data is validated with the *in vitro* cell viability assay using MTT dye and found to be identical. The cyto-viability studies ensured the biocompatibility of the nanotherapeutics.

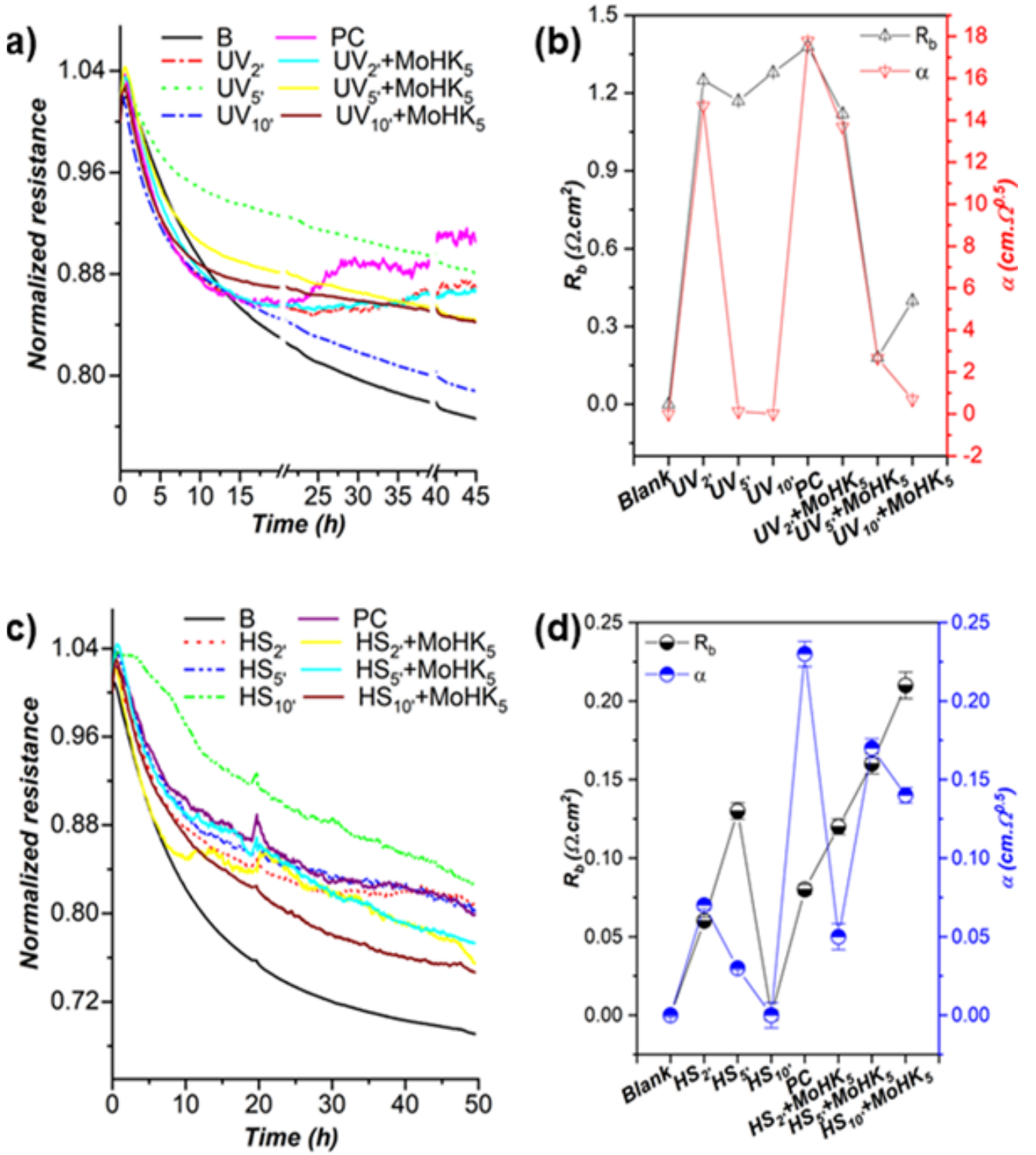

Figure 3. (a) ECIS data for RAW 264.7 cells treated with UV-irradiation (λ_m = 254 nm) and (b) its derived R_b and α values. (c) ECIS results for heat shock treated (45 ˚C) cells and (d) its corresponding R_b and α values.

UV rays cause a cascade of inflammatory responses, including the release of ROS, proinflammatory cytokines, and activation of the pain sensory pathway. Increased phospholipase activity may also occur due to oxygen radical-induced peroxidation of membrane lipids. The UV-C rays can trigger the generation of ROS, which further increases the concentration of proinflammatory cytokines and other mediator pathways such as EP4, EP2, PGE2-EP4, and LPS. To study this, a pre-incubated cells are exposed to UV radiation for 2 (acute), 5, and 10 (extended) min for both untreated and test sample treated cell lines, followed by real-time stress monitoring using ECIS. Cells exposed to harsh UVC light are subjected to determination of Z, R, and C to correlate the cell phase changes, serving as a metric for assessing the biophysical damage. This insight can further help in developing preventive strategies [27].

In **Fig.** 3(a), the cells inoculated with MoHK NPs are stable at the initial period compared to positive control and untreated cell lines. This strong cellular regeneration further favored the formation of an intact cell barrier. The wells covered in confluent cell layers is scanned to determine the impedance at different frequencies. Localized differences observed in the resistance measurements indicate the heterogeneity of the cell layer on the substrate. For better insights on cell barrier and micromotion, resistance/capacitance is recorded at low frequency, *i.e.,* 62.5 Hz (**Fig**. S6 (a) and (b)). Inter and intra changes in resistivity among the wells are compared to correlate the biophysical phenomena (**Fig.** S6 c). Here, 2 min UV-irradiation accelerated cell micromotion. In comparison, 5 min exposure may initiate cellular agitation observed in wells without MoHK. In the presence of MoHK, a distinct observation indicates that cells might be nourished with ROS scavenging species, tolerating the acute irradiation, and restricting the micromotion. This contrasts with the MoHK wells treated for 10 min. These observations are further supported by modeled data in **Fig**. S7, showing a decrease in R_b and an increase in α for MoHK-treated wells with no significant difference in C_m. The R_b and α value at 25 h, as shown in **Fig**. 3(b), provide insights into the effect of UV irradiation on a cell-electrode interface. During the UV treatment, the cell tight junction seems loosened but regains its morphology and ECM for MoHK NPs inoculated wells.

3.2 Heat-shock mediated ROS and effect of MoHK NPs

An optimal temperature is desired for cellular homeostasis. However, exposure to abrupt heat shock can cause cellular stress, modifying the biochemical and physical processes. Herein, the ECIS method assesses the biophysical phenomena by applying heat shock on RAW 264.7 cells. The interlinking mechanism between temperature-induced stress and changes in cellular function is studied *via* electrical impedance. **Fig.** 3(c) shows that cell vitality correlated with resistance change. Heat shock triggered cell agitation, causing migration resulting in higher impedance readings. However, MoHK NPs supported better recovery after heat shock for various times, *i.e.,* 2-, 5-, and 10-min. Cells observed to be stress-resistant as observed with low degree of impedance change. From **Fig.** S8 (a-b), 2 min heat shock-induced and MoHK NP-treated wells are comparable with positive control. The shock

resulted in cell micromotion causing an increased resistance. However, no characteristic resistance change is observed with prolonged exposure time. Additionally, from the post-shock treated well, an increased capacitance is also observed due to current permeated through ruptured cells. Untreated wells showed a linear increase in capacitance compared to a decreasing trend for MoHK-treated wells. Here, MoHK may acted as a shock absorber by scavenging ROS. Thus, protecting the cell and its ECM. Resistance deviation for the cells with heat shock is comparable to control (**Fig.** S8c). An increase in heat shock time is reflected with increased resistance. Notably, the well exposed to a 10-minute heat shock exhibited the highest resistance among the tested wells. Presumably, increased cell debris adhered to the micro-electrodes causing the high barrier resistance, evidenced by the fitted model for R_b shown in **Fig**. 2(d), derived from raw data in **Fig**. S9. This result indicates a rapid formation of cell barrier during post heat-shock for all MoHK treated wells, even superior to positive control. However, this initial rapid increase in R_b values could be attributed to increased cell-substrate adherence, which can also alter resistance. The increased cell-substrate attachment can also be due to the recovery of the cell's normal function influenced by MoHK, leading to a tighter and more stable cell barrier. Distinguishingly, for MoHK-treated wells, the α values increased linearly concerning heat-shock time. A slower rate of impedance change is observed in the other sample-treated wells, indicating less susceptibility to temperature-induced morphological distortion. Therefore, MoHK acted as a shock absorber by tolerating the heat- shock generated ROS and improving the cells' vitality. MoHK stabilized the heat shock-induced cellular oxidative stress in a time-dependent manner.

3.3 H_2O_2 generated ROS and MoHK as a scavenger

The H_2O_2 facilitates redox sensing and signaling inside the cell. H_2O_2 generation, transport, capture, and biological repercussions are well studied [28]. The high level of H_2O_2 triggers the radical initiation, expanding the oxidative pathways. A protective effect of MoHK is observed against H_2O_2-induced oxidative stress (**Fig.** 4 a). The anti-oxidant response from MoHK NPs is found to supersede natural anti-oxidants, *i.e.,* ascorbic acid (AA) and gallic acid (GA), even at the 10-fold concentration difference. After 7 h of sample inoculation, 1 mM of H_2O_2 is added at t= 29 h. A fall in cell resistance is observed, ascribed to the shrinkage of cells due to the oxidative stress affected by H_2O_2. Interestingly, MoHK-treated cells had robust cellular integrity compared to standard references. MoHK effectively supported the cells under stress conditions. Therefore, treated well's resistance is comparable with standards. MoHK has provided prolonged anti-inflammatory activity with high resistance up to t = 70 h, augmenting a similar effect to gallic acid and excelling effectiveness compared to AA.

A change in resistance with respect to frequency is represented in **Fig.** S10. It can be observed that both at low and high frequencies, the test samples treated wells exhibited higher resistance comparable to PC and blank. A reduction trend in resistance is marked by an increase in frequency in ECIS wells in the order of PC>$MoHK_5$>GA>M_5>AA>K_5>blank. Importantly, wells treated with MoHK NPs show better proliferation than standard anti-oxidant and pristine cells seeded well. **Fig.** S11 represents the wells' resistance deviation (S.D.) histogram. Notably,

the wells treated with MoHK NPs demonstrated a minimal shift in resistance response attributed to reduced cell micromotion. Further, PC wells showed a higher change in resistance response due to cell layer formation without oxidative stress. The remaining wells exhibited similar observations. Cell biophysical parameters are inferred from modeled data in **Fig.** S12 and compiled in **Fig.** 4(b). This demonstrates that MoHK-treated cells supported a tight junction development after H_2O_2 exposure, unlike other wells with no significant change. In contrast, MoHK untreated wells showed an impaired formation of cell tight junctions, evidenced by a flat curve in R_b and a decrease over α over-time.

A conventional H_2O_2 assay is performed correlating the oxidation of H_2O_2 to validate the ECIS results. The impact of test samples *viz.,* Kaempferol, MoO_3 NPs, and MoHK NPs on intracellular H_2O_2 levels is determined. **Fig**. 4(c) shows that pretreatment with MoHK NPs significantly reduced intracellular H_2O_2 compared to other studied samples, suggesting a potential H_2O_2 scavenging activity. This is further validated by observing cell status inoculated on gold-microelectrode in ECIS after H_2O_2 addition (*t* = 30 h) using an optical microscope (**Fig**. 4(d-i)).

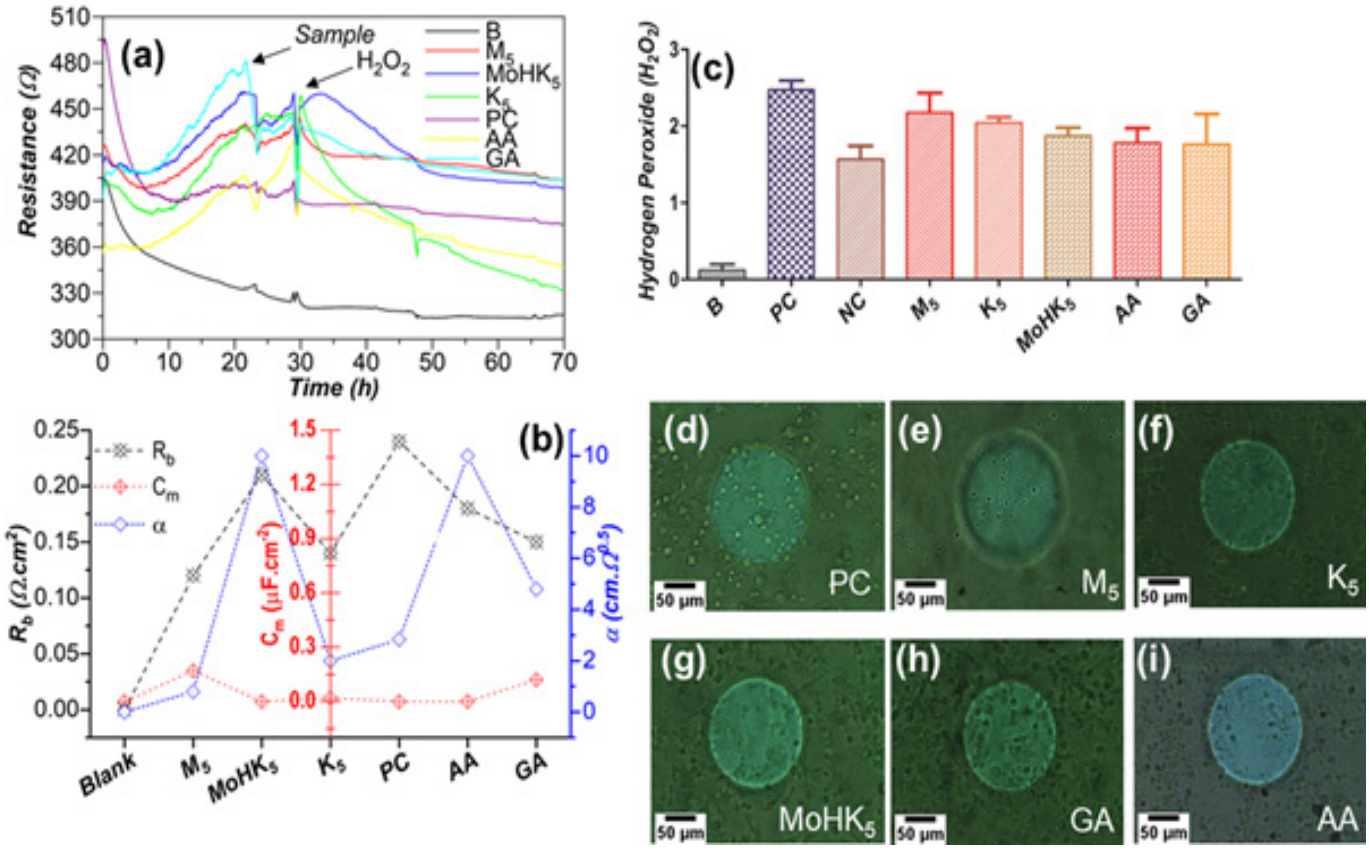

Figure 4. (a) H_2O_2-induced oxidative stress and corresponding anti-oxidant activity of the treated sample. (b) R_b α, and C_m derived from ECIS data. (c) Intracellular H_2O_2 assay with a significant difference in anti-oxidant response corresponding to test sample treatment (P<.05) determined using One-way ANOVA. (d)-(i) Optical microscopic images of gold micro-electrodes wells at 30 h (20×; scale-50 μm).

3.4 PGE2-induced cell oxidative stress and role of MoHK NPs

Inflammation is important to explore as it potentiates several diseases and disease-causing factors [29,30]. An ECIS-mediated bioimpedance investigated post-inflammation induction and subsequent anti-inflammatory activities of test samples (**Fig.** 5a). The inflammation is chemically induced using PGE2, well known as a potent pro-inflammatory cytokine activating EP4 pathway. PGE2 generation elicits inflammation and alters key cytokines such as IL-1β, IL-6, and IL-23. PGE2 also inhibits T cell receptor signaling, and proliferation leads to chronic inflammation diseases. EP4 pathway-mediated chronic inflammation is induced with lethal (10 µg) and sub-lethal (10 ng) concentrations of PGE2. The cells are inoculated with samples at t = 22 h after the grown cell is attached to the substrate. The 10 µg MoHK treated cells retain better anti-inflammatory (50% effective) against 10 µg PGE2. The µg concentration of MoHK is highly effective in controlling cellular inflammation against the ng concentration of PGE2.

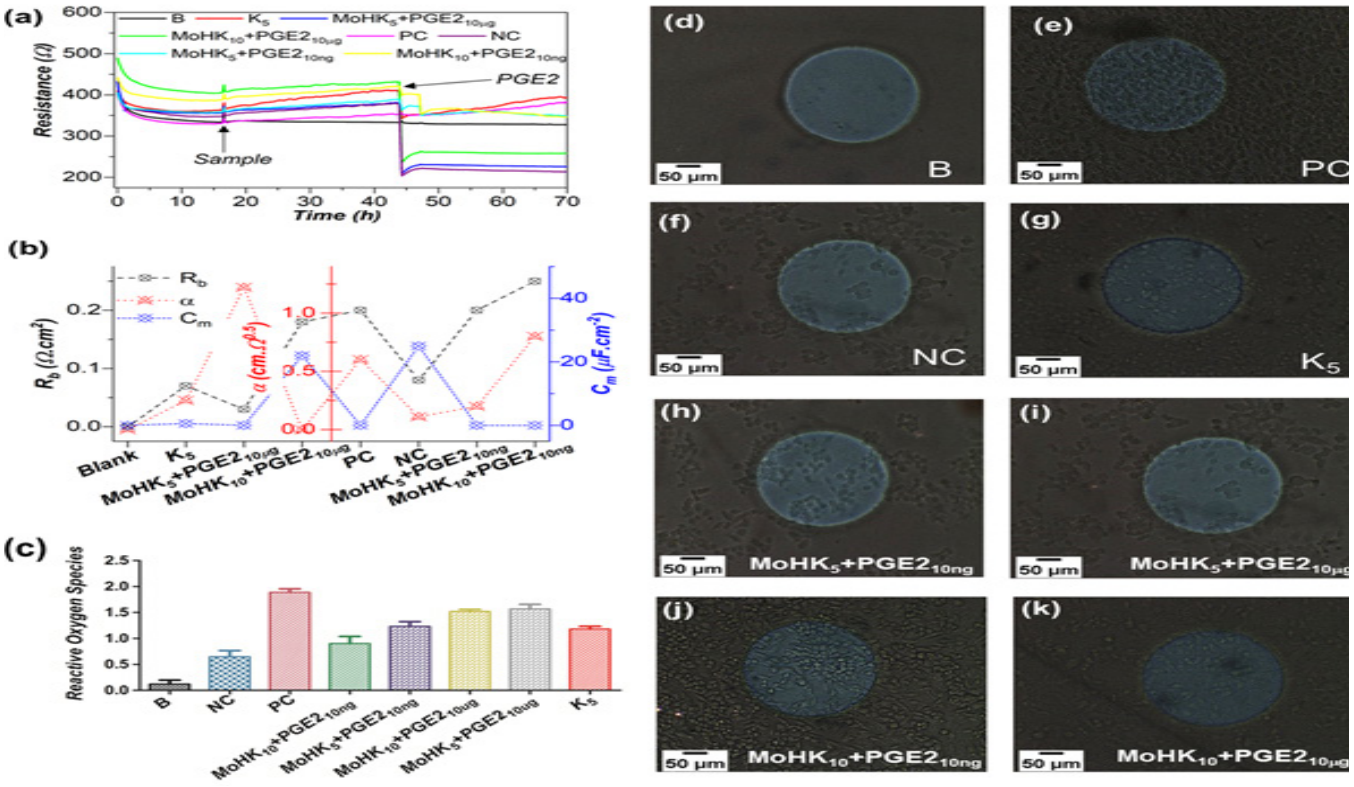

Figure 5. (a) ECIS data for effect of test sample on PGE2 induced inflammation at lethal and sub-lethal concentrations (b) Shows R_b, α, and C_m value derived from ECIS data, (c) DCFDA assay with significant difference in anti-oxidant-based anti-inflammatory response corresponding to test sample treatment (P<.001) determined using One-way ANOVA, and (d-k) Optical images of cells on gold micro-electrode in ECIS array at 60 h (20×).

In **Fig**. 4(b), the C_m measured for $MoHK_5$ treated with $PGE2_{10\mu g}$ is superior to $MoHK_{10}$ with $PGE2_{10ng}$. Likewise, calculated R_b and α shows an increasing trend with an increased concentration of MoHK for both lethal and sub-lethal doses of PGE2. This could be due to the anti-oxidant properties of nanotherapeutics under investigation *via* modulating the EP4 pathway by reducing the production of inflammatory cytokines, further inhibiting the activation of nuclear factor-kappa B (NF-κB). Our hypothesis is also supported by earlier *in vivo* studies [31]. In addition, MoHK can have a direct anti-inflammatory effect by reducing the activation of immune cells and ROS production, reducing cell necrosis. This can be observed by increased barrier resistance, promoting normal cell growth under inflammatory stress, and facilitating the formation of a cell monolayer at gold-microelectrodes by MoHK. Similarly, MoHK concentration-based resistance is also traced for a lethal dose of PGE2. However, the degree of resistance for lethal doses is lower than PC. The effectiveness of MoHK NPs in mitigating PGE2-induced oxidative stress within cells is also evaluated using the conventional DCFDA assay. In brief, RAW 264.7 cells are pretreated with Kaempferol, MoO_3, and MoHK NPs. From **Fig**. 4 (c), the test samples treated cells considerably decreased the oxidative stress than those treated with PGE2 alone. This finding indicates an anti-inflammatory potential of MoHK NPs comparable to PC. These results are further supported by the microscopic images acquired after adding PGE2 (t = 60 h) in all the wells (**Fig.** 4d-k).

ECIS's ability to electrically distinguish various biophysical cellular processes such as morphology, micromotion, adhesion, apoptosis, and proliferation in impedance signal is predominant in investigating the therapeutic potential of natural, synthetic, and semi-synthetic novel drug-like molecules. We envisage that ECIS, with attributes like non-invasiveness, real-time monitoring, and *in-situ* cell analysis, can pace up the pathology and succeeding therapeutics to understand and address the critical factors of cell damage and repairs.

4. Conclusions

The ECIS-based bioassay effectively demonstrated the dynamic cellular responses to oxidative stress and nanotherapeutics. The induction of intracellular oxidative stress has been systematically studied with RAW 264.7 cells. ECIS-derived cell behavior analyses complement conventional cytocompatibility and anti-oxidant/-inflammatory assays. The findings confirm that MoHK NPs possess significant anti-oxidant properties, as indicated by changes in cell-substrate resistance, membrane capacitance, and intercellular resistance. This study highlights the potential of ECIS as a robust tool for non-invasive pharmacological evaluation, paving the way for future research on cell-nanomaterial interactions and the development of novel therapeutic strategies.

Declaration of competing interest

The authors declare that they have no known competing financial interests.

Acknowledgments

G.P thankfully acknowledges the support of ICMR New Delhi for the award of Senior Research Fellowship (Grant no. 5/3/8/26/ITR-F2020). This

work was supported by SERB-DST, Government of India through Start-up Research Grant (SRG/2019/000238).

References

[1] S. Fulda, A.M. Gorman, O. Hori, A. Samali, Cellular stress responses: Cell survival and cell death, Int J Cell Biol 2010 (2010). https://doi.org/10.1155/2010/214074.

[2] S. Muralidharan, P. Mandrekar, Cellular stress response and innate immune signaling: integrating pathways in host defense and inflammation, J Leukoc Biol 94 (2013) 1167–1184. https://doi.org/10.1189/jlb.0313153.

[3] V. Calabrese, C. Cornelius, C. Mancuso, G. Pennisi, S. Calafato, F. Bellia, T.E. Bates, A.M. Giuffrida Stella, T. Schapira, A.T. Dinkova Kostova, E. Rizzarelli, Cellular stress response: A novel target for chemoprevention and nutritional neuroprotection in aging, neurodegenerative disorders and longevity, Neurochem Res 33 (2008) 2444–2471. https://doi.org/10.1007/s11064-008-9775-9.

[4] K. Rehman, M.S.H. Akash, Mechanism of Generation of Oxidative Stress and Pathophysiology of Type 2 Diabetes Mellitus: How Are They Interlinked?, J Cell Biochem 118 (2017) 3577–3585. https://doi.org/10.1002/jcb.26097.

[5] N. Fedoroff, Redox regulatory mechanisms in cellular stress responses, Ann Bot 98 (2006) 289–300. https://doi.org/10.1093/aob/mcl128.

[6] T. Hussain, B. Tan, Y. Yin, F. Blachier, M.C.B. Tossou, N. Rahu, Oxidative Stress and Inflammation: What Polyphenols Can Do for Us?, Oxid Med Cell Longev 2016 (2016). https://doi.org/10.1155/2016/7432797.

[7] S. Muralidharan, P. Mandrekar, Cellular stress response and innate immune signaling: integrating pathways in host defense and inflammation, J Leukoc Biol 94 (2013) 1167–1184. https://doi.org/10.1189/jlb.0313153.

[8] H.D. de Freitas Queiroz Barros, M.R. Maróstica Junior, Phenolic Compound Bioavailability Using In Vitro and In Vivo Models, in: Bioactive Compounds, Elsevier, (2019): pp. 113–126. https://doi.org/10.1016/B978-0-12-814774-0.00006-2.

[9] E.C. Dreaden, A.M. Alkilany, X. Huang, C.J. Murphy, M.A. El-Sayed, The golden age: Gold nanoparticles for biomedicine, Chem Soc Rev 41 (2012) 2740–2779. https://doi.org/10.1039/c1cs15237h.

[10] S. Mitragotri, J. Lahann, Physical approaches to biomaterial design, Nat Mater 8 (2009) 15–23. https://doi.org/10.1038/nmat2344.

[11] Z.Q. Wang, Y.W. Pan, J. Wu, H. Bin Qi, S. Zhu, Z.J. Gu, A bibliometric analysis of molybdenum-based nanomaterials in the biomedical field, Tungsten 6 (2024) 17–47. https://doi.org/10.1007/s42864-023-00225-1.

[12] I.A. de Castro, R.S. Datta, J.Z. Ou, A. Castellanos-Gomez, S. Sriram, T. Daeneke, K. Kalantar-zadeh, Molybdenum Oxides – From Fundamentals to Functionality, Advanced Materials 29 (2017) 1701619. https://doi.org/10.1002/ADMA.201701619.

[13] G. Schwarz, J. Schulze, F. Bittner, T. Eilers, J. Kuper, G. Bollmann, A. Nerlich, H. Brinkmann, R.R. Mendel, The Molybdenum Cofactor Biosynthetic Protein Cnx1 Complements Molybdate-Repairable Mutants, Transfers Molybdenum to the Metal Binding Pterin, and Is Associated with the Cytoskeleton, Plant Cell 12 (2000) 2455–2471. https://doi.org/10.1105/TPC.12.12.2455.

[14] G. Pandey, M. Marimuthu, P. Kanagavalli, V. Ravichandiran, K. Balamurugan, M.

Veerapandian, Chitosanylated MoO_3-ruthenium(II) nanocomposite as biocompatible probe for bioimaging and herbaceutical detection, ACS Biomater Sci Eng 5 (2019) 3606–3617. https://doi.org/10.1021/acsbiomaterials.9b00575.

[15] S. Hofer, S. Geisler, R. Lisandrelli, H.N. Ngoc, M. Ganzera, H. Schennach, D. Fuchs, J.E. Fuchs, J.M. Gostner, K. Kurz, Pharmacological targets of kaempferol within inflammatory pathways—a hint towards the central role of tryptophan metabolism, Antioxidants 9 (2020) 1–19. https://doi.org/10.3390/antiox9020180.

[16] L.Y. Tu, J. Pi, H. Jin, J.Y. Cai, S.P. Deng, Synthesis, characterization and anticancer activity of kaempferol-zinc(II) complex, Bioorg Med Chem Lett 26 (2016) 2730–2734. https://doi.org/10.1016/j.bmcl.2016.03.091.

[17] M. Marimuthu, B.P. Kumar, L.M. Salomi, M. Veerapandian, K. Balamurugan, Methylene blue-fortified molybdenum trioxide nanoparticles: harnessing radical scavenging property, ACS Appl Mater Interfaces 10 (2018) 43429–43438. https://doi.org/10.1021/ACSAMI.8B15841.

[18] A.K. Yagati, S.G. Chavan, C. Baek, D. Lee, M.H. Lee, J. Min, RGO-PANI composite Au microelectrodes for sensitive ECIS analysis of human gastric (MKN-1) cancer cells, Bioelectrochemistry 150 (2023) 108347. https://doi.org/10.1016/j.bioelechem.2022.108347.

[19] J.S. Kresge, C. T., Leonowicz, M. E., Roth, W. J., Vartuli, J. C., Beck, ²»ÉøÍ¸ÐÔµÄ © 19 9 2 Nature Publishing Group, Nature 359 (1992) 710–713.

[20] M. Marimuthu, C. Park, S. Kim, C.S. Choi, Real-time electrical measurement of L929 cellular spontaneous and synchronous oscillation, Int J Nanomedicine 7 (2012) 83–93. https://doi.org/10.2147/ijn.s28465.

[21] C. Lo, C.R. Keese, I. Giaever, Impedance Analysis of MDCK Cells Measured by Electric Cell-Substrate Impedance Sensing, Biophys J 69 (1995) 2800–2807. https://doi.org/10.1016/S0006-3495(95)80153-0.

[22] J. Hong, K. Kandasamy, M. Marimuthu, C.S. Choi, S. Kim, Electrical cell-substrate impedance sensing as a non-invasive tool for cancer cell study, Analyst 136 (2011) 237–245. https://doi.org/10.1039/c0an00560f.

[23] M.R. Pennington, G.R. Van de Walle, Electric Cell-Substrate Impedance Sensing To Monitor Viral Growth and Study Cellular Responses to Infection with Alphaherpesviruses in Real Time, MSphere 2 (2017) 1–12. https://doi.org/10.1128/msphere.00039-17.

[24] G.R. Pandey, P. Kanagavalli, K. Karnam, K. Thanigai Arul, P. Monisha, C.L. Dong, J.L. Chen, M. Veerapandian, J. Nirmal, Molybdenum trioxide hybridized kaempferol: double-powered nanosystem for salvaging oxidative stress and electrochemical immunoprobing of interleukin-6, Mater Today Chem 24 (2022) 100809. https://doi.org/10.1016/j.mtchem.2022.100809.

[25] O.I. Aruoma, A. Murcia, J. Butler, B. Halliwell, Evaluation of the Antioxidant and Prooxidant Actions of Gallic Acid and Its Derivatives, J Agric Food Chem 41 (1993) 1880–1885. https://doi.org/10.1021/jf00035a014.

[26] G. Schuster, A.A. do Amaral, J. Wyzykowski, M.G.P. Valenga, N.L. Boschen, G.A.R. Maia, P.R.P. Rodrigues, A.L. Gallina, Ascorbic acid as antioxidant for soybean biodiesel, Orbital 10 (2018) 183–190. https://doi.org/10.17807/orbital.v10i3.1097.

[27] L. Lisi Hruza, A.P. Pentland, Mechanisms of UV-induced inflammation, Journal of Investigative Dermatology 100 (1993) S35–S41. https://doi.org/10.1038/jid.1993.21.

[28] H. Sies, Hydrogen peroxide as a central redox signaling molecule in physiological oxidative

stress: Oxidative eustress, Redox Biol 11 (2017) 613–619. https://doi.org/10.1016/j.redox.2016.12.035.

[29] P. Hunter, The inflammation theory of disease. the growing realization that chronic inflammation is crucial in many diseases opens new avenues for treatment, EMBO Rep 13 (2012) 968–970. https://doi.org/10.1038/embor.2012.142.

[30] D. Furman, J. Campisi, E. Verdin, P. Carrera-Bastos, S. Targ, C. Franceschi, L. Ferrucci, D.W. Gilroy, A. Fasano, G.W. Miller, A.H. Miller, A. Mantovani, C.M. Weyand, N. Barzilai, J.J. Goronzy, T.A. Rando, R.B. Effros, A. Lucia, N. Kleinstreuer, G.M. Slavich, Chronic inflammation in the etiology of disease across the life span, Nat Med 25 (2019) 1822–1832. https://doi.org/10.1038/s41591-019-0675-0.

[31] M. He, T. Ichinose, S. Yoshida, T. Ito, C. He, Y. Yoshida, K. Arashidani, H. Takano, G. Sun, T. Shibamoto, PM2.5-induced lung inflammation in mice: Differences of inflammatory response in macrophages and type II alveolar cells, Journal of Applied Toxicology 37 (2017) 1203–1218. https://doi.org/10.1002/jat.3482.

Appendix A. Supplementary data
Supplementary Information
Bioimpedance-based investigation of anti-oxidant nanotherapeutics against intracellular oxidative stress

Gaurav Pandey[1,2], Murugan Veerapandian[1,2]*

[1]*Electrodics and Electrocatalysis Division, CSIR-Central Electrochemical Research Institute, Karaikudi 630 003, Tamil Nadu*

[2]*Academy of Scientific & Innovative Research (AcSIR), Ghaziabad 201 002, India*

Reagents and materials

For all the assays, a mammalian-macrophage RAW 264.7 cell lines were used, procured from NCCS, Pune, and sub-cultured using Dulbecco's modified eagle medium (DMEM), 10% (v/v) fetal bovine serum (FBS), and 50 µg/ml Streptomycin obtained from Pan Biotech. For cellular studies 3-(4,5-dimethylthiazol-2-yl)-2,5-diphenyltetrazolium bromide (MTT), 2',7'-dichlorofluorescein diacetate (DCFDA), MAK164 (H_2O_2 assay), and EZAssay™ thiobarbituric reactive species (TBARS) assays kits were procured from Roche, Sigma-Aldrich, and Hi-Media, respectively. All the assays are performed following the manufacturer's instructions. Hydrogen peroxide (H_2O_2), L-cysteine, and Prostaglandin E2 (PGE2) were purchased from Hi-Media and TCI, respectively. All the chemicals other than biological samples and PGE2 were stored in ambient conditions and used without further processing. The autoclaved DI water (18.2 MΩ.cm^{-1}) from the Millipore system was used for all the experimental works.

Instrumentation

The cells were incubated in Heracell™ vios 160*i* CO_2 incubator (ThermoFisher™) maintained at 40% relative humidity, 37 °C temperature, and 5% CO_2. The ECIS® (Electric Cell-substrate Impedance Sensing) ZΘ was used to investigate the cytocompatibility of nanosystem using a customized 8W10E (8 wells ten electrodes) gold-microelectrode system from Applied Biophysics, Troy, New York, and all the experiments were conducted at multiple frequency modes. The Autoclave SLEDD, Equitron, was used for sterilization and decontamination processes. The absorbance/fluorescence was performed using a Synergy SpectraMax M3 multi-plate reader. Morphological characteristics of the cells were visualized in the inverted optical microscope, Lawrence and Mayo India Pvt. Ltd, India (LM-52-3501).

MoO_3 hybridized Kaempferol nanoparticles (MoHK NPs)

The MoHK NPs were synthesized based on our earlier report (Pandey et al., 2022). In brief, an aqueous dispersion of MoO_3 NPs was homogenized using a bath sonicator and kept under magnetic stirring at 65°C and 800 rpm. A probe sonication mediated hybridization on MoO_3 NPs was done by dropwise addition of alcoholic dispersion of Kaempferol. The resulting particles

were centrifuged, washed thrice, and vacuum dried at 50°C for 2 hours to obtain MoHK powder. **Fig**. S1 represents the HR-TEM images, revealing the average particle size of 2-8 nm and 12-18 nm for MoO_3 and MoHK NPs, respectively. The chemical integrity of the prepared NPs is studied from Raman spectroscopy (**Fig.** S2).

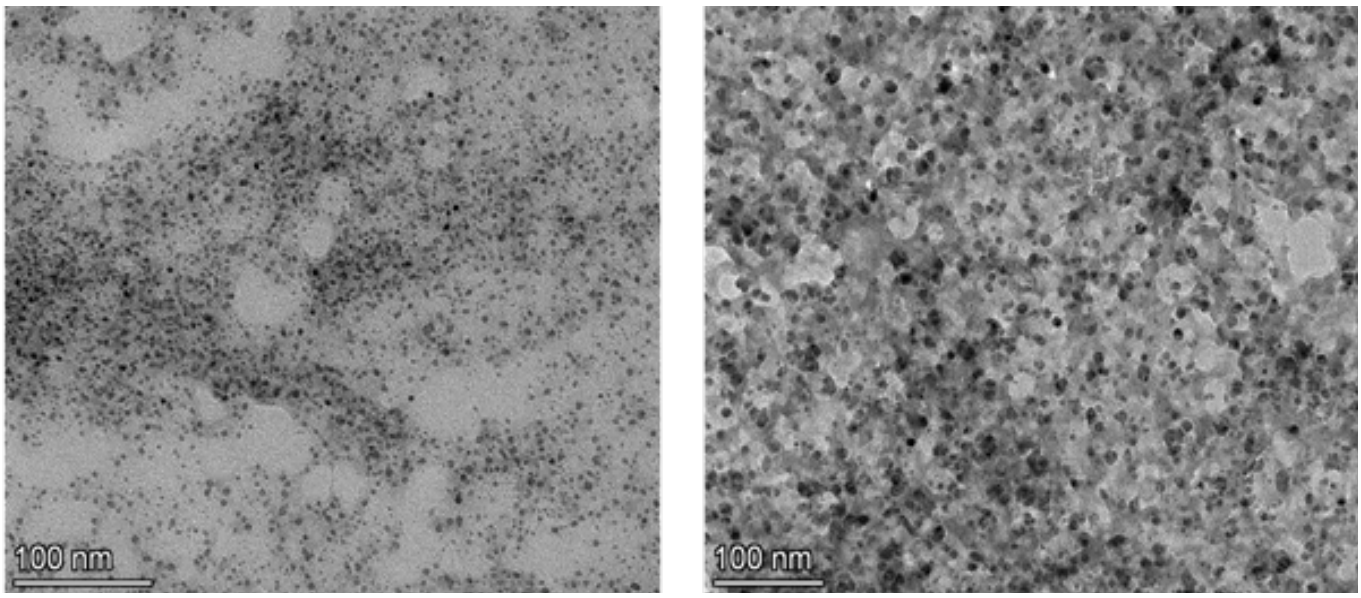

Figure S1. HR-TEM image for showing the well-distributed MoO3 (davg 2- 8 nm) and MoHK (davg = 12-18 nm) NPs.

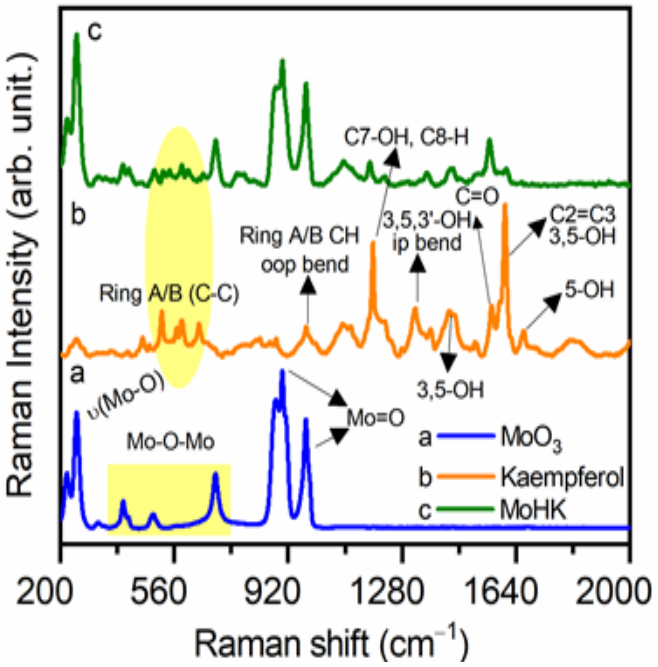

Figure S2. Raman spectrum for synthesized MoHK NPs compared with MoO3 and kaempferol.

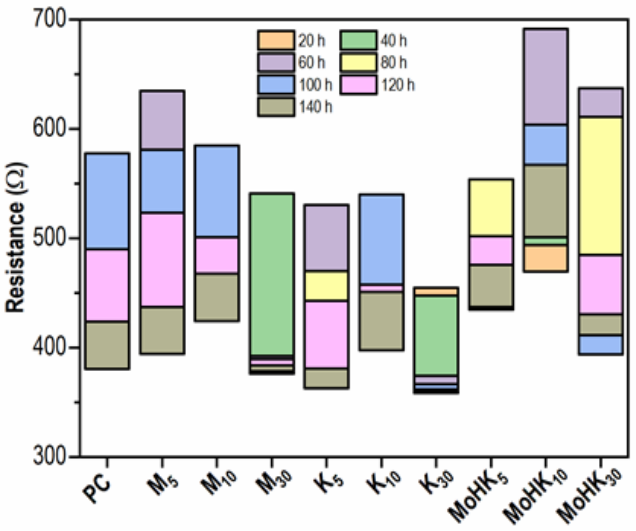

Figure S3. Resistance value for different sample treated wells recorded at different time from ECIS.

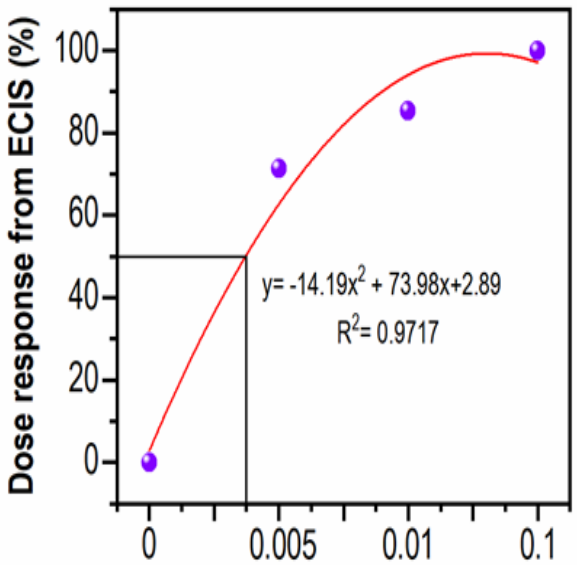

Figure S4. Dose response curve derived from ECIS

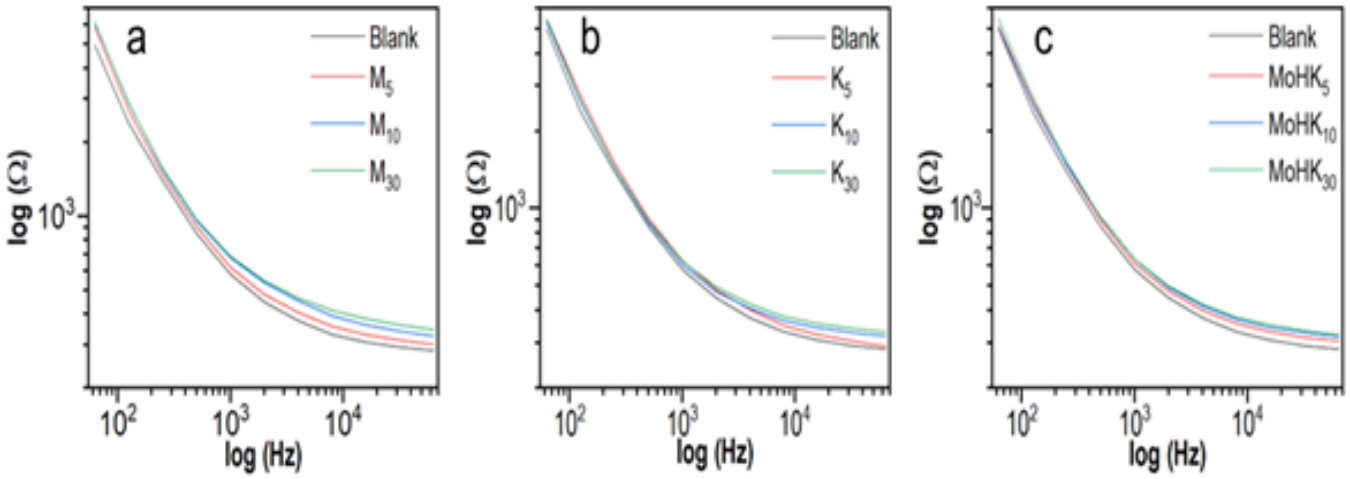

Modeling of ECIS data:

The modeling of ECIS resistance data aimed to obtain biophysical insights on macrophage cells during external stimuli and after test sample treatment. Three independent variables were compared to understand the biophysical behavior *viz.,* membrane capacitance (C_m) arising from the phospholipid cell membrane and interstitial spaces, cell-cell junction resistance (α), and resistance beneath the cells and gold microelectrode (R_b) from ECM and its components such as cytoplasm and the adhesion protein. C_m is the average capacitance of the cell plasma membranes, and R_b is an intrinsic barrier resistivity that provides the insight permeability on restriction to the flow of electric current by a material at cell-cell barriers. In comparison, α provides the current barrier underneath the cells and thus describes changes in the region beneath the cells. R_b can be calculated as following equation (1) [S1]:

$$r_c \left(\frac{p}{h}\right)^{1/2}$$

…… (S-1)

Here,

r_c stands for the spread cell's effective radius,

ρ for the solution's resistivity, and

h is the distance separating the cells and the substrate.

One can study the RAW 264.7 cellular behavior at the interface with variable factors. It is observed that the differences in the impedance values are associated with changes in the effective radius of the cells and the typical separation between the cells and the substratum. This information has profound importance for the study of cell morphology, offering useful resources for cellomics.

An electrical component-based mathematical model of the cell-substrate interface is used to determine the α, R_b, and C_m values. In brief, an electrical signal of alternating current (AC) is used to measure the resistance of this interface, and the resulting resistance data are examined to calculate the α, R_b and C_m values. Changes in the cell-substrate interface, such as modifications to cell shape or spreading, have an impact on the α and can be determined from the slope of the linear section of the resistance curve. Thus, a rate of change in resistance over time is represented by this slope, which is connected to cellular behavior. Similarly, the R_b is sensitive to changes in the cell-substrate interface, such as alterations in cell morphology, adhesion, and spreading. As a result, changes in barrier resistance over time can provide insight into cellular processes, such as the formation and disruption of the cell monolayer or barrier and the effects of various treatments or conditions on cellular behavior. C_m is calculated by fitting the impedance data to the appropriate circuit model. The cell-substrate interface impedance can be represented as a circuit. This capacitance might change depending on the condition of the cell. Size and shape of the cells can change during an experiment which can reflect in C_m.

At the same time, in some cases calculating parameter such as α for all values during the entire length of time might not be possible due to incoherent in the cell behavior in longer experiment. Further, it can also be ascribed with the complexity of cell-substrate contact and the range of variables that might influence the electrical characteristics. For modeling, establishing a stable and tight barrier over the substrate is desired for convenient measurement of interfacial resistance. Determining the barrier resistance for the entire experiment would be challenging in case of a discontinuous barrier over the substrate. Similarly, measuring the Rb precisely might not be feasible if there is poor contact between the electrodes and substrate or cell-to-cell contact. ECIS system would measure C_m for the entire cell-substrate interface as well as additional structures from the cellular microenvironment, such as ECM or extracellular vesicles. The overall resistance may change due to the existence of these structures, which could make the C_m less noticeable.

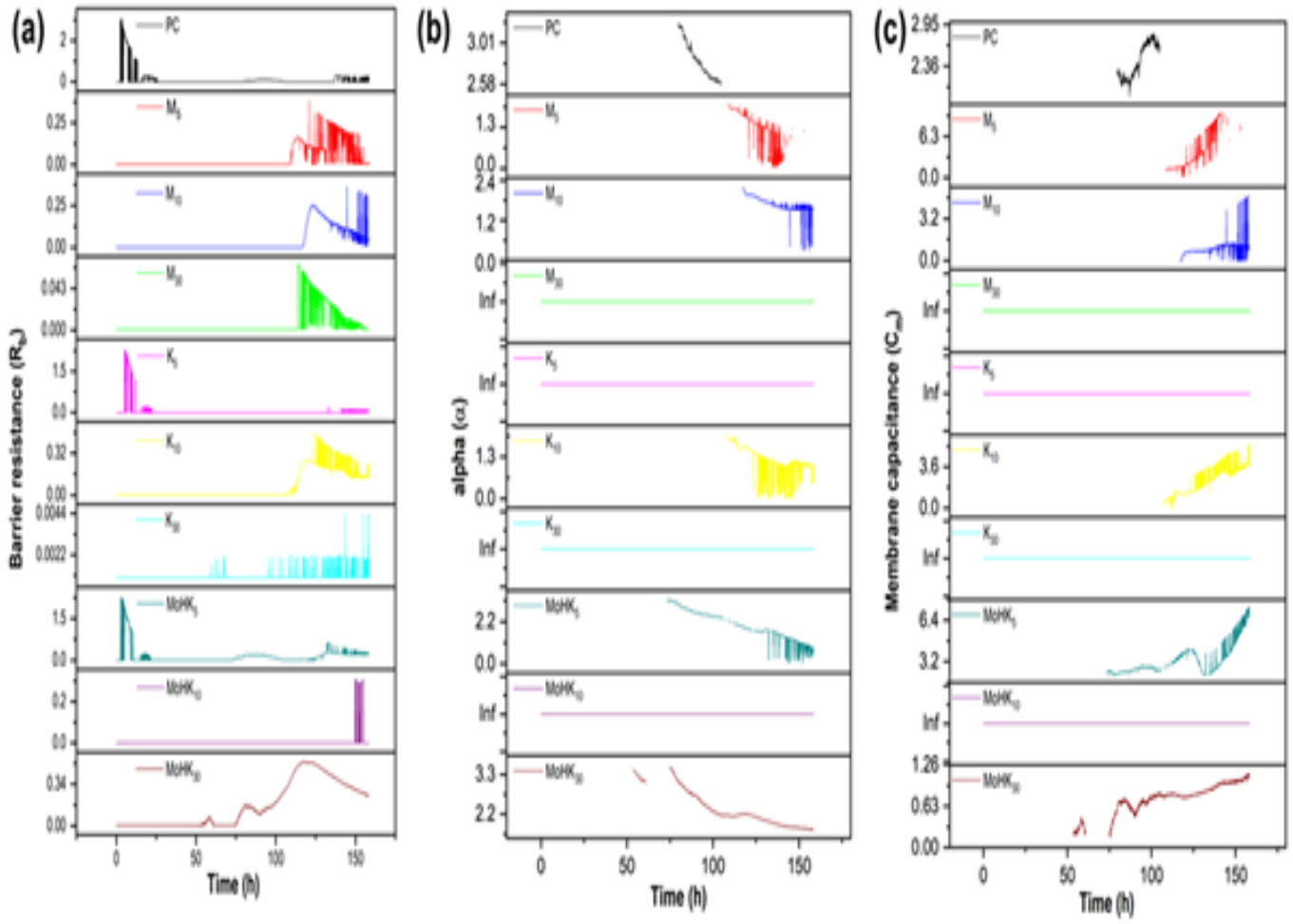

Figure S6. (a) Barrier resistance, (b) alpha, and (c) membrane capacitance as derived from ECIS real-time monitoring of cytocompatibility studies after modeling against control at t = 42 h.

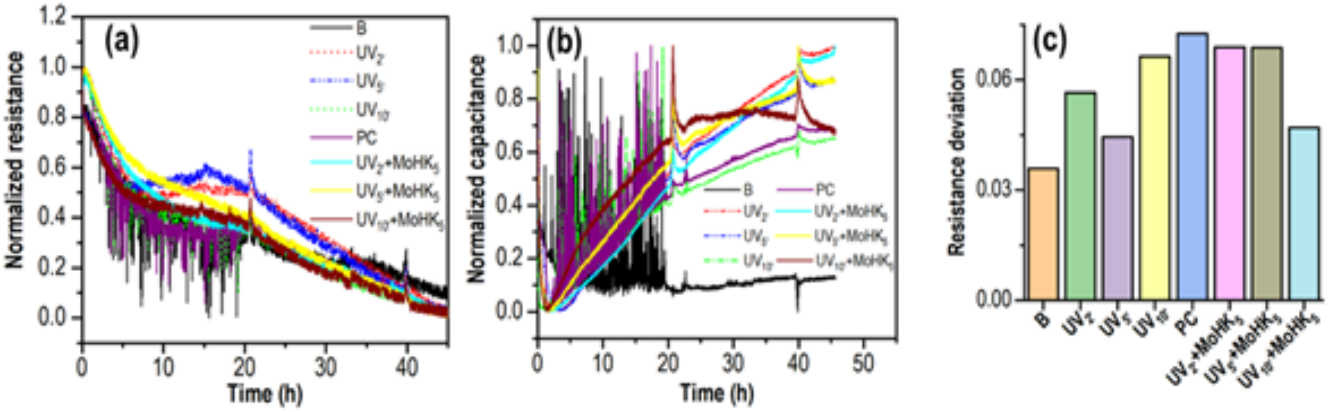

Figure S. Normalized resistance (a) and capacitance (b) monitored at low frequency of 62.5 Hz showing more in-depth biophysical changes of RAW 264.7 cells on gold microelectrodes, and Comparative histogram depicting the standard deviation (c) in the resistance response throughout the experiment from the mean value of resistance.

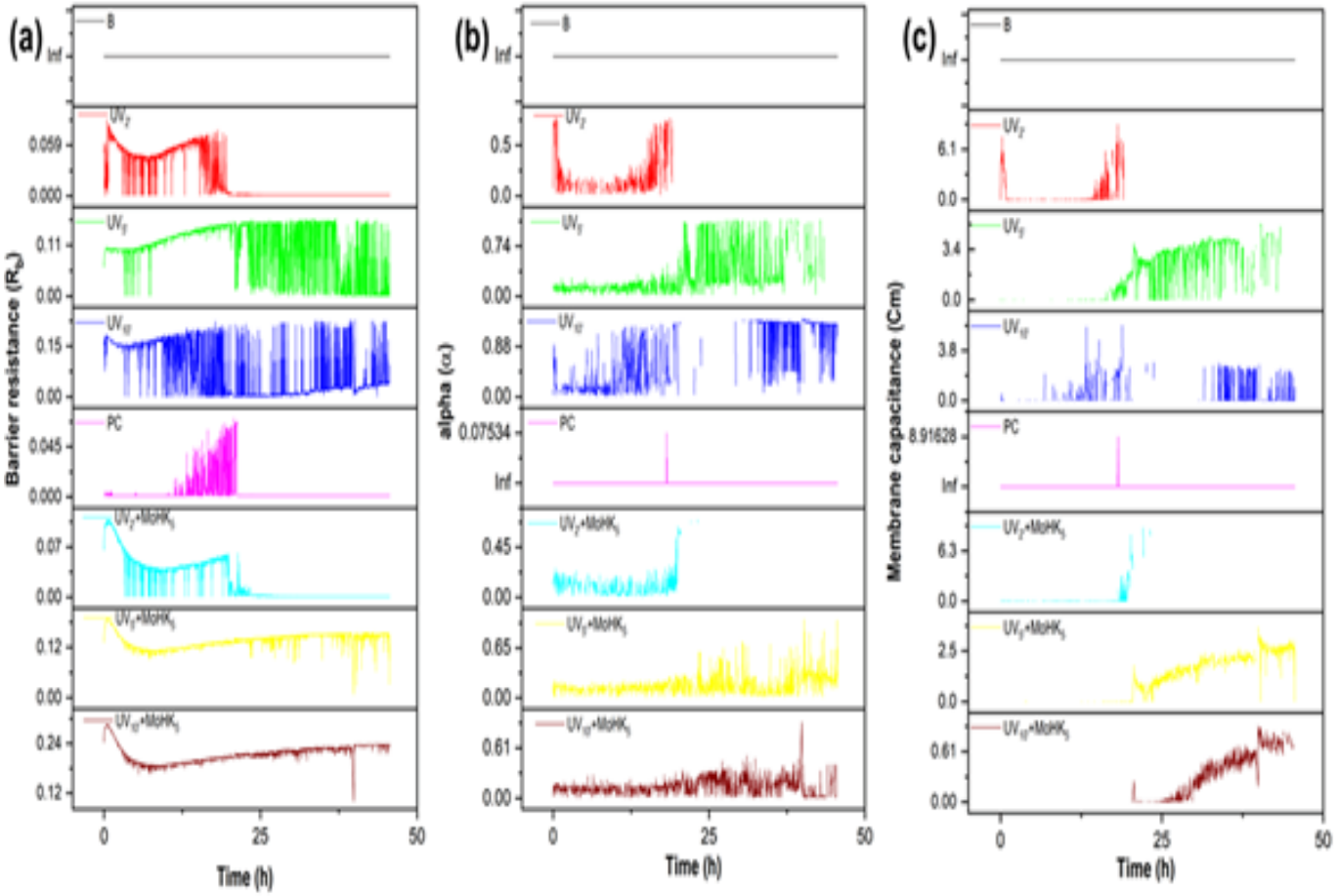

Figure S7. ECIS-derived data depicting the cell-cell junction variation with respect to UVC exposure and its healing in presence of MoHK, (a) barrier resistance, (b) alpha, and membrane capacitance (c).

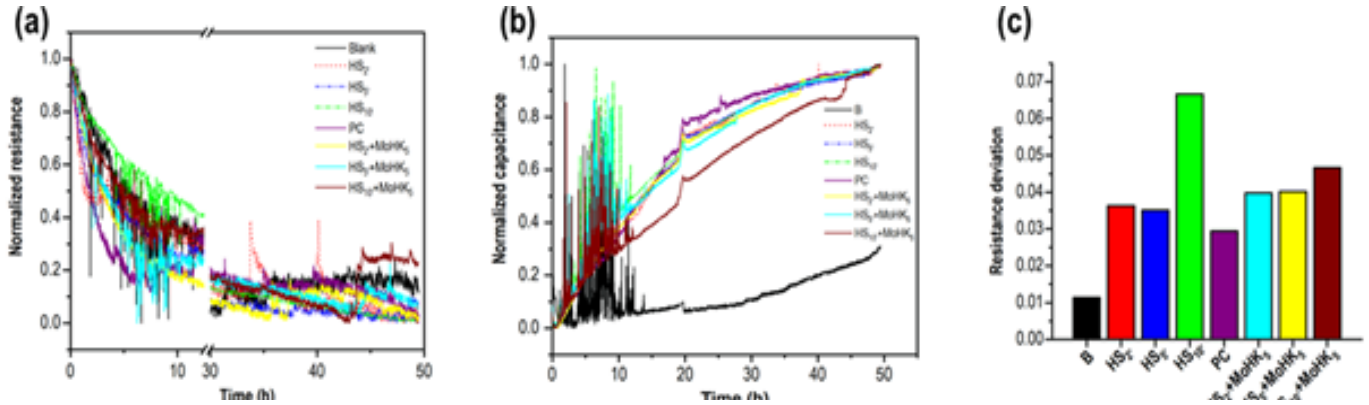

Figure S8. Normalized resistance (a) and capacitance (b) behavior of cells at 62.5 Hz, and (c) standard deviation values for all the wells measured from ECIS data.

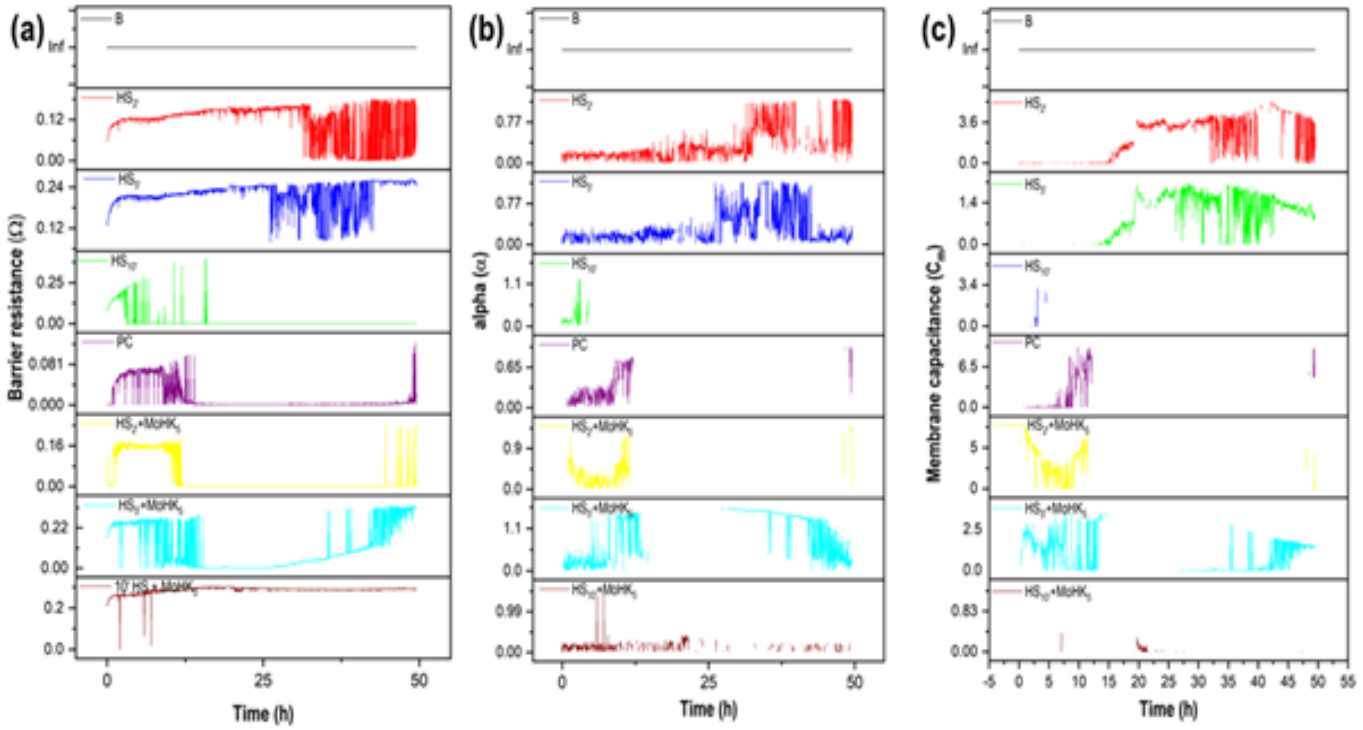

Figure S9. Effect of heat shock and MoHK NPs on the cell biophysical parameters as derived from modeled ECIS data: (a) barrier resistance, (b) alpha, and (c) membrane capacitance.

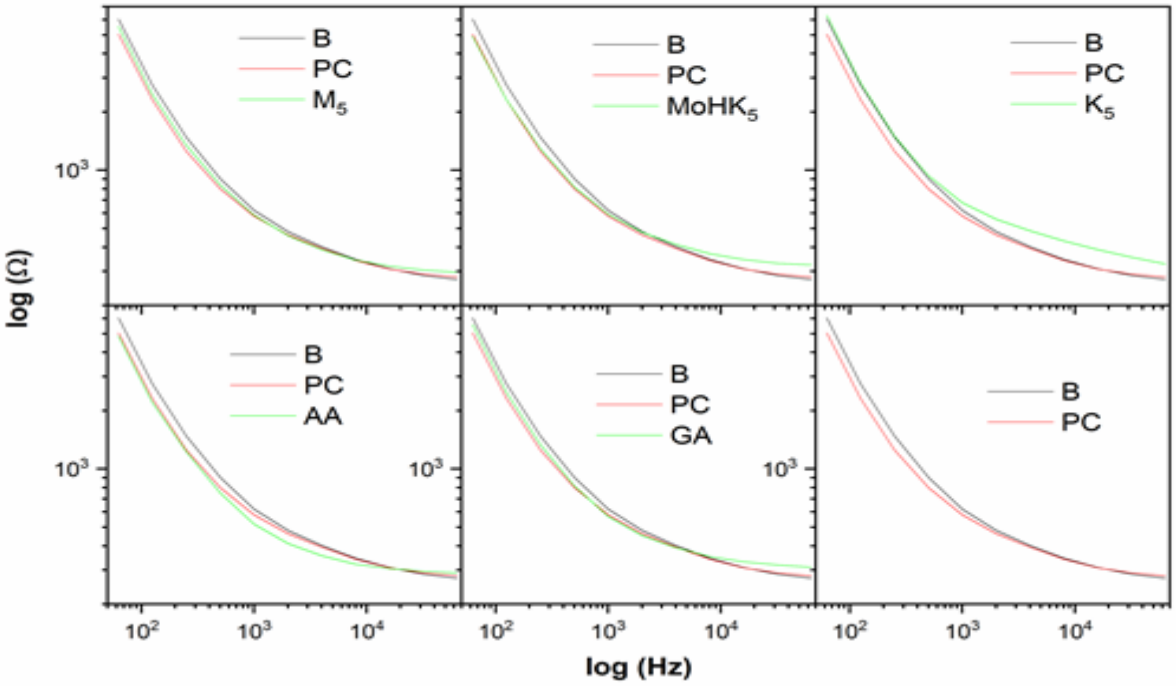

Figure S10. Comparative frequency vs resistance analysis for the wells. including A02- M5, A03- MoHK5, A04-K5, A06- AA, A07-GA, Blank, and PC-positive control.

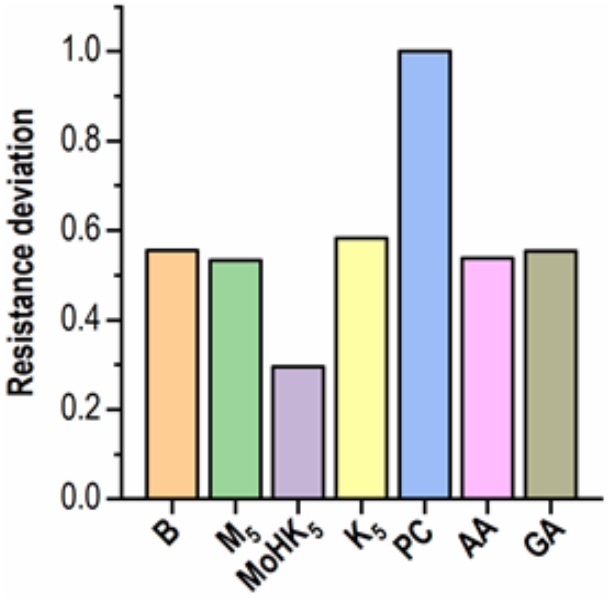

Figure S11. Normalized standard deviation value for resistance with respect to the mean resistance throughout the experiment as derived from Fig 4.

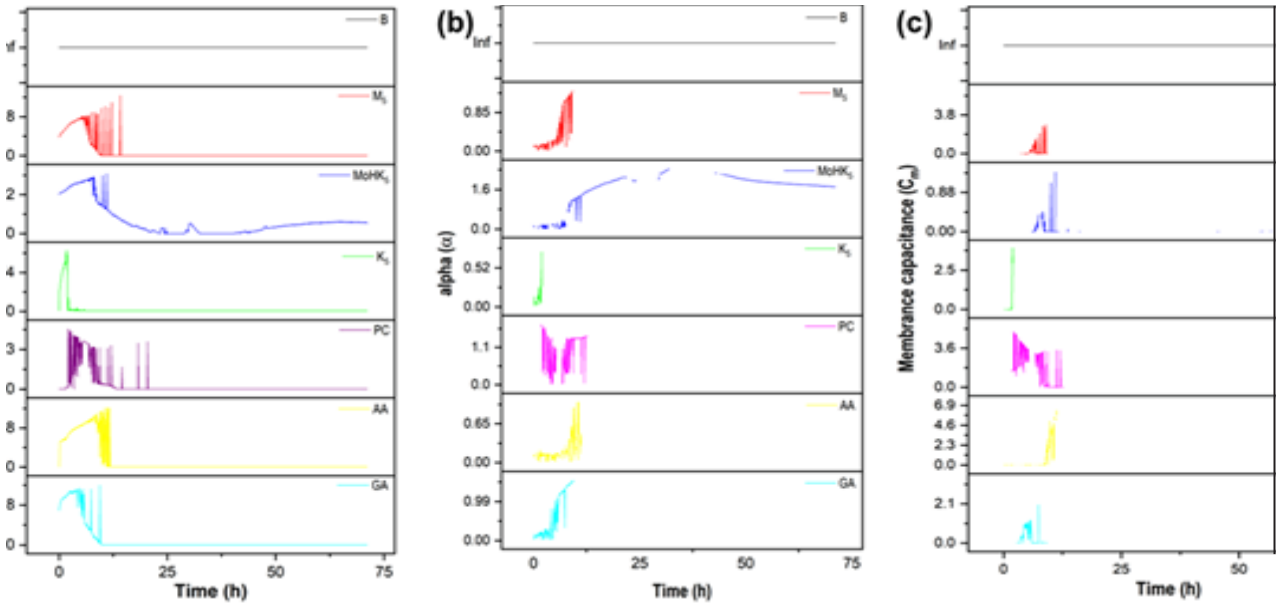

Figure S12. ECIS-derived cell modeled cell biophysical data: (a) barrier resistance, (b) alpha, (c) membrane capacitance data.

Reference

[S1] C. Lo, C.R. Keese, I. Giaever, Impedance Analysis of MDCK Cells Measured by Electric Cell-Substrate Impedance Sensing, Biophys. J. 69 (1995) 2800–2807. https://doi.org/10.1016/S0006-3495(95)80153-0.

Reinforced perflurosulfonic acid membrane with improved water holding capacity in low humidity polymer electrolyte fuel cells: Its future significance in unitized regenerative fuel cells

*Sreekuttan M. Unni[a,b], Vishal M. Dhavale[a,b], Harshal Agarwal[a,b], Santoshkumar D. Bhat[a,b],**
[a]CSIR-Central Electrochemical Research Institute-Madras Unit, CSIR Madras Complex, 600 113, India.
[b]Academy of Scientific and Innovative Research (AcSIR), Ghaziabad- 201002, India
**Corresponding author: sdbhat@cecri.res.in*

Abstract:

The performance of polymer electrolyte fuel cells (PEFCs) is significantly influenced by the membrane's ability to maintain optimal hydration levels. This study focuses on enhancing fuel cell performance through the optimization of humidity levels using a reinforced perfluorosulfonic acid (PFSA) membrane with improved water-holding capacity. The research investigates the impact of varying humidity conditions on the efficiency and durability of PEFCs, particularly under demanding operational environments. Reinforced PFSA membrane (Nafion-HP) to enhance water retention, was considered and tested under different humidity regimes to assess its effectiveness in maintaining stable hydration. The results demonstrate a marked improvement in fuel cell performance, with enhanced proton conductivity and reduced degradation rates observed in the optimized membrane. The findings have significant implications for the future development of unitized regenerative fuel cells (URFCs), where maintaining precise humidity control is crucial for efficient energy conversion and storage. This study contributes to the advancement of high-performance fuel cell technology by providing insights into the role of membrane hydration in optimizing fuel cell efficiency and longevity

Keywords: *PEFCs; PFSA; URFCs; MEA; EL; ORR*

Introduction

Unitized regenerative fuel cells (URFCs) represent a promising technology for energy storage and conversion, offering the potential for seamless transition between electrolysis and fuel cell operation. Integrating self-humidified membranes into URFCs enhances their performance, durability, and practicality, making them a compelling solution for various applications. An URFC consists of a membrane electrode assembly (MEA) that includes an ion-conducting membrane, typically a H^+-conducting perfluorosulfonic-acid membrane, which separates the electrodes responsible for electrocatalysis (catalyst layer) and gas or liquid transport (gas diffusion or porous transport layers) [1]. During charging (EL mode), the oxygen-evolution reaction (OER) occurs at the anode, and the hydrogen-evolution reaction (HER) occurs at the cathode. During discharging (FC mode), the hydrogen-oxidation reaction (HOR) occurs at the anode, and the oxygen-reduction reaction (ORR) occurs at the cathode. An URFC requires each electrode to be bifunctional to support both modes of operation. This bifunctionality can be achieved through two configurations: constant-gas (CG) or constant-electrode (CE). In the CG configuration, the URFC consists of an oxygen electrode (ORR/OER) and a hydrogen electrode (HOR/HER) [2]. In the CE configuration, the URFC consists of an anode (HOR/OER) and a cathode (ORR/HER), with gases at the anode and cathode being switched between EL and FC modes [3].

The relevance of URFCs with self-humidified membranes lie in their ability to address key challenges associated with membrane dehydration in URFC operation and conventional fuel cell systems along with energy storage technologies while unlocking new opportunities for renewable energy integration and sustainable development [4]. Self-humidified membranes play a critical role in maintaining optimal hydration levels within the fuel cell, thereby improving proton conductivity and electrochemical kinetics. By effectively managing water distribution and retention, these membranes minimize mass transport losses and ensure efficient proton transport across the electrolyte. This results in enhanced fuel cell performance, higher power density, and improved overall energy conversion efficiency in URFCs, making them more competitive with other energy storage technologies [5].

The integration of self-humidified membranes enhances the durability and reliability of URFCs by mitigating issues related to membrane dehydration, water flooding, and chemical degradation. The self-humidified membranes offer superior water management, maintaining stable hydration levels under varying operating conditions and reducing the risk of performance degradation over time [6]. As a result, URFCs with self-humidified membranes exhibit prolonged service life, increased operational reliability, and reduced maintenance requirements compared to traditional fuel cell systems. Self-humidified membranes streamline the design and integration of URFCs by eliminating the need for external humidification systems and complex water management components. This simplification not only reduces system complexity and manufacturing costs but also enhances system compactness and portability, making URFCs more suitable for diverse applications, including automotive, stationary power generation, and off-grid energy storage [7].

Additionally, the integration of self-humidified membranes facilitates the development of plug-and-play URFC systems that are easier to install, operate, and maintain in real-world applications. URFCs with self-humidified membranes offer a versatile platform for integrating renewable energy sources, such as solar and wind power, into the energy infrastructure. By converting excess renewable energy into hydrogen through electrolysis during periods of low demand, URFCs enable efficient energy storage and grid balancing, thereby enhancing the stability and reliability of renewable energy systems. Moreover, the reversible operation of URFCs allows for the generation of clean electricity from stored hydrogen during peak demand periods, supporting grid stability and reducing reliance on fossil fuels [8].

The adoption of URFCs with self-humidified membranes contributes to the advancement of sustainable development goals by promoting clean energy production, reducing greenhouse gas emissions, and fostering energy independence and security. By harnessing renewable energy sources and enabling efficient energy conversion and storage, URFCs play a crucial role in transitioning towards a low-carbon economy and mitigating the impacts of climate change. Furthermore, the scalability and versatility of URFC technology make it adaptable to various socioeconomic contexts and geographic regions, empowering communities to achieve energy access, resilience, and economic prosperity.

Nafion HP membranes represent a significant advancement in proton exchange membrane (PEM) technology for polymer electrolyte membrane fuel cells (PEMFCs). These membranes offer high proton conductivity, excellent mechanical strength, low methanol permeability and increased water management capabilities [9,10], making them particularly suitable for enhancing the performance and durability of PEFCs. However, optimizing the humidity levels and water balance in operating PEMFCs is a critical challenge to enable high performance URFCs. In this study, we explore the optimization of humidity levels in operating PEMFCs using reinforced Nafion HP membranes, focusing on their benefits and applications and its further relevance to unitized regenerative fuel cells.

Hence, in the present study, the entire focus was on optimizing the humidity levels in operating PEMFCs with the self-humidified Nafion HP-based reinforced membrane electrode assemblies (MEAs) and analyzing the chemical stability of the membranes at lower humidity and high temperature (30 %RH and 80 ^{o}C for longer duration @ OCV hold). The presence of silica in the reinforced membrane is an added advantage since it holds water even at low relative humidity as we envisage retention in cell performance even at low RH.

2.Experimental

2.1. Membrane electrode assembly fabrication

The MEA is fabricated using a Nafion HP membrane (reinforced perflurosulfonic acid membrane with silica nanoparticles, 0.8 mil thick, designed for lower relative humidity environments and high operating temperature, procured from Ion Power®), carbon-supported platinum catalyst (50 wt.% Pt/Vulcan XC72, BASF®) and Toray (Toray-060, 5% PTFE wet proofing) carbon gas diffusion layers (GDLs). In brief, a 5 cm × 5 cm area of Toray® carbon (TGP-H-060, 5 wt. % wet proofing) is cut and weighed. For slurry preparation, Pt/C (100 mg) is dispersed in 6 mL of water and to that mixture, 3.06 mL of iso-propyl alcohol (IPA) is added. 0.807 mL Nafion ionomer is added to the above dispersion to achieve a Nafion/Carbon mass ratio of 0.75. This is sonicated for 90 min to have a uniform dispersion. The above slurry is spray coated onto the Nafion membrane to achieve a loading of 0.3 mg Pt/cm^2. The membrane is dried to remove excess solvent. Two 5 cm^2 electrodes are cut from the larger 25 cm^2 electrode, one to be used as the anode and the other to be used as the cathode. The

schematic of the fabrication of catalyst coated membrane (CCM) and MEA is represented in **Figure 1.**

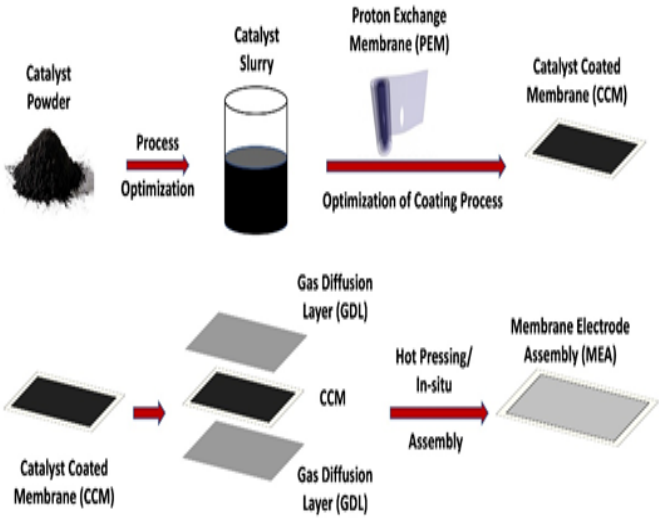

Fig. 1. Schematic illustration of catalyst coated membrane via spray coating and membrane electrode assembly fabrication

The electrodes are pressed with the catalyst coated membrane (integrated between 6 mil PTFE gaskets on either side) using a hot press (Karver). The hot press temperature was 130 °C and 3.79 MPa of pressure was applied at this temperature for 3 min to form the MEA. Next, the MEA is integrated into a Scribner fuel cell fixture comprised of graphite plates with a single channel serpentine flow field along with other components (current collector and endplate with nuts and bolts). The cell was bolted together with 30 in.lb torque.

2.2. Conditioning of the fuel cell and cell polarization

To begin cell testing, the cell is connected to the fuel cell test station (Scribner 850e). It is ensured that the fuel cell test station has enough water, as well as proper amounts of N_2, H_2 and O_2 gas in the connected gas cylinders. These gases will be supplied to the humidifiers and cells throughout the testing.

2.2.1. Cathode starvation break-in for the cell before the testing

To initiate cell break-in, humidifier temperature (dew points) of 80 °C and Cell temperature of 80 °C was maintained. H_2 and O_2/air are supplied to the anode and cathode sides of the cell, respectively. A hydrogen backpressure of 0.5 bar is applied; the backpressure on the anode is increased from ambient to 1.5 bar total pressure to aid the crossover of H_2 from the anode to cathode during break-in. The current is increased in steps until the cell voltage is decreased 0.3 V. The voltage is held at 0.3 V for 2-5 min for the current response to stabilize. The current density is then reduced to 200 mA/cm^2. Oxygen/air supply is stopped while maintaining the current at 200 mA/cm^2. The voltage of the cell is observed to drop since there is no supply of oxygen to the cathode. When the voltage drops to 0.2 V, oxygen/air is re-supplied to the cathode quickly. The process is repeated until the voltage difference between the two cycles is < 5 mV. At the end of the conditioning procedure, the back pressure was reverted to ambient [10].

2.2.2. Conditioning of the cell after the break in and cell testing

The cell was purged with Nitrogen initially at the rate of 0.4 lpm through both the anode and cathode of the cell. Both humidifier temperatures are raised from 30 to 80 °C, followed by the cell temperature (80 °C). When the cell temperature reaches 80 °C, the cell is stabilized for 1 h and then the H_2 and O_2/air fuel is supplied at the required stoichiometry (0.2 lpm for H_2 and 0.1 lpm for O_2 and 0.47 lpm for air). After stabilization of the OCV, the current is applied (200 mA/cm^2) and the cell can stabilize for 2 h. After this, the polarization curve is recorded at regular time intervals, stepping the current in set amounts until a lower cutoff voltage of 0.1 V is achieved. After recording the polarization, the cell is cooled down by turning off the heaters and passing humidified nitrogen.

2.2.3. Cell polarization at different relative humidities and stability test

The cells are polarized at different relative humidities to see the effect of the relative humidity (30 to 100 %RH on both anode and cathode) on fuel cell performance. Further, chemical stability for the membrane is analyzed by monitoring the OCV in relation to time at 30 % RH @ 80 °C.

3. Results and Discussion

The unique structure of the Nafion HP membrane facilitates efficient proton transport while effectively managing water content within the membrane, critical for maintaining high fuel cell performance. This reinforced

membrane offers several advantages for humidity control in PEFCs with respect to improved water retention properties to help maintain adequate hydration levels even under low humidity conditions. This feature is particularly beneficial for mitigating dehydration effects and ensuring continuous proton conduction within the membrane. In addition, with reduced water flooding, reinforced membranes exhibit superior water management capabilities, effectively preventing water flooding under high humidity conditions. By regulating water uptake and distribution, these membranes minimize the risk of flooding-induced performance degradation and enhance overall cell efficiency and enhanced durability. The mechanical robustness and chemical stability of Nafion HP membranes contribute to their long-term durability in fuel cell operation. These membranes are less prone to swelling, degradation, and pinhole formation, even in harsh operating environments with fluctuating humidity levels. The presence of silica in the Nafion HP membrane provides water holding capacity for the membrane to work at various relative humidity. The uniform distribution of silica is seen in membrane morphology from Scanning electron microscopy as represented in **Figure 2**.

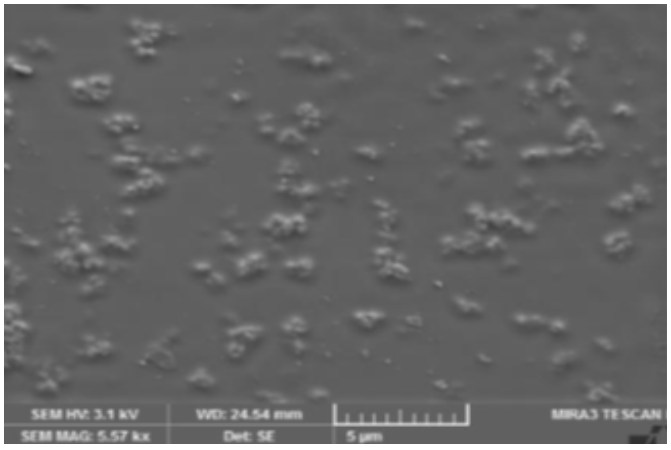

Fig. 2. SEM morphology for Nafion-HP membrane confirming the presence of silica in the membrane matrix.

In the present work, humidity levels have been optimized while using Nafion HP membranes, implementing various strategies tailored to specific operating conditions, like humidification control. Advanced humidification systems are integrated into PEFC test stations to precisely regulate the humidity of reactant gases and maintain optimal water content within the membrane. This ensures consistent proton conductivity and maximizes cell performance over a wide range of operating conditions. The humidity levels at various temperatures for the tested cells are provided in **Table 1** [11].

Table 1. Tabulation of relative humidities for the membranes with constant cell temperature in H_2-air configuration to attain the required %RH.

% RH	Cell temperature (°C)	Humidifier temperature (°C)	Cell temperature (°C)	Humidifier temperature (°C)
30	80 °C	53.0	70 °C	44.5
40		59.0		50.0
50		64.0		55.0
60		68.0		59.0
70		71.5		62.0
80		74.5		65.0
90		77.5		67.5
100		80.0		70.0

It is observed in the polarization curves, **Figure 3** that the Nafion HP membrane retains good cell performance at variable levels of humidities under H_2-Air configuration (0.2 lpm of H_2 and 0.47 lpm of Air).

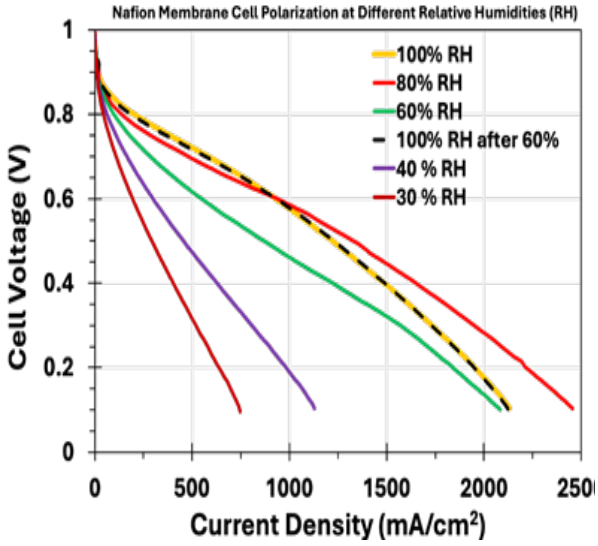

Fig. 3. Cell Voltage vs. Current density (mA/cm^2)

for the Nafion membrane at various relative humidities.

The Nafion™ HP is an ultra-thin membrane that offers high power density. The membrane is reinforced and designed for lower relative humidity environments and high operating temperature. It can be clearly seen that silica in the Nafion membrane has a very good water holding capacity and hence some reasonable cell performance retained even at 30 %RH. Maximum fuel cell performance is seen at 80 % RH along with an improvement in the mass transfer region. Cell performance is also very good at 100 %RH, but there is a drop in the mass transfer region, likely due to excess water. This clearly indicates that reinforced membrane is useful to improve the mass transfer region at slightly lower RH in comparison to 100 % saturation. In addition, the peak power density for cell using the Nafion HP

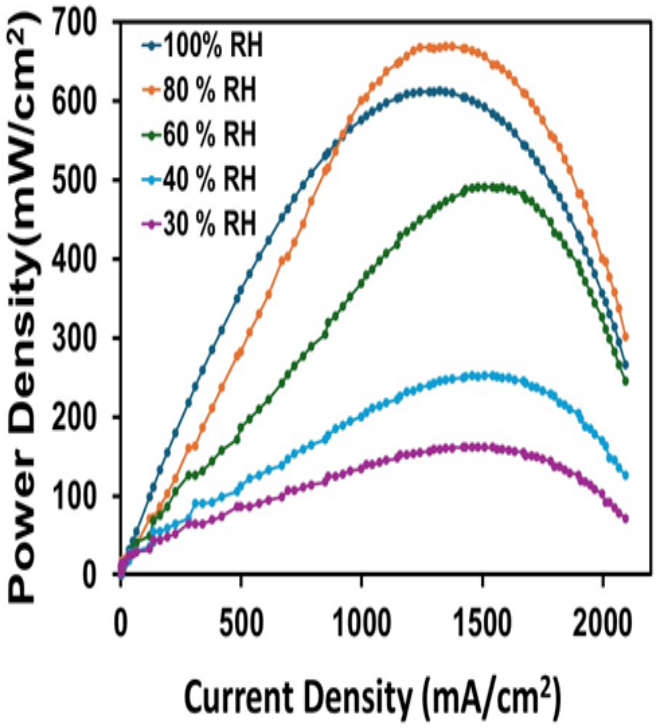

Fig. 4. Peak power densities in relation to current density for Nafion membrane at different relative humidities.

Stability data for operating cells with the reinforced Nafion HP membrane is also shown under H_2-air configuration. Cells are tested following start-stop cycle for the two days, 6 h each day, which clearly indicates that there is no drop in open circuit voltage and data while holding the open circuit voltage (OCV) at 30 %RH @ 80 °C in relation to time is stable, confirming the chemical

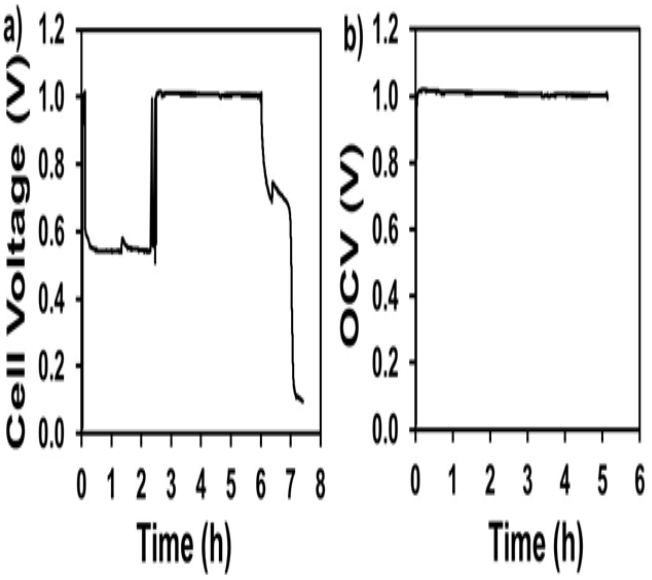

Fig. 5. (a) Change in cell voltage during cell polarization, and (b) OCV hold in relation to time for Nafion membrane at 30 %RH and cell temperature of 80 °C.

Figure 5a shows the change in OCV in relation to time during cell polarization experiments. OCV was initially recorded before the cell polarization experiments (before applying current) and then the current was applied to 1 A to analyze the change in OCV and then stabilize and the steps are repeated before the cell polarization and after the cell polarization. Stability was also analyzed at the OCV hold without any current load @ 30 %RH to see steady state as represented in **Figure 5b**. The data confirms that membrane electrolytes are stable even at lower RH during PEMFC operation.

3. Conclusions

To summarize, the optimization of humidity levels through Nafion HP membranes has significant implications for various PEFC applications, including automotive, stationary power generation, and portable electronics. It is proven that Nafion membrane in presence of silica can retain cell performance even at low RH. Cell break-in protocol and stability test are critical for these membranes which also confirms the chemical stability

of the membrane electrolytes. The current density of 1 A/cm^2 at 0.6 V at 80 % RH confirms the improved cell performance for Nafion HP membranes. By enhancing water management capabilities and ensuring reliable operation under diverse operating conditions, reinforced high performance Nafion membranes contribute to the widespread adoption of PEFC technology across different sectors. Future research directions will focus on further refining the design and properties of Nafion HP membranes to achieve improvements in URFC performance, durability, and cost-effectiveness along with preparation of bifunctional catalysts for improved round trip efficiency. Additionally, exploring novel materials and fabrication techniques could lead to the development of next-generation PEMs with enhanced humidity control and overall cell performance.

Acknowledgements

The authors acknowledge CSIR-Fast track tranlational Program (FTT060503) and CSIR-Hydrogen technogy Mission Progam (H_2T) for the financial assistance

Declaration of competing interest

There no competing financial interests to declare for the research reported in this article

References

[1] A. Kusoglu and A. Z. Weber, **Chem. Rev.,** 2017, 117, 987–1104.

[2] R. Baldwin, M. Pham, A. Leonida, J. McElroy and T. Nalette, **J. Power Sources,** 1990, 29, 399–412.

[3] J. Ahn and R. Holze, **J. Appl. Electrochem.,** 1992, 22, 1167-1174

[4] Immanuel Vincent, Eun-Chong Lee and Hyung-Man Kim, RSC Adv., 2020, 10, 16844

[5] Yagya N. Regmi, Xiong Peng, Julie C. Fornaciari, Max Wei, Deborah J. Myers, Adam Z. Weber, Nemanja Danilovic, **Energy Environ. Sci.,**13 (2020) 2096-2105

[6] K. Devi Renuka, Santoshkumar D. Bhat, Sreekuttan M. Unni, 2022, Chapter 11, **Renewable Energy Technologies: Advances and Emerging Trends for Sustainability,** WILEY Publishers

[7] Kangwei Qiao, Huibing Liu, Shiqing Huang, Xiaofei Zeng**, Dapeng Cao*, **International Journal of Hydrogen Energy,** 50, 2024, 209-220

[8] Noor ul Hassan, Prabhu Ganesan, Aaron A. Lando, William E. Mustain, Hector R. Colon-Mercado, **Journal of Power Sources** 541 (2022) 231599

[9] Mingzhang Pan, Chengjie Pan, Chao Li, Jian Zhao, Renewable and Sustainable Energy Reviews, 141, 2021, 110771Pablo A. García-Salaberri, **Sustainable Materials and Technologies** 38, 2023, e00727

[10] Hang Su, Donghao Ye, Yuanqi Cai, Wei Guo, **Applied Energy** 323 (2022) 119626

[11] M Neeshma, Santoshkumar D Bhat*, **ACS Applied Materials and Interfaces** 15 (2023) 53881-53890

PROFORMA OF SUBSCRIPTION FORM

I /We wish to subscribe **The Journal of Electrochemical Society of India (JECSI)** for ..... year(s) for which (i) a Demand Draft vide …….....……. dated …….....…… issued from (Name of the bank…….....)favouring **ELECTROCHEMICAL SOCIETY OF INDIA JOURNAL, payable at Bengaluru or (ii) NEFT/IMPS vide UTR no……..dated for Rs/US $…….is enclosed.**

NAME…….

DESIGNATION…….

POSTAL ADDRESS…….

……PIN…….....

E-MAIL…….Phone no.……

Subscriber ID (for renewal only)……

Signature…….

Bank account details	**Subscription details:**
Name: Electrochemical Society of India Journal Account No. 110045333254 Bank Name: Canara Bank Customer ID: 309740255 IFSC Code: CNRB0000683 MICR Code: 560015023 Indian Institute of Science Canara Bank IISc, Bangalore - 560012	**Print only**: For institutions & Individuals: Annual 6 issues: Rs 2000/- (India), Annual 6 issues: USD 250.00 incl. postages (abroad), For students: Annual 6 issues: Rs 1000/- **Print & Online (customer type: institution):** USD 100.00 & INR 5000.00 Please note that institutional prices are available only for libraries of higher education institutions and research organizations.

Journal of the Electrochemical Society of India

Vol. No. 73 (5 & 6), Jul-Sep 2024

CODEN - JESIA 73 [5&6] 2023 ISSN:0013-466X

Email : ecsiiisc@gmail.com

FROM IV

See Rule VIII

1.	Place of publication	:	Bengaluru
2.	Periodicity of its publication	:	Quarterly
3.	Printer name	:	Print Hut
	Whether the Citizen of india	:	YES
	Address of the printer		Govindarajnagar Bengaluru - 560040
4.	Publishers Name	:	**The Electrochemical Society of India**
5.	Editor's Name	:	Dr. U. Kamachi Mudali
	Whether Citizen of India	:	Yes
	Address	:	**The Electrochemical Society of India** Indian Institute of Science Campus, Bangalore - 560 012
6.	Name and Address of Individuals who own the newspaper/holders and partners and shareholders	:	**The Electrochemical Society of India** Indian Institute of Science Campus, Bangalore - 560 012. holding more than 1% of the total capital.

I, Dr. U. Kamachi Mudali hereby declare that the particulars given above are true to the best of my knowledge and belief.

Sd/-

Dr. U. Kamachi Mudali

Chief Editor, JECSI

(Publisher)

THE ELECTROCHEMICAL SOCIETY OF INDIA

Indian Institute of Science Campus, Bengaluru - 560 012, India
Phone : +91-80-22932613
E-mail : ecsiiisc@gmail.com | www.ecsi.in

CALL FOR NOMINATIONS FOR ECSI AWARDS- 2024

Shri S.K. Seshadri Memorial Mascot National Award
(Instituted in the year 1980)

With a view to stimulate interest among Scientists and Technologists in the field of corrosion, the Electrochemical Society of India has instituted the prestigious "**Shri S. K. Seshadri Memorial Mascot National Award"** for notable and outstanding contributions in the field of Industrial Corrosion. The award is sponsored by Director, M/s. Biosafe Solutions.

1. The research work considered for this award should be in the field of Corrosion Science and Technology, Corrosion Prevention and Allied aspects. Industrial Significance to be highlighted and Industrial applicability is desired.

2. The work should have been carried out to bring it to the point of application. The process of development and test schedules may have been carried out during the preceding couple of years, but should have culminated in a fruitful result. The work need not necessarily have been published.

THE N. M. SAMPAT AWARD - 2024
(Instituted in the year 1986)

With a view to recognize outstanding services rendered to the Electroplating industry andTechnology, the Governing Council of the ECSI has with great pleasure has instituted "**The N. M. Sampat Award".** This award is sponsored by M/S Canning Mitra Phoenix Limited, Mumbai. Research work considered for this award should be in the field of Metal Finishing, Electroplating, Surface Coating and Modification, and allied fields. Work carried out in these areas with possible industrial applicability or academic excellence would be considered. The work need not have been published but industrial applications should have been established.

ECSI- METROHM National Award - 2023
(Instituted in the year 2021)

With a view to recognize the contributions made by individuals in the field of basic electrochemistry, electrochemical instrumentation and devices, theoretical and; experimental electrochemistry, the Electrochemical Society of India has instituted this prestigious award **"ECSI- METROHM National Award for Electrochemical Science".** The award is sponsored by M/s Metrohm India Ltd. Chennai. Meritorious work in any field of Electrochemical Science would qualify for this award.

ECSI- AMARA RAJA National Award- 2023
(Instituted in the year 2021)

With a view to stimulate interest among Scientists and Technologists in the field of Batteries, Fuel Cells and Sensors, the Electrochemical Society of India has instituted the prestigious award **"ECSI- AMARA RAJA National Award for Advanced Electrochemical Technology".** The award is sponsored by M/s. Amara Raja Batteries Ltd. Tirupathi. Meritorious work in the field of Batteries, Fuel Cells and Sensors would qualify for this award.

ECSI-Dr. K. Elayaperumal National Award- 2023
(Instituted in the year 2022)

With a view to recognize the outstanding contributions of individuals made in the area of Corrosion Mitigation in Industries, The Electrochemical Society of India has instituted the prestigious award "ECSI- Dr. K. Elayaperumal National Award for Excellence in Industrial **Electrochemical Science and Technology"** from this year. The award is sponsored by Dr. K. Elayaperumal and his family. Meritorious work in the area of corrosion mitigation in industries would qualify for this award.

GUIDELINES FOR NOMINATION

1. Nominations may be made by Research Organizations/Institution/ Industries/Individuals.
2. The nomination should be accompanied by the complete bio-data and important contributions for which the nomination is being made.
3. The work should have been carried out to bring it to the point of application. The process of development and test schedules may have been carried out during the preceding couple of years, but should have culminated into a fruitful result at least during the year of application.

Each of the above awards carries a Scroll of Honor and cash prize.

Awardees are required to present their work in the form of an **Award Lecture** and also submit a written manuscript for publication in the Journal of Electrochemical Society of India. Complete Nominations in all respects for the above awards should reach The Secretary, The Electrochemical Society of India, Indian Institute of Science Campus, Bengaluru - 560 012.

Nominations complete in all respects for the above awards should reach
Hon President or General Secretary,
The Electrochemical Society of India, Indian Institute of Science Campus,
Bengaluru - 560 012,
E-Mail: ecsiiisc@gmail.com

Dr. S. T. Aruna	**Dr. Ajay Krishnan**
Hon. President, ECSI	Hon. Gen. Secretary, ECSI

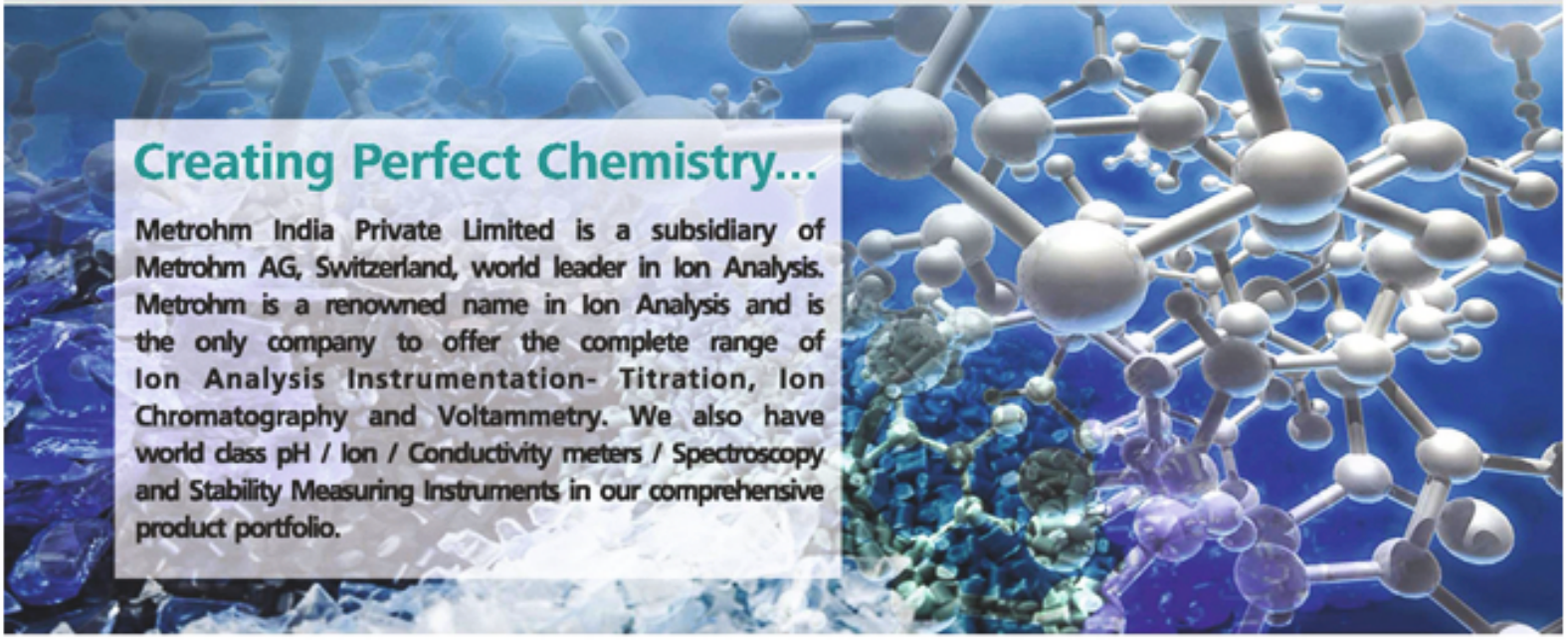

Creating Perfect Chemistry...

Metrohm India Private Limited is a subsidiary of Metrohm AG, Switzerland, world leader in Ion Analysis. Metrohm is a renowned name in Ion Analysis and is the only company to offer the complete range of Ion Analysis Instrumentation- Titration, Ion Chromatography and Voltammetry. We also have world class pH / Ion / Conductivity meters / Spectroscopy and Stability Measuring Instruments in our comprehensive product portfolio.

Titrator

Ion Chromatography

Voltammetry

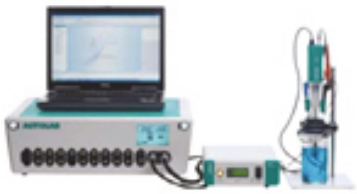

Electrochemical station

NIRS Analyzer

Raman Spectroscopy

Labwater Purification

Surface Area Analyzer

We also have:

- Electrochemical research instrumentation from Metrohm Autolab
- On-line and at-line process analyzers for process monitoring from Metrohm Process Analytics
- NIR and Raman Spectroscopy solutions from Metrohm and B&W Tek
- Innovative technology for electrochemistry research from Dropsens
- BET surface area, pore size distribution from MicrotracBEL Corp., Japan
- Testing instrumentation for the energy storage device and energy conversion device markets from Arbin instruments
- Lab water solutions from Elga
- Pipetting and dispensing solutions from Socorex

PARTICIPATE IN WATER SURVEY

SCAN ME

GET YOUR **FREE** GIFT!

Metrohm India Private Limited
Metrohm-SIRI Towers, 3&4, Fourrts Avenue, Annai Indira Nagar
Okkiyam, Thoraipakkam, Chennai - 600097, India.
Ph: +91 44 40440440 | Customer support: +91 44 40440444

For details, e-mail us at **info@metrohm.in** or visit us at **www.metrohm.in**

Metrohm
India Private Ltd.